OPTICAL THIN FILM MEASUREMENT BY INTERFEROMETRIC FRINGE PROJECTION AND FLUORESCENCE STIMULATED EMISSION

Daniele Dipresa

Submitted in accordance with the requirements for the degree of
Doctor of Philosophy

The University of Leeds
School of Mechanical Engineering

February 2013

The candidate confirms that the work submitted is his own and that appropriate credit has been given where reference has been made to the work of others.

Acknowledgements

I would like to express profound gratitude and sincere thanks to my Professor Dave Towers and Dr Cathy Towers for their invaluable support, encouragement and guidance during the course of this research work.

Besides my supervisors, I would like to thank all the technicians at the Mechanical Engineering department. In particular, special thanks go to Paul Banks for his help with the experimental rig used in this project.

I wish to extend my thanks to my colleagues and above all friends within our research group.

My gratitude extended to all my friends in Leeds and around the world. They always helped me with their enthusiasm.

I am especially indebted to my family, my parents Elena and Sergio and my little sisters Valentina and Savina for being my inspiration and motivation through what has been an arduous period of studies.

My sincere thanks to my girlfriend, Lucrezia for sharing with me those long nights whilst I was writing up, for her love and motivation.

Finally I would like to thank everyone who believed in me.

Abstract

The introduction of a new technique for metrology of thin liquid films to give both the profile of the exterior surface and information on the thickness of the film is the main focus of this research. The proposed approach is based on the use of fringe projection system with a narrow band laser illumination and a high concentration of fluorescent dye dissolved in the fluid in order to generate fluorescence emission from minimum thickness of the film (i.e. the top few microns). The method relies on calculation of an interference phase term and the modulation depth of the fringes created by means of a twin fibre configuration. The characterisation of candidate fluorescent dyes in terms of absorption, related to the depth of penetration of the incident light into the dye and their fluorescence emission efficiency is presented and their application in full field imaging experiments is evaluated. A strong focus of the technique proposed is its flexibility and versatility allowing its extension to phase stepping techniques applied to determine the (fringe) phase map from static and dynamic fluids. Some experiments are carried out using the best dye solution in terms of fluorescence emission and light depth penetration. On the basis of the phase-height relationship achieved during the calibration process, the proposed measurement system is applied for the shape measurement of some static fluids. The profile of the exterior surface of these fluids is investigated by means of phase-stepping technique and the resolution of the measurements is estimated. Furthermore a flow rig set-up based on inclined system (gravity assisted) is presented in order to test the shape measurement system in presence of real liquid flows. Different liquid flow thicknesses are processed and analysed. Example data will be included from some fluid films of known geometry in order to validate the method.

Table of Contents

Acknowledgements ..... **III**
Abstract ..... **IV**
Table of Contents ..... **V**
List of Abbreviations ..... **VIII**
List of Tables ..... **X**
List of Figures ..... **XI**
Preface ..... **XVI**
Part I Foundations **1**
Chapter 1 The importance of thin films in industry and some applications **2**
1.1 Why thin films? 2
1.1.1 Applications of thin film deposition 3
1.1.2 Thickness and uniformity of thin films 8
1.2 Summary 12
Chapter 2 Thin film experimental applications and film thickness **15**
2.1 Spin Coating process 15
2.2 Thin Film Resistor and multilayer barrier coating structure 16
2.3 Thin liquid films over topographies – The process of planarization 19
2.4 Thin liquid films over topographies – Experimental techniques 20
2.5 Summary 27
Chapter 3 Overview of three-dimensional shape measurement using optical methods **30**
3.1 Optical techniques for 3D shape measurements 30
3.2 Summary 48
Part II Materials and Methods **51**
Chapter 4 New way to measure thin film topography **52**
4.1 Limitations of the previous methods 52
4.2 Fluorescence based fringe projection 53
4.3 Fluorescence: emission and depth of penetration 54
4.3.1 Depth of penetration – Theoretical Analysis via Beer-Lambert Law 54

4.3.2 Depth of penetration
– Experimental approach: flow cell 57
4.3.3 Fluorescence intensity 62
4.4 Summary 68
Chapter 5 Building the optical system 71
5.1 Experimental setup for producing laser based fringes 71
5.1.1 Grating based fringe projection 74
5.1.2 Twin fibre system 79
5.1.3 Noise Analysis: comparison of 3 sets of projected fringes 83
5.2 Improvement of Twin Fibre System
– Thermal Enclosure System 86
5.3 Improvement of Twin Fibre System
– Phase Stepping Algorithm Implementation 89
5.4 Summary 94
Chapter 6 Calibration procedure 98
6.1 Phase-to-height relationship in phase measurement profilometry 99
6.2 Summary 109
Part III Experiments and Results 111
Chapter 7 Experiments on static fluids 112
7.1 Twin fibre system 113
7.2 Phase measurement profilometry 118
7.3 Summary 128
Chapter 8 Experiments on thin film flowing fluids 130
8.1 Description of the experimental set-up 131
8.1.1 Set-up requirements 134
8.1.2 Improvements 137
8.2 Experimental results 142
8.3 Summary 152
Chapter 9 Conclusions and Future Work 155
9.1 Characterization of fluorescent dyes for laser based fringe projection 155
9.2 Imaging system for thin (liquid) film measurement 156
9.3 Experiments on static and dynamic fluids based on phase to height calibration 157

9.4 Outlook 158
9.4.1 System improvements 158
9.4.2 Measurements with different fluid-topography combinations 158
Appendix A 160
Appendix B 163
Index 165

List of Abbreviations

2-D	two-dimensional space
3-D	three-dimensional space
arctan	inverse tangent function
APC	angled physical contact
BNC	Bayonet Neill–Concelman (connector)
BS	beam splitter
CCD	charge-coupled device
DMD	digital mirror device
DRAM	dynamic random-access memory
e.g.	exempli gratia (for example)
ERLIF	emission reabsorption laser induced fluorescence
eV	electron volt
FC	fibre connector
FCFS	first-come, first-served
FFT	fast Fourier transform
FP	fringe projector
FS	fusion splice
IC	integrated circuit
IR	infrared
LED	liquid crystal display
LIF	laser induced fluorescence
M	molar
MEMS	micro-electro-mechanical systems
MOSFET	metal–oxide–semiconductor field-effect transistor
NA	numerical aperture
$N.A._{object}$	numerical aperture object
PL	pellicle beam splitter
PME	phase modulation (ellipsometer configuration)
p.p.m.	parts per million
PZT	piezoelectric transducer
RAE	rotating analyser (ellipsometer configuration)

RCE	rotating compensator (ellipsometer configuration)
RL	red laser spot projector
RPE	rotating polarizer (ellipsometer configuration)
Re	Reynolds number
RMS	root mean square
SEM	scanning electron micrograph
Si	silicon
SM	single mode (fibre)
STD	standard deviation
UV	ultraviolet
VLSI	very-large-scale integration

List of Tables

Table 3.1: Summary of the optical techniques analysed. **47**

Table 7.1: Standard deviation of the residual errors between the unwrapped phase and the fitted phase distributions as a measure of phase noise **122**

List of Figures

Figure 1.1: Applications of thin film deposition..... **3**
Figure 1.2(a-d): Uniform and non-uniform coating **4**
Figure 1.3: Wheatstone bridge configuration **5**
Figure 1.4a: Schematics of a classical solar cell..... **6**
Figure 1.4b: Cross-section of thin film a-Si:H cell..... **6**
Figure 1.5: The Photoelectric Effect..... **6**
Figure 1.6: Different photovoltaic cells show different energy band gaps..... **7**
Figure 1.7: Schematics of polycrystalline thin-film cell..... **7**
Figure 1.8: Schematic of a microchip **8**
Figure 1.9: Micrograph of a tobacco mosaic virus **8**
Figure 1.10: Cross-section of an aerogel **9**
Figure 1.11a: The magnetic recording media **9**
Figure 1.11b: The world's thinnest liquid crystal display (LCD) panel..... **9**
Figure 1.11c: Cross-section of a common CD and time recording..... **10**
Figure 1.12: Sequence of steps for a typical optical lithography process..... **11**
Figure 2.1: Spin coating..... **15**
Figure 2.2: Single layer thin film and its application as film thermometer **17**
Figure 2.3: Typical multilayer barrier coating structure and its application in thin film photovoltaic cells **18**
Figure 2.4: VLSI circuit dimensions..... **18**
Figure 2.5: Outline of topographic planarization..... **20**
Figure 2.6: Predicted thin film flow over a single, square trench..... **21**
Figure 2.7: Twyman-Green interferometer..... **21**
Figure 2.8: The characteristic dimensions of the corrugated wall **23**
Figure 3.1: Schematics of the triangulation principle..... **31**
Figure 3.2: Projection moiré where fringes or a grating are projected onto a surface and viewed through a second grating **32**
Figure 3.3: Relationship between collected data and the recovered image **33**
Figure 3.4: Some fringe projection schemes..... **34**
Figure 3.5: Layout of diffractive fringe projection interferometer **35**
Figure 3.6: The optical geometry of projection unit **36**
Figure 3.7: Particular of the fringe pattern projected on an ancient roman coin **36**

Figure 3.8: Fluorescence principle **37**

Figure 3.9a: Application of Snell's law **39**

Figure 3.9b: Polarization states **39**

Figure 3.10: Ellipsometry, basic principle **40**

Figure 3.11: The concept of extinction coefficient **41**

Figure 3.12: Application of Ellipsometry on multi-layered structures **42**

Figure 3.13: Schematics of Ellipsometer in RAE configuration **42**

Figure 3.14a: Dynamic interferometer **45**

Figure 3.14b: Four phase shifted interferograms on detector are obtained thanks to the grating/mask **46**

Figure 4.1: Schematics to illustrate the Beer-Lambert law **55**

Figure 4.2: Comparison between the absorption of three candidate fluorescent dyes (molar absorptivity vs wavelenght) **56**

Figure 4.3: Comparison between the absorption of three candidate fluorescent dyes (% absorbed light vs path lenght) **56**

Figure 4.4: Schematic diagram of the system adopted to estimate the depth penetration into the fluorescent solution when the dye concentration is near the saturation level **58**

Figure 4.5: Schematic representation of flow cell device filled up with a saturated solution of DCM special in methanol exposed to the laser light **59**

Figure 4.6: Light penetration depth for Sulforhodamine 640 dissolved in water (left), methanol (right). **60**

Figure 4.7: Fluorescence penetration depth for a saturated solution of Rhodamine B in ethanol **60**

Figure 4.8: Comparison between theoretical (Beer's law) predictions and experimental results for a dye solution of Sulforhodamine 640 in methanol **61**

Figure 4.9: Fluorescence emission spectra for Rhodamine B chloride (in ethanol) and Sulforhodamine 640 (in methanol). **62**

Figure 4.10: Schematic diagram of the proposed fluorescence detection system **63**

Figure 4.11: Measured transmission spectrum for the long pass filter (568 nm) used for the fluorescence detection **64**

Figure 4.12: Emission of fluorescence for Rhodamine B (in ethanol) and Sulforhodamine 640 (in methanol) dyes **65**

Figure 4.13: Showing the average fluorescence intensities and the depth of penetration for the different combinations of dye-solvent examined. **67**

Figure 5.1: Schematics of projected fringes system **72**

Figure 5.2: Constructive and destructive interference **73**

Figure 5.3: Geometry determining the conditions for diffraction from a multi-wire grating **74**

Figure 5.4a: Geometry of diffraction orders **75**

Figure 5.4b: Image of 0th and 1st order diffraction **75**

Figure 5.5: Definition of system parameters **76**

Figure 5.6: Geometry of grating fringe illumination system **77**

Figure 5.7a: Practical fringe projection system with grating **78**

Figure 5.7b: CCD camera spectral response **78**

Figure 5.8: Fringe pattern **79**

Figure 5.9: Michelson interferometer **79**

Figure 5.10: A twin fibre based fringe projector **80**

Figure 5.11: Experimental image showing fringe pattern **81**

Figure 5.12: The above plot relates to the grating system with two and three microscope objectives **84**

Figure 5.13: Loss of monotonicity in the unwrapped phase **85**

Figure 5.14: Twin fibre system (right) shows a noise level lower than 2 objective (middle) and 3 objective (left) grating system setups **85**

Figure 5.15: Fringe projection configuration **87**

Figure 5.16: The optical setup used for the experiments **88**

Figure 5.17: Modulation of phase difference **90**

Figure 5.18: Synchronization sequence **91**

Figure 5.19: Phase shift accuracy **92**

Figure 5.20: The schematic diagram summarizes the main steps of the phase stepping process **93**

Figure 6.1a: Schematic diagram of the fringe projection profilometry system **98**

Figure 6.1b: Final step: phase-to-height calibration of the measurement system **98**

Figure 6.2: Schematic of the measurement system **99**

Figure 6.3: The schematic shows the effect of field curvature in the optical system **100**

Figure 6.4: Showing the basic concept of N.A. object compared to N.A. of an optical system **101**

Figure 6.5: Calibration procedure **102**

Figure 6.6: Diagram of pellicle (a very fine, 2 μm thick membrane) beam splitter operation **102**

Figure 6.7: Image acquisition **103**

Figure 6.8: The projected spot on the unwrapped phase map **104**

Figure 6.9: MOSFET transistor as a switch (ON/OFF) to control the Red Laser spot projector (RL) **104**

Figure 6.10: Reconstructed planes of calibration (z-scale in microns) **106**

Figure 6.11: Standard deviation (STD, in microns) for the previous planes of calibration **107**

Figure 6.12: The average standard deviation (for the six calibration planes) is less than 2 microns **108**

Figure 7.1: The practical system architecture proposed **113**

Figure 7.2a: Microscope slide with a single convex cavity **114**

Figure 7.2b: A sandwich structure of two microscope slides with the dye solution in the middle **114**

Figure 7.2c: Typical dimensions of the sandwich structure of two microscope slides **114**

Figure 7.3: Fluorescent fringe pattern **115**

Figure 7.4a: Fringe separation ≈ 700 μm, fringe depth from camera ≈ 990 μm ... **116**

Figure 7.4b: Fringe separation ≈ 500 μm, fringe depth from camera ≈ 700 μm ... **116**

Figure 7.5: The unwrapped phase along a row brings out the non-flat surface **116**

Figure 7.6: The fringe pattern shows the presence of non-flat surface **117**

Figure 7.7: Instantaneous interferogram **118**

Figure 7.8: Phase shifted interferograms **119**

Figure 7.9: Wrapped phase estimated using the 4 shifted interferograms **120**

Figure 7.10: Unwrapped phase map **121**

Figure 7.11: Fringe projector (FP) block and rig (open-top vessel) used in the present study **123**

Figure 7.12a: Cross section of a measured profile of a (liquid) surface, positioned at z = 98 microns **123**

Figure 7.12b: The standard deviation (STD) for the previous surface profile **124**

Figure 7.13: Schematic showing the clear glass flow cell and the 100 μm thick blade, from a calibrated feeler gauge, used for the thickness measurement. **125**

Figure 7.14: Wrapped phase map in presence of the 100 μm metal thickness and without **126**

Figure 7.15a: A Matlab visualization of the two unwrapped phase maps **126**

Figure 7.15b: Cross-section of the two unwrapped phase maps **127**

Figure 7.16: Cross section of the two measured profiles **127**

Figure 8.1: The practical flow rig set-up developed **132**

Figure 8.2a: Side view showing (in green) the height of the exit of feeding slit ... **133**

Figure 8.2b: A_B and C_D steps define the geometry of feeding slit **134**

Figure 8.3: Showing the relationship between thickness of the film and height of reservoir once the angle (α) the slit makes with the horizontal is known **136**

Figure 8.4: Schematic design of the inclined support showing the glass plate..... **137**

Figure 8.5: Illustration of wettability for three different solvents..... **138**

Figure 8.6: Layout showing the typical set-up configuration adopted during the experiments **139**

Figure 8.7: The plot shows, for the same reservoir height, H the variation of asymptotic fluid thickness, h∞ when the slit height changed, d. **140**

Figure 8.8a: Estimation of the fluid thickness **141**

Figure 8.8b: Projected spot and its image coordinates **142**

Figure 8.9a: The case of a gravity driven flow over the topography..... **143**

Figure 8.9b: The 2-D plot shows the relative height against the columns (pixels) of the whole image..... **144**

Figure 8.9c: Showing the result of 10th order polynomial fit applied to the data of Figure 8.9b **145**

Figure 8.10a: Full field of view of the reconstructed 3D surface..... **146**

Figure 8.10b: Showing the result of polyfit and polyval functions (10th order polynomial fit) applied to every single row of the above 3D plot **147**

Figure 8.11: Showing the result of polyfit and polyval functions (10th order polynomial fit) applied to every single row of the 2D raw data plot. **150**

Figure 8.12: 3D reconstructed surface plots for the raw data and the post-processed data by means of a 10th order polynomial fit..... **151**

Preface

In recent years, thin liquid film science has grown world-wide into a major research area. The importance of coatings and the synthesis of new materials for industry have resulted in a tremendous increase of innovative thin film processing technologies. Currently, this development goes hand-in-hand with the explosion of scientific and technological breakthroughs in microelectronics, optics and nanotechnology: this technology can well be regarded as a major key to the creation of devices such as computers, since microelectronic solid-state devices are widely based on material structures created by (liquid) thin-film deposition.

These films are essential for a multitude of production areas; examples include (Chapter 1): problems concerning heat dissipation in electronic circuits, photolithographic production of displays, for producing bacterial arrays in bio-films. The list is seemingly endless, comprising latterly the rapidly evolving area of micro-fluidics, with the need to control the flow on an ever decreasing scale in the context of laboratory-on-chip devices.
Another important reason for the rapid growth of thin film technology is the improved understanding of the physics and chemistry of films, surfaces, interfaces, and microstructures. A better fundamental understanding of materials leads to expanded applications and new designs of devices that incorporate thin fluid films.

Currently, the search for thin film materials is creating new opportunities for the development of new devices (for example bio-films, flexible thin film solar cells) and the improvement of technologies (e.g. photolithography for nano-electronic devices, 4-D technology for the study of dynamic motion of surfaces).
In addition, the importance of the shape followed by a thin liquid film flowing over a topography has grown in parallel to the increasing number of thin film devices that are developed. Industrial fields as different as microelectronics, displays, optical data storage or bio-devices all require an understanding of thin fluid film deposition.
In most of these devices, many layers are successively deposited, lithographically patterned and developed.

As the coating fluid flows, for example by spin coating (Chapter 2), its properties will be influenced by the previous thin film layers, their thickness and uniformity.

Therefore, basic research activities will be necessary in the future, to increase understanding of thin fluid films on different topographic patterns and, at the same time, to ensure predictable product properties in terms of performance of thin films in various technological processes for films with thicknesses ranging from a few nanometers to several hundred microns.
In addition there is a strong need for accurately measuring the 3-D shape of objects and film thickness (Chapter 3) to speed up and ensure product development and manufacturing levels of quality.
However current techniques show significant limitations for metrology of thin liquid films (Chapter 4).

Hence, informed by an extensive literature review, the **main aim** of this work is:

- to compare existing techniques compatible with thin fluid films for the measurement of the surface profile and their thickness (Chapter 2 and 3);

- to describe and characterize the use of candidate fluorescent dyes in order to present a technique based on suitable fluorescent dyes for measuring the surface topography of thin fluid films by fluorescence based fringe projection (Chapter 4 and 5);

- to show that this technique (Chapter 5) can give a satisfactory solution in terms of resolution and stability of the images;

- to build (Chapter 5) a fully tested system for thin film measurement based on a twin fibre based fringe projector (by means of a 200 mW laser at 532 nm);

- to improve the twin fibre configuration against the environmental instabilities (*thermal enclosure system*, Chapter 5);

- to adopt this thermally isolated setup for fast acquisition of temporal phase stepped (LabView code) in order to determine the fringe phase map from static and dynamic fluids (Chapter 5);

- to find a relationship between the modulated phase distribution in the projected fringe patterns and the height of the object under test (Chapter 6, *calibration procedure*);

- to familiarize with the technique developed , based on fringe projection using fluorescent dye solutions, focusing attention on the study of fluids in the static condition by means of the phase stepping technique (Chapter 7);

- to build a flow rig set-up (Chapter 8) in order to test the shape measurement system and validate the proposed method in presence of real liquid flows over topography of known geometry;

Part I

Foundations

Chapter 1

The importance of thin films in industry and some applications

1.1 *Why thin films?*

Thin film, free surface coating flows over surfaces containing topography/patterning (localised or uniformly distributed) occur in many branches of engineering and the high-tech manufacturing industries, as well as having several medical applications. Typically thin films (ranging from fractions of a nanometre to several hundred micrometres in thickness) are deposited onto a metal, ceramic, semiconductor or plastic base.
The study of surface topography/patterning and the flow over it plays a fundamental role in different research fields as described below.

a) With the rapid development of microelectronics, thin films are important in problems concerning heat dissipation in electronic circuits **[1]**; in addition they improve safety in shipping, aircraft and power transmission by limiting rates of ice accretion **[2]**; and take part in a prime example of biomimetics **[3]**, the lotus effect (very high water repellency, “super-hydrophobicity”, exhibited by the leaves of the lotus flower).

b) Thin films have a strong influence in medical applications: they influence the effectiveness of membrane blood oxygenators in extra-corporeal systems **[4]**; in the lung, films affect the redistribution of liquid lining the airways **[5]**; in the eye it can influence the effectiveness of tear films flowing over the cornea **[6]**.

c) Thin films are present in a range of microelectronic components, for example in the photolithographic production of displays, where film thickness control of successive photo-resist layers over topographies is key **[7]**; they are a vital component of nano-patterned substrates with beneficial adhesion properties for producing bacterial arrays in bio-films, and are used in toxicity monitoring and in fast screening of infectious diseases **[8]**.

1.1.1 *Applications of thin film deposition*

The above applications range in thickness from 22 nm (transistor gate lengths in microelectronics, from Intel **[9]**) to 700 μm (substrate of larger displays **[10]**). The spatial extent of the surfaces is between 50μm (bacterial arrays diameter in bio-films) and 550× 650-mm (third generation flat panel displays **[10]**).

In order to gain an insight into the Thin Film Industry it is useful to look at the applications of thin film deposition (Figure 1.1): a lot of the applications appear to be in research or high tech industries and hence rapid commercial growth might be expected.

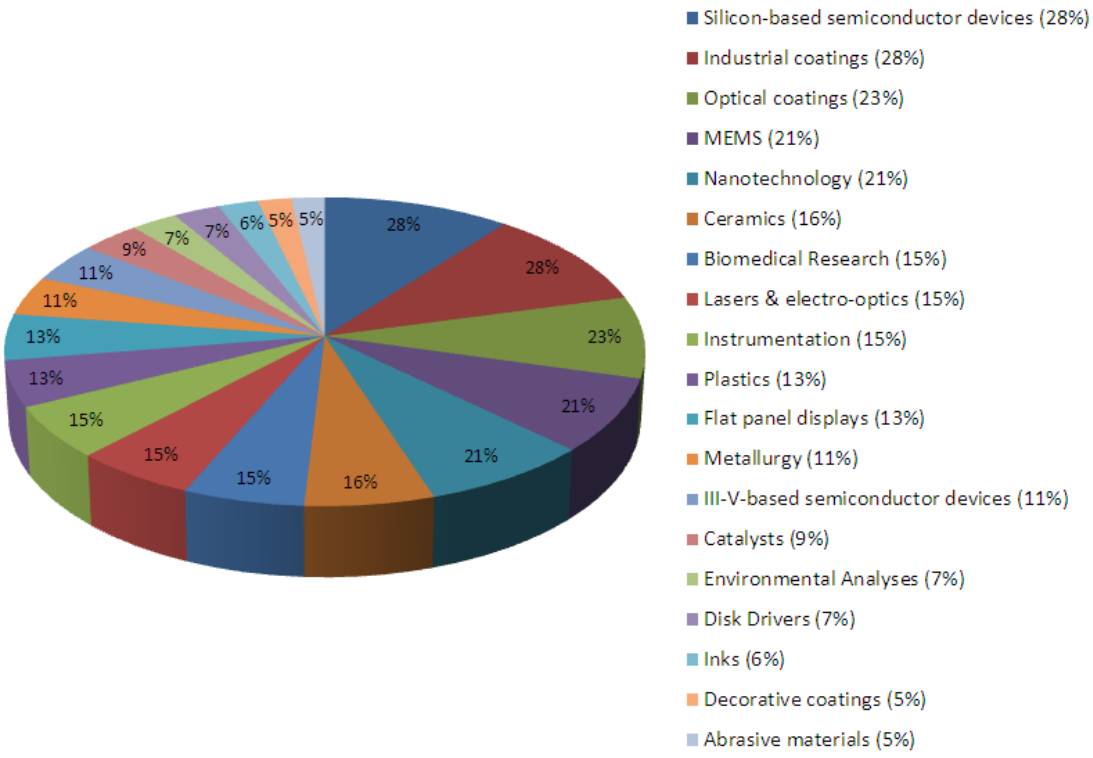

Fig. 1.1: Applications of thin film deposition (Percentages are from *R&D Magazine, March 2001* voluntary survey)

In precision manufacturing industries the industrial goal is often that of minimising the free surface disturbances caused by the presence of topographic features so as to ensure predictable product properties. A good example is the application of thin coatings (which need to be uniform) on flat substrates like TVs or electronic displays used for interfacing electronic equipment with human operators. The result of this operation depends on how clean the substrate is.

For example if there is an anti-reflection coating on a TV (Fig. 1.2, a-d), then if the coating is not uniform one will get glare (e.g. from the sun) in regions where the coating thickness is not correct (e.g. see Figure 1.2d).

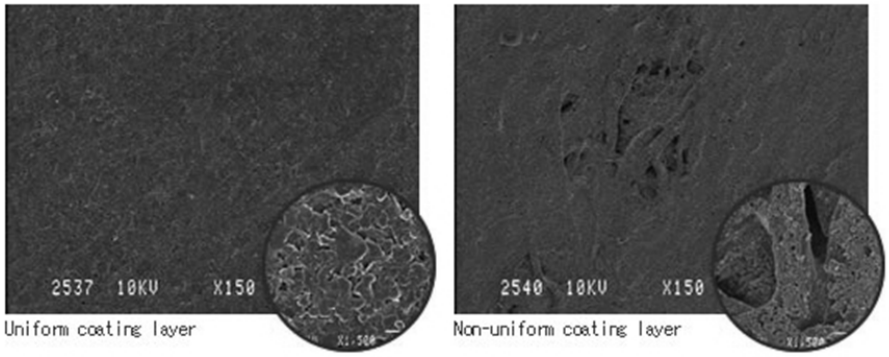

a) Portion of uniform coating layer **b)** Coating showing non-uniform areas

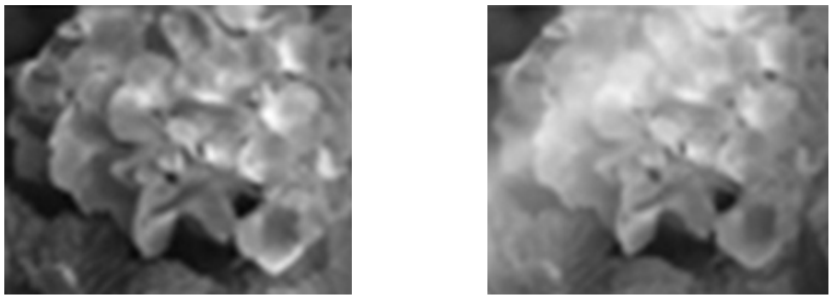

c) Test image with uniform coating layer **d)** Same test image but in presence of non-uniform coating

Figure 1.2(a-d): Uniform and non-uniform coating.
The sequence of images shows the difference between uniform coating (a) and non-uniform coating (b) on a display. The effect on a test image is shown in presence of (c) uniform coating and (d) non-uniform coating (scanning electron micrograph (SEM), from Nippon Paper Group).

In other words, the presence of disturbances on the surface of the substrate leads to variations in the film thickness and as the fluid flows over the disturbance the wake produced can extend 10's of mm giving large areas of the product that have faults.
In addition, the strong requirement for providing a link between analogue and digital information has produced new and pressing requirements for precision integrated resistive networks on a single substrate (chip). For example, the measurement of temperature, strain and pressure is frequently accomplished using resistive sensors, such as thermistors and strain gauges, in voltage dividers formed with resistors.
Often, these sensors, and their accompanying bias resistors, must operate over a broad temperature range.

It is not uncommon to require a maximum operating temperature of 125 °C. Typically, a Wheatstone bridge is the source of the output voltage (Figure 1.3):

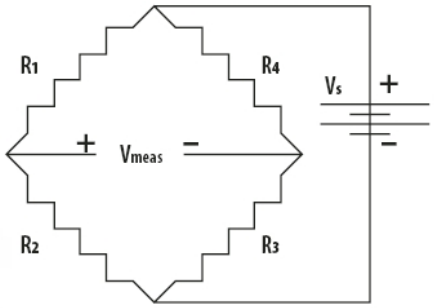

Figure 1.3: Wheatstone bridge configuration

The output voltage from the Wheatstone bridge is given by the following equation:

$$Vmeas = Vs\{R_2 \div (R_1 + R_2) - R_3 \div (R_3 + R_4)\}$$

In Figure 1.3, R_1 and R_4 are biasing resistors, which act as the reference half of the voltage dividers formed with the two sensing resistors, R_2 and R_3, respectively.

The matching of R_1 to R_4 directly affects the accuracy of the output voltage.

Since R_2 and R_3 are sensors, their resistive values change in response to physical input. Therefore, the higher the initial precision (ratio match) of R_1 and R_4, the more accurately the output voltage will depict the sensor readings.

The electrical and mechanical stability of the films is one of the features which distinguishes modern thin film technology. This is important because closely trimmed resistors must tolerate some stressful conditions of assembly without significant drift. The advantages of integrated construction over individual discrete resistors become clear: any changes which do occur will be common to all resistors in the network, thus preserving the ratios precisely as trimmed **[11]**.

For example, the typical tolerance of a thin film resistor is 0.01 %; the best discrete resistors achieve a resistor tolerance of 0.5% **[11]**.

In the last twenty years much research had been focused on making solar cells cheaper and more efficient in order to effectively compete with other energy sources. Solar cells are particularly suited to situations where electrical power from a classical electricity network is not available, e.g. to provide power for Earth orbiting satellites, water pumps, power systems and traffic signs.

In the light of this thin film science has a dual role: to reduce the amount of light absorbing material required in creating a solar cell on one hand (Fig. 1.4a, **[12]**) and

to improve the energy conversion efficiency by adopting several multi-layer thin films (Fig. 1.4b, **[13]**) having efficiencies above those of bulk silicon wafer on the other.

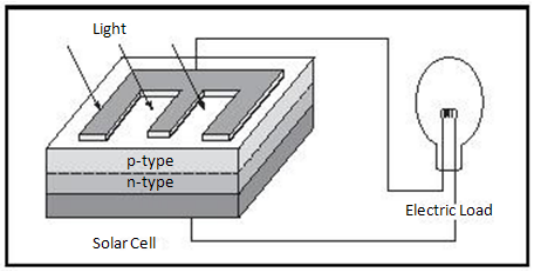

Fig. 1.4a: Schematics of a classical solar cell **[12]**

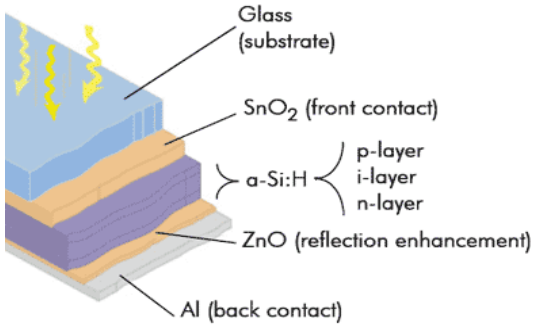

Fig. 1.4b: Cross-section of thin film a-Si:H cell **[13]**

The photoelectric effect (Figure 1.5, **[13]**) is the basic physical process by which a photovoltaic cell converts sunlight into electricity: the energy of the absorbed light is transferred to electrons in the atoms of the cell. These electrons can escape from their normal positions in the atoms of the semiconductor. To produce an electric current it needs to provide a quanta of energy (incident photons) enough to free electrons in the semiconductor material (Figure 1.6, **[13]**). This energy is known as the "bandgap energy". To make an efficient solar cell, it necessary that the films thickness and materials optical constants are as uniform as possible.

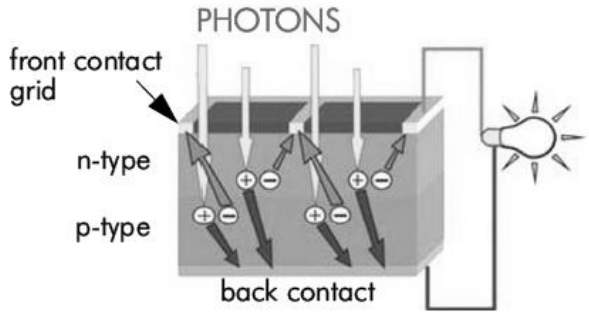

Figure 1.5: The Photoelectric Effect **[13]**

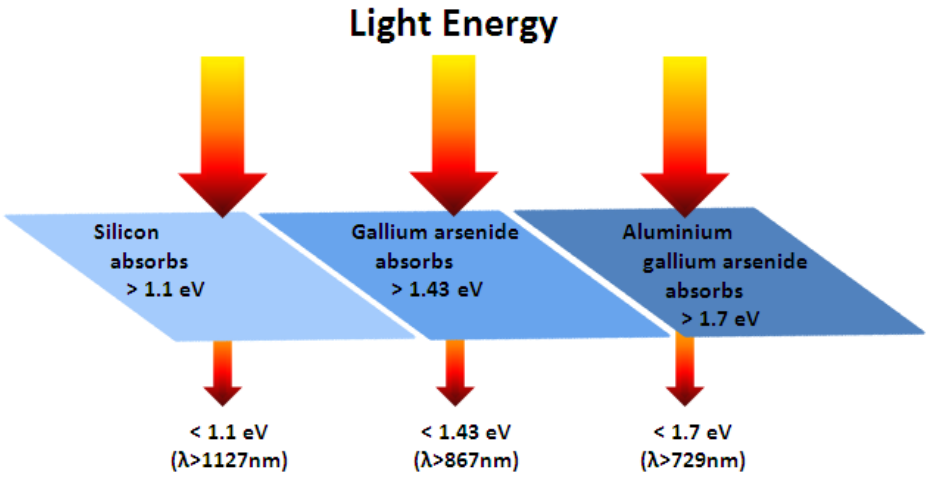

1.6: Different photovoltaic cells show different energy band gaps **(**adapted from **[13])**. Only when photons energy matches the band gap energy it possible to generate free electrons. Photons with energy less than band gap energy pass right through the material (no electricity generation).

If one considers the whole spectrum of sunlight, from infrared to ultraviolet, the energy of a photon ranges between 0.5 eV to about 2.9 eV. Usually 55% of solar energy can't be used because this energy is below the bandgap of the material **[14]**. Unlike a standard single-crystal cell, a thin film can use much less material: usually the active area is only 1 to 10 μm thick while thick films are 100 to 300 μm thick.

The main problem is that a typical thin film cell has a "window" (that's a thin, less than 0.1 μm, layer) on top needed to absorb light energy from only the high-energy end of spectrum. This layer must be thin enough to let light through and, at the same time, have a wide bandgap (2.8 eV or more). In addition silicon can act as a mirror reflecting more than 30% of the incident light: single or multiple antireflection coatings help to optimize light absorption reducing undesirable reflections (Fig. 1.7).

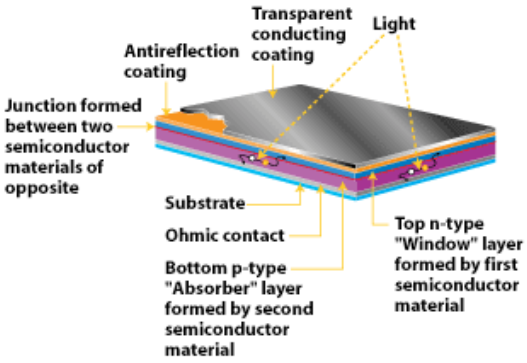

Figure 1.7: Schematics of polycrystalline thin-film cell (courtesy of U.S. Department of Energy - Energy Efficiency and Renewable Energy)

1.1.2 *Thickness and uniformity of thin films*

It is interesting to notice that current trends in the industry are to produce components, e.g. as microchips (Figure 1.8, **[15]**), having non-uniform exterior surfaces but require to be covered by uniform coatings.
Such applications span the range of structures from DRAM trench cells and MEMS (micro-electro-mechanical systems) devices to coatings of esoteric materials such as nanotubes, 3-D nanostructures of viruses (Figure 1.9, **[16]**), microlenses, piping, grains and particles, and even porous dental material **[16]**.

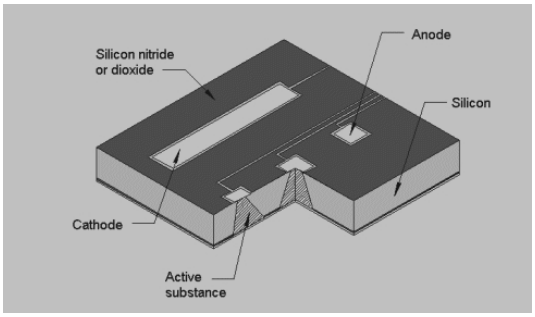

Fig. 1.8: Schematic of a microchip **[15]**

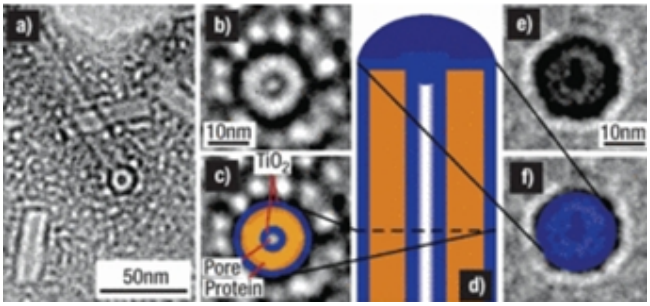

Fig. 1.9: Micrograph of a tobacco mosaic virus **[16]**: a 300 nm long tobacco mosaic virus (a, b) is used as template for creating the final structure**.** Following the deposition of TiO_2 (c-e) the template for 3D nanostructures is ready (f)**.**

Another example of an application with strong potential for industrial uses is the coating of aerogels (Figure 1.10, **[16]**). These extremely low density materials are produced by drying gels in such a manner as to remove their liquid content, while leaving the solid matrix of material behind. This results in extraordinarily porous material with a supporting structure, whose properties make them particularly suitable as an insulator, desiccant, and in load-bearing applications **[16]**.
Silica is the most common type of aerogel **[17]**.

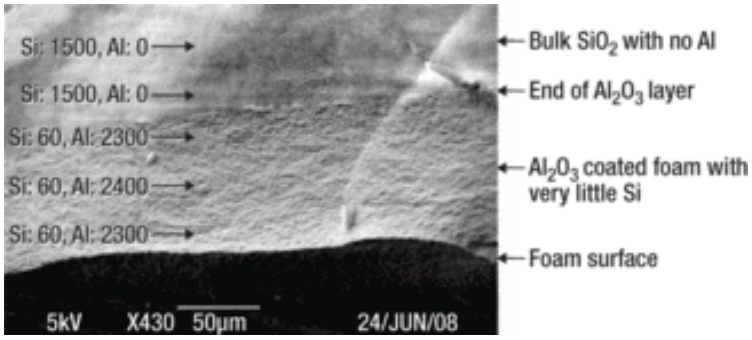

Figure 1.10: Cross-section of an aerogel **[16]**

A common method for forming thin films on a surface is *spin coating*. Spin coating applications include the manufacture of magnetic disks, lens coatings, reflectors, and liquid crystal displays (e.g. see Figure 1.11, a-c).

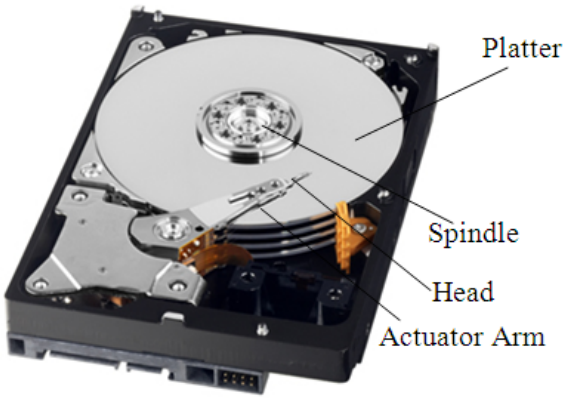

Figure 1.11a: The magnetic recording media (platter) are thin films of about 10-20 nm in thickness (adapted from **[18]**)

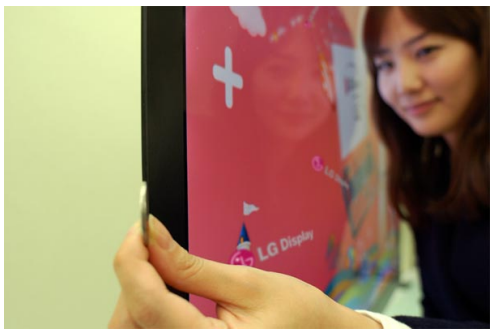

Figure 1.11b: The world's thinnest liquid crystal display (LCD) panel (42 inches wide, 2.6 mm thick, courtesy of LG **[19]**)

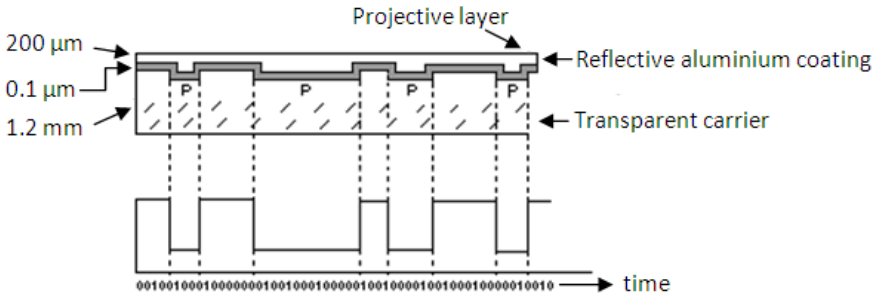

Figure 1.11c: Cross-section of a common CD and time recording (adapted from **[20]**)

In semiconductor manufacturing, the ability of spin coating to produce thin, uniform films makes this a fundamental process. In this context, the importance of topographic substrate planarization with films applied by a spin-coating process was reported in the works of L. E. Stillwagon and R. G. Larson **[21, 22]**: a theory was developed in order to relate the time required to level the topographic gaps to their width and to the thickness and viscosity of the film.

A particularly important semiconductor application includes forming thin resist films in photolithography: a photographic process by which a light-sensitive polymer, called a photoresist, is exposed and developed to form 3D relief images on the substrate. In general, the photoresist image has (ideally) the exact shape of the designed pattern in the plane of the substrate, with vertical walls through the thickness of the resist. The final resist pattern has parts of the substrate covered with resist while other parts are completely uncovered.

This final pattern is needed for pattern transfer since the parts of the substrate covered with resist will be protected from etching, ion implantation, or other pattern transfer mechanisms (Figure 1.12, **[23]**).

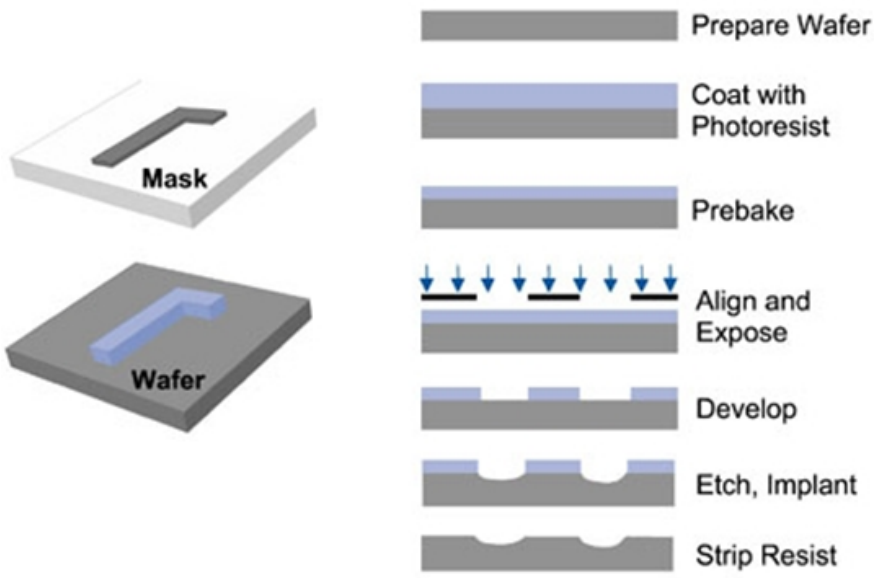

Figure 1.12: Sequence of steps for a typical optical lithography process **[23]**

In the semiconductor industry the two film properties, film thickness and uniformity, correlate directly with lithography resolution. The processing parameters known to affect these include liquid viscosity, solute concentration, drying rate, gas flow above the wafer, and wafer rotation. Another important parameter affecting film quality is substrate surface topography. It remains a need to improve methods for forming spin-coated films, particularly on substrates having a non-uniform surface topography.

For example, non-uniformities may include surface features having a height up to about 10 μm **[24]**. Further developments in microelectronics (improvement of power dissipation, increase of computing power for the same energetic consumption) will depend on lithography and the ability to make thin films on topographically non-uniform substrates.

1.2 *Summary*

This chapter has introduced the concept of thin film (free surface coating flows over surfaces containing topography/patterning) and some applications of thin film deposition in different branches of science. In particular, the study of surface topography and the flow over it plays a fundamental role in different research fields from microelectronics to applied medicine. The applications of thin film deposition show tremendous potential for developing advanced electronic devices ranging from few nanometers (silicon-based semiconductor devices) to a few hundred microns (substrate of larger electronic displays).

Current trends in the industry are to produce components, e.g. as microchips, having non-uniform exterior surfaces (required for the functionality of the device) but require to be covered by uniform coatings. For instance, methods for forming spin-coated films on substrates having a non-uniform surface topography. The final result depends on the thickness uniformity of the thin films deposited. Hence, it is necessary to gain a deeper understanding of the mechanisms leading to non-uniformities of the free surface and how to control undesired defects.

The next chapter will provide a more detailed description of some theoretical approaches and thin film experimental applications.

Chapter references

[1] DARHUBER AA and TROIAN SM (2005). Principles of Microfluidic Actuation by Modulation of Surface Stresses. *Ann. Rev. Fluid Mech.* **37**, 425-455.

[2] MYERS TG, CHARPIN JPF and THOMPSON CP (2002). Slowly accreting ice due to supercooled water impacting on a cold surface. *Phys. Fluids* **14**(1), 240-256.

[3] VINCENT JFV, BOGATYREVA OA, BOGATYREV NR et al. (2006). Biomimetics: its practice and theory. *J. R. Soc. Interface* **3**(9), 471–482.

[4] ABU-RAMADAN E and KHAYAT RE (2005). Shear-thinning flow in weakly modulated channels. *Int. J. Numer. Meth. Fluids* **48**(5), 467-499.

[5] ROSENZWEIG J and JENSEN OE (2002). Capillary-elastic Instabilities of Liquid-lined Lung Airways. *J. Biomech. Eng.* **124**(6), 650-655.

[6] BRAUN RJ and FITT AD (2003). Modelling drainage of the precorneal tear film after a blink. *Math. Med. Biol.* **20**(1), 1-28.

[7] MIDDLEMAN S and HOCHBERG AK (1993). Process Engineering Analysis in Semiconductor Device Fabrication. New York: McGraw-Hill (ISBN: 0070418535).

[8] YOO SK, LEE JH, YUN SS et al. (2007). Fabrication of a bio-MEMS based cell-chip for toxicity monitoring. *Biosensors & Bioelectronics* **22**(8), 1586-1592.

[9] Intel® 22nm Technology. Introducing the world's first 3-D transistor ready for high-volume manufacturing.
Available from http://www.intel.co.uk/content/www/us/en/silicon-innovations/intel-22nm-technology.html (Accessed: 27/05/2013).

[10] SHEETS RE (Spring 1996). Scanning projection for large-area lithography. *MICROLITHOGRAPHY WORLD Magazine*.

[11] VISHAY INTERTECHNOLOGY, INC. Precision Thin Film Technology. Available from http://www.vishay.com/docs/49562/49562.pdf (Accessed: 27/05/2013).

[12] BUBE RH (1988). Photovoltaic Materials. London: Imperial College Press (ISBN: 9781860940651).

[13] Characterization of Photovoltaic Devices by Spectroscopic Ellipsometry. Available from: http://www.intercovamex.com (Accessed: 27/05/2013).

[14] BÖER KW (2002). Survey of Semiconductor Physics. New York: John Wiley & Sons Inc. (ISBN: 0471355720).

[15] SANTINI JT, CIMA MJ and LANGER R (1999). A controlled-release microchip. *Nature* **397**(6717), 335-338.

[16] SUNDARAM GM, DEGUNS EW, BHATIA R et al. (2009). Thin Films for 3D: ALD for non-planar topographies. *Solid State Technol.* **52**(14).

[17] KISTLER SS (1932). Coherent Expanded Aerogels. Rubber Chemistry and Technology. *J. Phys. Chem.* **5**(4), 600-603.

[18] Western Digital: Internal Desktop Hard Drives Overview. Available from http://www.wdc.com/it/products/products.aspx?id=770 (Accessed: 27/05/2013).

[19] Thinnest Large-Screen LCD Panel is 2.6mm Thick. Available from http://www.ecnmag.com/news/2009/12/thinnest-large-screen-lcd-panel-26mm-thick (Accessed: 27/05/2013).

[20] How do optical discs work? Available from http://cdman.com/how-do-optical-discs-work (Accessed: 27/05/2013).

[21] STILLWAGON LE, LARSON RG and TAYLOR GN (1987). Planarization of Substrate Topography by Spin Coating. *J. Electrochem. Soc.* **134**(8), 2030-2037.

[22] STILLWAGON LE and LARSON RG (1990). Leveling of thin films over uneven substrates during spin coating. *Phys. Fluids* **A2**, 1937-1944.

[23] MACK CA (2006). Field Guide to Optical Lithography. Bellingham, WA: SPIE Press (ISBN: 0819462071).

[24] YAJI W (2007). Method for forming a resist film on a substrate having non-uniform topography. US Patent 7199062.

Chapter 2

Thin film experimental applications and film thickness

2.1 *Spin Coating process*

As discussed at the end of the previous chapter, two film properties correlate strongly with lithography resolution: film thickness and uniformity. In addition, the final result depends directly on substrate surface topography. In particular, current trends are to produce components containing non-uniform topography (i.e. they possess a non-uniform exterior surface). Hence for structures like microchips, uniform coatings (i.e. uniform coatings in thickness) need to be generated on top of non-uniform topographies.

Strategies are required to improve the specification of spin-coated films, particularly on substrates having a non-uniform surface topography. To understand the typical problems that occur in manufacture it is useful to give an example: in semiconductor manufacturing, a common method for forming thin films on a surface is *Spin coating* (Figure 2.1).

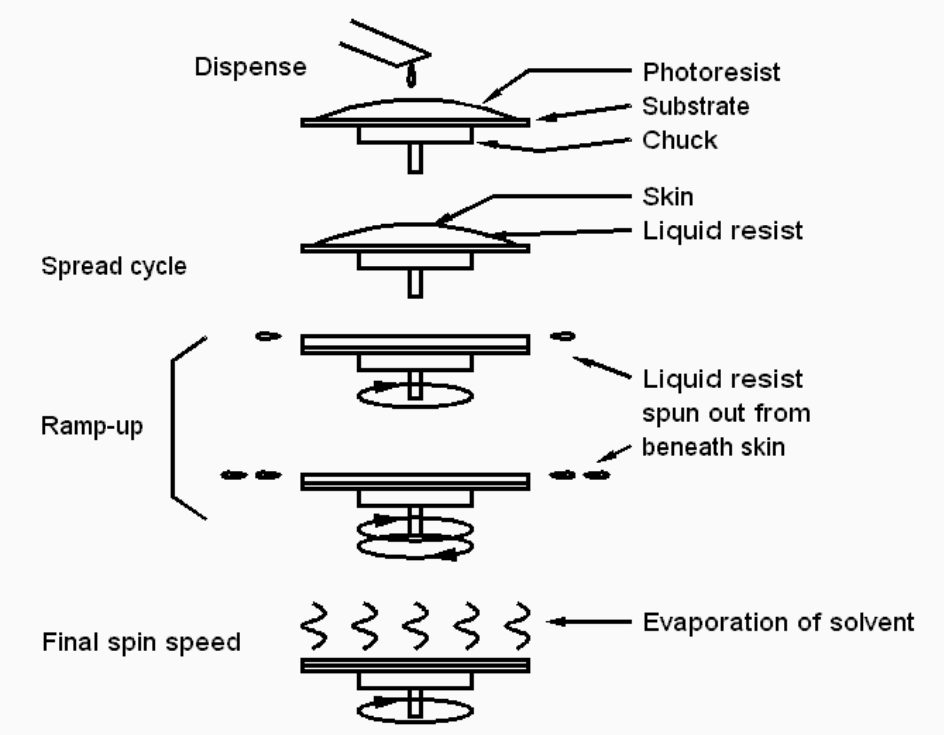

Figure 2.1: Spin coating (adapted from **[25]**)

In this process (typically in applications of IC lithography), it is common to use a liquid resist that is comprised of a non-volatile material dissolved in a volatile solvent. Above a spinning substrate, such as a wafer, this liquid resist is dispensed, usually close to its centre. The wafer is put in rotation until it reaches its final spinning velocity: centrifugal forces cause much of the liquid to flow off the substrate surface. The process goes on until the volatile solvent evaporates in order to concentrate the non-volatile material dissolved in the resist.

The reduction of the thickness of the liquid film (on the spinning wafer) is the effect of solvent evaporation and liquid spin off. As the liquid film becomes thinner, the viscous forces become increasingly dominant. At the end, as the viscous forces balance the centrifugal forces, it is possible to produce an extremely thin film on the surface of the wafer. The range of film thicknesses easily achieved by spin coating is 1-200 μm **[26]**. For thicker films, high material viscosity, low spin speed, and a short spin time are needed. However, these parameters can affect the uniformity of the coating. Multiple coatings are preferred for a film thickness greater than 15 μm **[27]**.

Equipment manufacturers are aware that surface topography may produce flow "anomalies" in the resist during spin coating process. In particular, the effect of these anomalies can lead to resist accumulation on one side of the surface feature and depletion on the opposite side. In addition, this problem becomes stronger as the distance from the centrifugal centre of the substrate increases. Therefore, the same thickness of the coating, on adjacent features, is influenced by changing even a single topographical feature. Often these problems are particularly visible in those regions situated seemingly far from the changed feature (or substrate imperfection) on a line extending from the centrifugal centre.

2.2 *Thin Film Resistor and multilayer barrier coating structure*

In the light of the above, the industrial goal is often that of minimising the free surface[1] disturbances caused by the presence of topographic features in order to ensure the stability and repeatability of the process.

([1]) The shape of the air–liquid interface of a (thin) liquid film

This is of considerable importance, especially in the large-scale manufacturing of semiconductor devices.

Of increasing importance is to guarantee, particularly in the fabrication of high-density microelectronic devices, the uniformity (in thickness and composition) of the deposited films in order to achieve acceptable standards for device manufacturing. To gain an insight into the typical dimensions one can consider a thin film application known as the “Thin film Resistor”: resistor material (Tantalum nitride) with a size of 100 μm square and with 2 to 15 μm thickness is deposited on a plain ceramic substrate, for example in the fabrication of film thermometers (Figure 2.2).

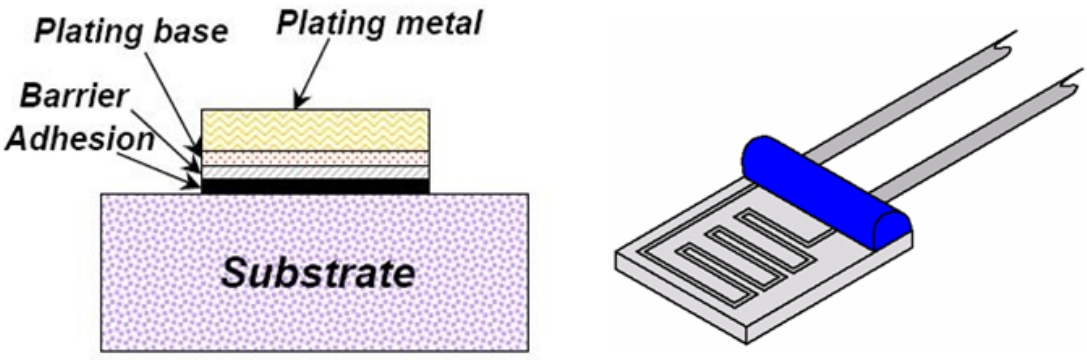

Figure 2.2: Single layer thin film and its application as film thermometer (courtesy of NGK SPARK PLUG CO.)

It is easy to imagine what happens if this metal deposition is not uniform, for example as a consequence of deformations of the metal pattern or substrate irregularities: unpredictable heating of the resistor and even cracking (failure) on soldering. However, continuous evolution drives precision manufacturing industry toward even thinner, lighter and more flexible components. Although huge progress has been demonstrated, a fundamental obstacle is the sensitivity of the electronics components to environmental factors, primarily moisture and oxygen. The conventional encapsulation solutions, using a glass/metal can with desiccant, tends to increase weight, thickness and cost of fabrication. Therefore, in order to maintain a thin and flexible form, these devices are protected by a barrier dielectric layer against damage caused by moisture and oxygen.

Recent applications make use of a multilayer thin film barrier for protection of flex-electronics as thin film photovoltaic panels (Fig. 2.3, **[28]**): some layers of polymers are deposited in liquid form and, by UV processing, achieve a plastic behaviour.

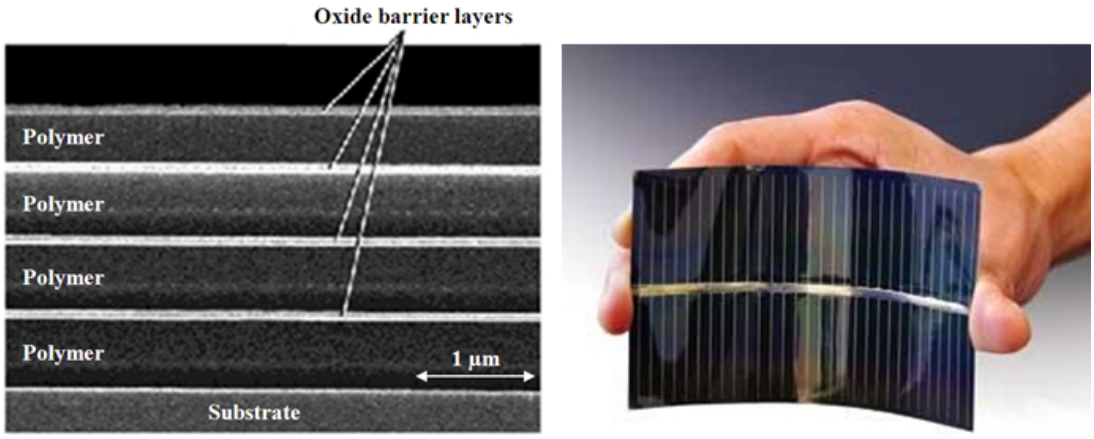

Figure 2.3: Typical multilayer barrier coating structure (left) and its application in thin film photovoltaic cells **[28]**

To get the picture of degree of uniformity required in the deposited films, one can examine the manufacturing of integrated circuits especially in VLSI (Very-Large-Scale Integration) circuits (Figure 2.4).

Small variations in film uniformity can have a large influence on the manufacturing yield: in this case film uniformity deviations of less than 5% are required at present. It is hardly surprising that the uniformity requirements are decreasing to a deviation limit of 1 to 2% in the near future **[29]**.

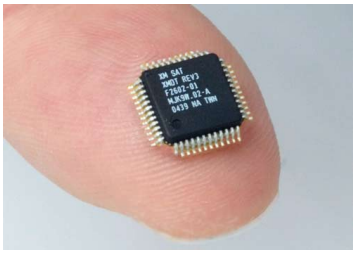

Figure 2.4: VLSI circuit dimensions (courtesy of R. Kaamran**,** *VLSI design*, Ryerson University)

2.3 *Thin liquid films over topographies – The process of planarization*

Typically in a device fabrication process sequence, there is a requirement to deposit films on a non-planar surface. In principle, this film should be uniformly distributed across all structural features of the substrate topography. This requirement is particularly stringent in those fabrication processes where the definition of very small geometries is required (e.g. a photolithographic pattern). Hence, the minimization of free surface disturbances caused by the presence of topographic features is an important target in several fields of research and industry.

In theory, this desired free surface planarization can be achieved by inducing "Marangoni surface tension gradients" **[30]** either by using a localized heater creating temperature variations at the film surface or by deliberately introducing surfactants into the flow, in other terms by introducing organic compounds that, lowering the surface tension of a liquid, allow easier spreading. The former approach, known as "thermo-capillary planarization" has been investigated for 2-D flows in the work of Gramlich et al. **[30]**: two profiles had been chosen to model physically realizable heaters (rectangular 'top-hat' and parabolic). It was found to be effective in reducing the height of the capillary ridge. In particular, with the optimized heaters, the variation in surface height is reduced by more than 50% compared to the original isothermal ridge. However due to the practical difficulties of integrating precision positioned local heating sources into the manufacturing process, with the associated additional energy consumption, the recent trend is to modify the topography of the non-functional (originally flat) regions of the substrate during the manufacturing process (*topographic planarization*, Figure 2.5, **[31]**): the process of planarization is vital for the development of multilevel structures in VLSI circuits where the principal target is to minimize interconnection resistance and conserve chip area (**[31]**, **[32]**).

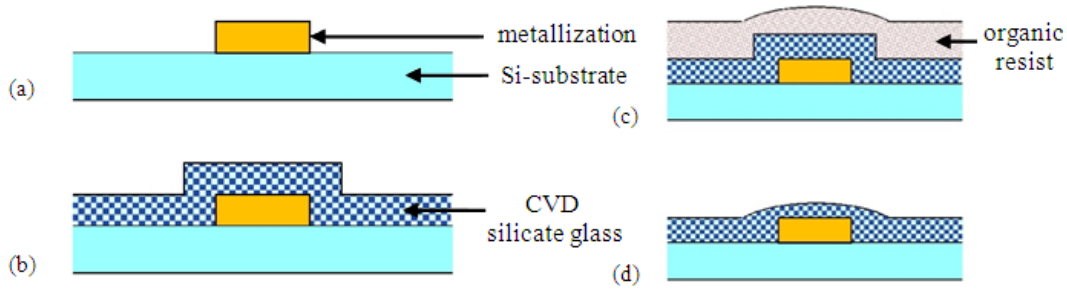

Figure 2.5: Outline of topographic planarization: an abrupt step (a) is coated with a layer of a low melting dielectric material (b) and subsequently an organic resin (c). The resin and dielectric are removed at the same time (technique known as "sacrificial etchback") and, eventually, a smooth surface is left behind (d) **[31]**

2.4 *Thin liquid films over topographies – Experimental techniques*

The simple idea of modifying the topography of the originally flat areas of the substrate at very little or no extra cost **[33]** in order to oppose the deviations from planarity caused by the functional topography is very difficult to achieve in practice. Indeed, controlling free surface disturbances for realistic 3-D flows is extremely challenging scientifically due to the complex free surface disturbances caused by distributed topography. Existing theoretical and experimental methods are incapable of meeting this challenge: currently only idealised cases over simple, discrete topographies have been considered **[30, 33, 38, 107]**.

Currently, experimental and theoretical methods have only been applied to simple cases of 3-D flows over regular or discrete topographies with film thicknesses typically much larger than the size of the topographies.

For example, the experimental study of Decré et Baret **[33]** in 2003 has investigated the free-surface shape of a thin liquid film (thickness ranging between 80 and 120μm) flowing over an inclined plate with topography (step, trench, rectangular and square topographies with depths of 10 and 20 μm, and lateral dimensions of the order of 1 to several mm): the report brings out the fact that even an outwardly simple case (3-D flow over a small square trench topography) shows a 'bow-wave' disturbance persisting downstream over distances far larger than the dimensions of the topographic feature (Figure 2.6, **[34]**).

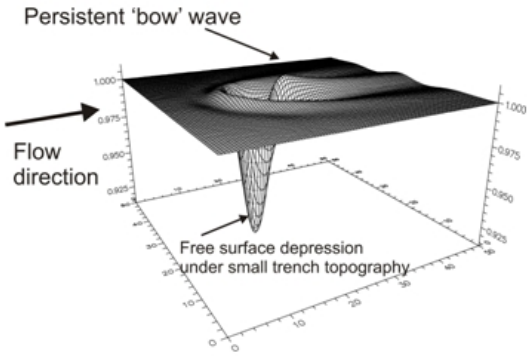

Figure 2.6: Predicted thin film flow over a single, square trench **[34]**

The experimental technique used phase-stepped interferometry to measure the phase of a wavefront by collecting intensity interferograms for (usually) 4 different stepped positions of the reference mirror in a Twyman-Green interferometer (Figure 2.7).

The Twyman-Green interferometer is a variant of the Michelson interferometer where the beam is expanded to cover the desired field of view and the fixed mirror (reference mirror) in the Michelson interferometer is rotatable.

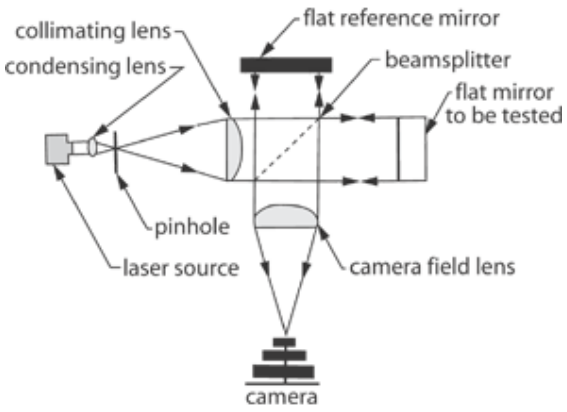

Figure 2.7: Twyman-Green interferometer (from Optical Society of America)

Now considering the time-averaged spatial intensity distribution $I(x,y)$ of an interferogram, this can be described using the equation **[35]**:

$$I(x,y) = I_o(x,y) \cdot \{1 + V(x,y)\cos[\Phi(x,y) - \Phi r(x,y)]\}$$

$I(x,y)$ can be written as a function of the phase of the wavefront $\Phi(x,y)$ where $I_o(x,y)$ represents the mean intensity, $V(x,y)$ the visibility (which depends on the coherence between the object and reference beams and their intensity ratio), and $\Phi r(x,y)$ the reference phase given by the position of the reference mirror in the interferometer.

Thus, any change in the surface topology manifests itself in the form of change in the phase term. This phase information can be used to obtain the object surface information as below (Karaalioglu C. and Skarlatos Y., **[36]**):

$$\Phi(x,y) = \frac{4\pi}{\lambda} \cdot d(x,y)$$

where $d(x,y)$ is the distance between the beam splitter and the object surface and hence is the desired surface form information (the value of refractive index in vacuum is assumed as 1).

The main problem is that one has to calculate the phase of the interferogram, $\Phi(x,y)$, as a result of phase shifted measurements. The phase stepped intensities can be obtained as a function of time by stepwise modulation of the position of the reference mirror in the interferometer, e.g. using a piezoelectric device.

The phase distribution of an interferogram can be determined as **[35]**:

$$\Phi(x,y) = arctan\left[\frac{(I_4 - I_2)}{(I_1 - I_3)}\right]$$

With I_1, I_2, I_3, I_4 are the intensity distribution of the interferogram with phase shifts of 0, π/2, π and 3π/2 radians, respectively and *arctan* is the inverse tangent function.

Usually in this kind of measurement, a solid-state detector array captures the interference fringes. By means of temporal phase shifting, a computer can control the phase difference between the two interfering beams and, at the same time, capture the detector output. By using a variety of algorithms it is possible to calculate the phase difference taking three or more measurements.
A problem that came out of the Decré & Baret paper **[33]** is that to spatially resolve the fringes required the field of view to be limited to about 1 mm, hence 100's of image patches had to be assembled and collected to measure over a field of a few 10's of mm, giving acquisition times of hours and generating considerable experimental difficulties in maintaining the stability of the flow. In addition, any vibration or thermal turbulence from the environment can modify the phase difference of the two beams in an unpredictable way. Consequently, environmental factors introduce large errors in the measurements. In addition reflections, from the solid substrate below the fluid film, generated parasitic fringes limiting the accuracy of the data obtained.

Another technique, to investigate the structure of a film flow over a topography, makes use of the fluorescence imaging method **[37]** as in the experimental study of Vlachogiannis and Bontozoglou **[38]**.
The idea is that by doping the fluid with a small concentration of dye (200-300 p.p.m. of sodium salt of fluorescein), the film fluoresces under ultraviolet illumination.
The fluorescence imaging method proposed has been used to investigate the structure of a gravity-driven film flow along a corrugated wall (in particular an inclined periodic wall with rectangular corrugations, Figure 2.8 **[38]**).

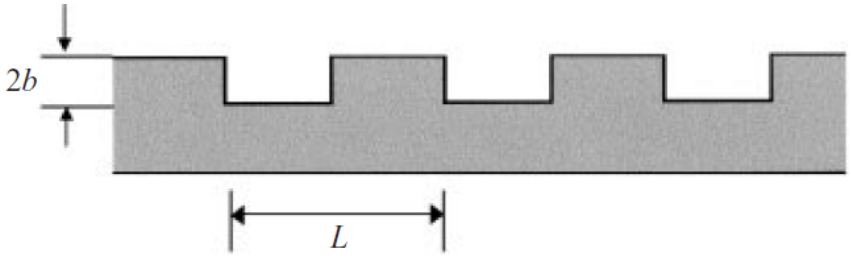

Figure 2.8: The characteristic dimensions of the corrugated wall (2b = 400 μm, L = 1.2 mm)

The fluorescence imaging technique is useful to follow the variation of film height in space and time of a film along an inclined wall (angles 1°- 8° inclusive) in order to confirm computational models of steady flow and to find out possible unsteady flow regimes. This work involves slightly inclined films over smaller disturbances.
The relation between fluorescence intensity $I(x,y,t)$ and local film thickness is linear if one considers thin films with thickness (h) less than 1.5 mm **[38]**:

$$I(x,y,t) = a(x,y)\cdot h(x,y,t) + b(x,y)$$

where $a(x,y)$ and $b(x,y)$ are two linear coefficients depending on the concentration of dye, the solution, the surface roughness of the wall plate and the UV source.
A variety of flows have been observed with this experimental method by modifying the inclination angles (1-8 degrees) over the range of Reynolds numbers ($10 < Re < 400$). The Reynolds number is a direct ratio of the density of fluid to the dynamic viscosity.

In particular, the Reynolds number is given by **[39]**:

$$Re = \frac{\rho V L}{\mu}$$

where ρ being the density of the fluid [kg/m^3], V is the velocity of the fluid [m/s], L the length or diameter of the fluid [m] and μ the dynamic viscosity [kg/ms].
In other words, the Reynolds number indicates whether the flow of a fluid is absolutely steady ("laminar flow", at low Reynolds numbers where viscous forces are dominant) or, unsteady (in turbulent flow, dominated by inertial forces, which tend to produce random vortices and other flow instabilities). The flow transition occurs as Re increases: a transition state whereby the flow exhibits neither completely laminar nor completely turbulent characteristics (unsteady waves).
Usually low Reynolds numbers are encountered in precision manufacturing applications using thin fluid films.

It has been seen that above a certain Reynolds number, depending on the inclination angle, film flows become linearly unstable. By observing the free surface, in the transverse direction, it is possible to see the formation of arrays of isolated depressions.

Furthermore, the experimental study of Vlachogiannis and Bontozoglou highlights that the critical Reynolds number is higher for a flow over an incline with rectangular corrugations than for a flat incline. In this context, the work of A. Wierschem and N. Aksel [**40**], based on linear stability analysis of a liquid film flowing down an inclined wavy plane, shows the topography has a stabilizing effect on the flow by increasing the critical value of the Reynolds number compared to the case of a gravity-driven film over a flat incline [**41**]. In particular they confirmed that, for gravity-driven films flowing down a profile (interface) inclined at an angle α with respect to the horizontal, the uniform film becomes unstable to long-wave disturbances, much larger than the depth of the film, when the calculated value for the Reynolds number is greater than the *critical value,* $Re_{crit} = \frac{5}{4}\cot\alpha$ (for a clean interface).

However, the main limitation of Vlachogiannis and Bontozoglou work is the limited resolution available of ~ 20 microns and that in the work reported the results refer to a single corrugation **[38]**.

The application results discussed in the preceding section confirm that when thin liquid film flows over a substrate containing topography, the disturbance caused to its free surface can persist over length scales far larger than the size of the topography themselves. For this reason, it is fundamentally important to support pre-existing theoretical studies and computer models by experimental techniques in order to measure thin films in different conditions (fluid thickness and topography).

The advantages and disadvantages of the two techniques discussed so far are summarised below.

Phase-stepped interferometry: measurement of the liquid film's free surface topography (Decré & Baret paper **[33]**):

i) Advantages: resolution (less than 10 nm); considerable variety of algorithms developed to calculate the phase difference;

ii) Disadvantages: parasitic fringes generated from reflections between top and bottom surface; limited to simple topographies; small field of view with acquisition times of hours; flow stability; need large numerical aperture of the imaging system to accommodate the slope of the fluid layer;

Fluorescence imaging method: measurement of film thickness (Vlachogiannis and Bontozoglou paper **[38]**):

i) Advantages: experimentally simple; thickness of film is large enough (1.5 mm) for most applications; works on complex topographies, can operate over a large field of view;

ii) Disadvantages: variable resolution (20 μm-100 μm);

2.5 *Summary*

The fabrication of a device (for example for structures like microchips) involves a sequence of processes needed to deposit films on a non-planar surface. It is a fundamental problem to uncover any process defects that could appear during the fabrication process. In particular, the industrial goal is often that of minimising the disturbances to the free-surface profile of the deposited film caused by the presence of topographic features in order to ensure accuracy, stability and repeatability of the process. The applications discussed in the preceding sections show that when thin liquid film flows over a substrate containing topography, the disturbance caused to its free surface can persist over length scales far larger than the size of the topography themselves.

Two experimental techniques (phase-stepped interferometry and fluorescence imaging method) used to investigate the structure of a film flow over a topography have been discussed with their relative advantages/disadvantages. The next chapter focuses its attention on some optical techniques which have been developed in order to get three-dimensional shape measurements by means of optical methods.

Chapter references

[25] MITTLER S. Surface Functionalization (December 2003). Available from http://www.physics.uwo.ca/~smittler/Silvia%20Mittler%20Surface%20Functionalisation.htm (Accessed: 27/05/2013).

[26] ECE4803: Electronic Packaging Substrate Fabrication. (2000). Available from http://www.ece.gatech.edu/research/labs/vc/packaging/lectures/lecture5.pdf (Accessed: 27/05/2013).

[27] BROWN WD (1999). Advanced Electronic Packaging. New York: IEEE Press. (ISBN: 0471466093).

[28] *SOLID STATE TECHNOLOGY Magazine* (October 2009), **52**(10).

[29] KERN W and SCHUEGRAF KK (2002). Deposition Technologies and Applications: Introduction and Overview. *In*: Seshan K, ed. Handbook of Thin-Film Deposition Processes and Techniques - Principles, Methods, Equipment and Applications, New Jersey: William Andrew, Noyes Publications.

[30] GRAMLICH CM, KALLIADASIS S, HOMSY GM, and MESSER C (2002). Optimal leveling over one-dimensional topography by Marangoni stresses. *Phys. Fluids* **14**(6), 1841-1850.

[31] GHANDHI SK (1994). VLSI Fabrication Principles, Silicon and Gallium Arsenide. Chichester: Wiley (ISBN: 9780471580058).

[32] BEADLE WE, TSAI JCC, and PLUMMER RD (1985). Quick Reference Manual for Silicon Integrated Circuit Technology. New York: John Wiley & Sons (ISBN: 0471815888).

[33] DECRÉ MMJ and BARET JC (2003). Gravity-driven flows of viscous liquids over two-dimensional topographies. *J. Fluid Mech.* **487**, 147-166.

[34] GASKELL PH, JIMACK PK, SELLIER M et al. (2004). Gravity-driven flow of continuous thin liquid films on non-porous substrates with topography. *J. Fluid Mech.* **509**, 253–280.

[35] GASVIK KJ (1996). Optical Metrology. New York: John Wiley & Sons (ISBN: 0471954748).

[36] KARAALIOGLU C and SKARLATOS Y (July 2010). Advances in Speckle Metrology and Related Techniques. Wiley-VCH (ISBN: 3527409572).

[37] LIU J, PAUL JD, and GOLLUP JP (1993). Measurements of the primary instabilities of film flow. *J. Fluid Mech.* **250**, 69-101.

[38] VLACHOGIANNIS M and BONTOZOGLOU V (2002). Experiments on laminar film flow along a periodic wall. *J. Fluid Mech.* **457**, 133-156.

[39] BIRD RB, STEWART WE, and LIGHTFOOT EN (2005). Transport Phenomena. New York: Wiley (ISBN: 0470115394).

[40] WIERSCHEM A and AKSEL N (2003). Instability of a liquid film flowing down an inclined wavy plane. *Physica D: Nonlinear Phenomena* **186**(3-4), 221-237.

[41] YIH CS (March 1963). Stability of Liquid Flow down an Inclined Plane. *Physics of Fluids* **6**(3), 321-334.

Chapter 3

Overview of three-dimensional shape measurement using optical methods

There are a remarkable number of optical techniques that have been developed in order to get 3D shape measurements in different applications. These methods can operate by acquiring (passive techniques such as photogrammetry) or by projecting (active techniques such as interferometry) electromagnetic energy into or from an object. A photodiode or camera records the transmitted or reflected energy. These techniques will be presented in the following sections.

3.1 *Optical techniques for 3D shape measurements*

The Time of Flight method uses the radar time-of-flight principle: the emitter unit generates a laser pulse and, during measurement, this object pulse is reflected back to a receiver. Now suitable electronics measure the roundtrip travel time of the returning signal. A typical resolution of this method is around a millimetre. A submillimeter resolution is achievable but only using high speed timing electronic circuitry and subpicosecond pulses (30 μm at a stand-off distance of 1m **[42]**).

The *Laser Scanning* technique is based on the active triangulation principle (Figure 3.1).

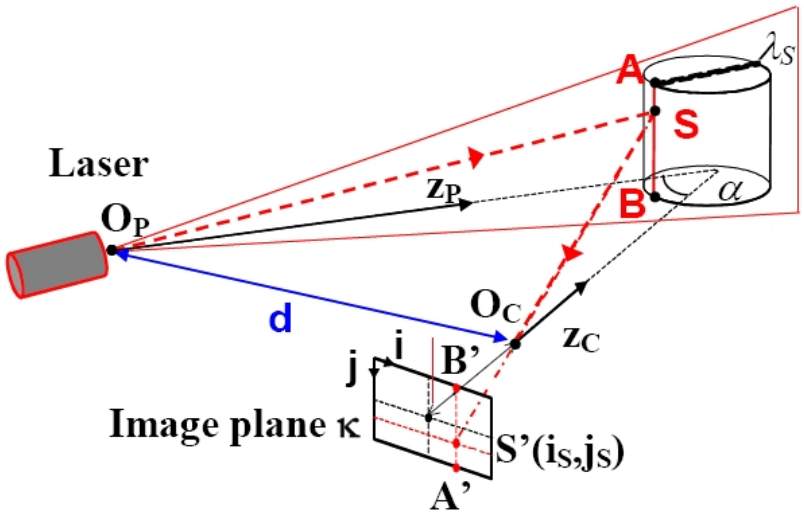

Figure 3.1: Schematics of the triangulation principle (from **"**State-of-The-Art and Applications of 3D Imaging Sensors in Industry, Cultural Heritage, Medicine, and Criminal Investigation" G. Sansoni, M. Trebeschi and F. Docchio, Sensors 2009).

The laser source generates a narrow beam, which reaches the object at point S. The back scattered light is imaged at point S' in image plane κ. The measurement of the location (i_S, j_S) of image point S' defines the line of sight S'O_c, and, by means of geometry, yields the position of S. The measurement of the surface is achieved by scanning the point S across the object surface.

The typical range of measurements is between 5 and 250 mm with a typical resolution of 250 μm **[43]**.

The point laser image can be recorded by a charged couple device (CCD) at high data acquisition rate. The main weakness is the achievable resolution, missing data in correspondence with occlusions and shadows and limited range and measurement volume.

The key of the *Moiré* method is two gratings: fringe range contours are obtained by illuminating the object with a light source passing through a grating, and viewing it with a laterally displaced CCD camera through a second grating known as a reference grating (Figure 3.2, **[44]**).

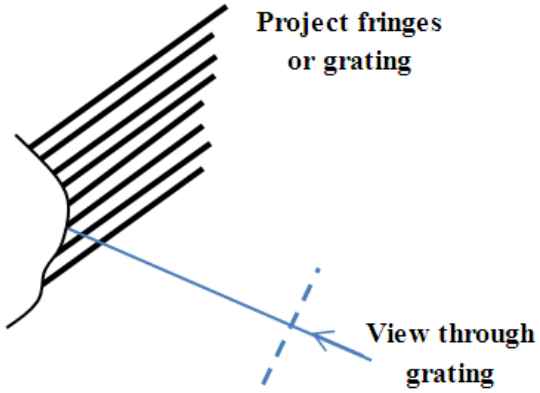

Figure 3.2: Projection moiré where fringes or a grating are projected onto a surface and viewed through a second grating (adapted from **[44])**

The resulting interference pattern shows equidistant contour lines and the information on surface depth is a complex and non-linear function of the system geometry.

This method is limited to the measurement of smooth surfaces because it can have phase discrimination problems when the surface does not exhibit smooth shape variations. In order to increase image acquisition speed and to analyse the fringe pattern by using phase shift methods, two or more multiple image moiré systems have been developed. For example, the *phase shifting moiré method* has a typical measurement range from 1 mm to 0.5 m with a resolution of typically one hundredth of a fringe (e.g. 25 μm, **[45]**).

The *Laser Speckle Pattern Sectioning* method is based on the relationship between optical wavelength and distance. If one considers that the optical field, in the analysis plane, can be seen as a two-dimensional "slice" of the object's three-dimensional Fourier transform then it is possible to get the other 2-D "slices" by changing the wavelength of the laser (Figure 3.3, **[46]**).

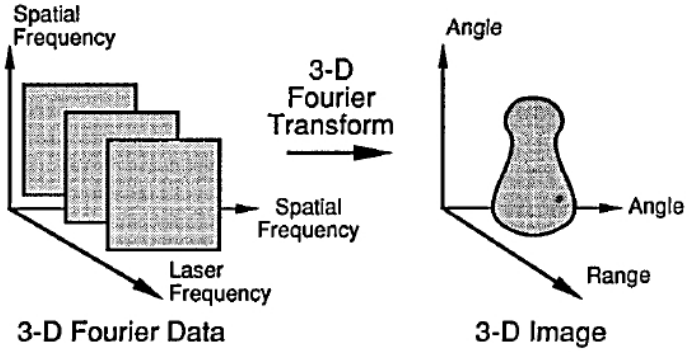

Figure 3.3: Relationship between collected data and the recovered image **[46]**

In recent years, the typical resolution is between 1 and 10 μm in the measurement range of 10 mm **[46]**. This technique shows a high flexibility of the measurement range but the main drawback is the time needed to get images with different wavelengths and the intrinsic requirement for a wavelength tunable laser.

As a passive technique, *photogrammetry*, makes measurements from photographs **[47]**. In particular, photogrammetry obtains reliable 3D models by establishing correspondences between features (photogrammetry markers) seen in multiple images. The elaboration of digital images follows a few steps: camera calibration and orientation, image point measurements, 3D point cloud generation, surface generation and texture mapping. Camera calibration is crucial in view of obtaining accurate models. Although it is a simple and inexpensive technique, it is limited to give information at well-defined targets (it needs some bright markers such as retro-reflective painted dots on the surface of a measured object).

The *Structured light* technique **[42]** shares the active triangulation approach mentioned above. However, instead of scanning the surface, 2-dimensional patterns of non-coherent light are projected and elaborated to obtain the range information for each viewed point simultaneously. A single pattern as well as multiple patterns can be projected (Figure 3.4). Object information is encoded into a deformed fringe pattern recorded by an image acquisition sensor: instead of adopting a reference grating (as in the Moiré method), the object shape is directly decoded from the deformed fringes recorded from the surface of a diffuse object following a suitable calibration process.

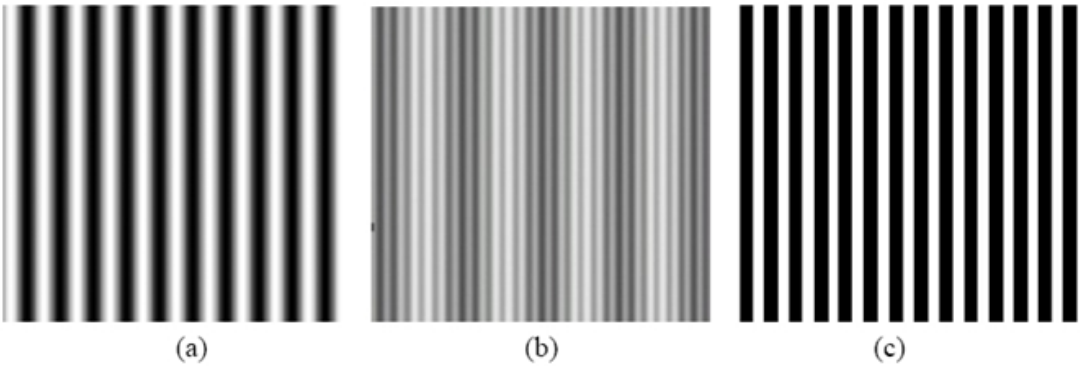

Figure 3.4: Some fringe projection schemes. (a) Sinusoidal fringes. (b) Superposition of two sinusoidal fringe patterns at different frequencies (c) Fringes of rectangular profile (from **"**State-of-The-Art and Applications of 3D Imaging Sensors in Industry, Cultural Heritage, Medicine, and Criminal Investigation" G. Sansoni, M. Trebeschi and F. Docchio, Sensors 2009).

The structured light method shows the following strengths: high data acquisition rate, good resolution via phase shifting, fringe density and direction change don't require moving parts if a computer controlled LCD/digital mirror device (DMD) is used; lateral and depth resolution of 1 and 0.1 μm **[42]**, respectively, can be achieved by using a microscope on small objects. The main weakness is missing data in correspondence with occlusions and shadows (this problem is inherent in all triangulation techniques).

Structured light can be obtained by the interference between two coherent waves or by adopting a grating in order to illuminate the object under observation.

Recently structured light has been generated by adopting an optoelectronic technique based on a fringe projection system including a saw-tooth phase grating **[48]**.

The idea is that, in analogy with a classical sinusoidal grating projection scheme where the fringes are straight lines (Figure 3.4a), structured light illumination can be generated by the interference of two fields diffracted by a saw-tooth phase grating (Figure 3.5, **[48]**).

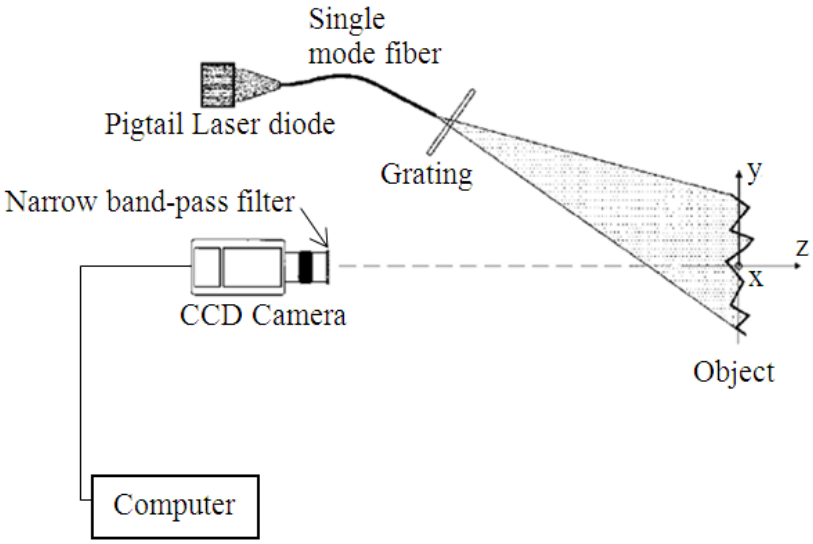

Figure 3.5: Layout of diffractive fringe projection interferometer (adapted from **[48])**

The light source is a red (670 nm) laser diode. The function of the grating is acting as beam splitter with light coming from the fibre output end: interference fringes appear in the area of overlapping of the two exiting beams. The system makes use of a CCD camera to record the fringe pattern generated on the test object. In addition a narrow band-pass filter, just in front of the CCD camera, is needed to allow operation in ambient light conditions. As mentioned before, the diffractive optical element (grating) has the task of behaving as a beam splitter so that most of the output power should be concentrated into the required diffraction orders. In order to have an idea about the saw-tooth phase grating performance it is useful to introduce the concept of *diffraction efficiency*, the ratio of the power of the diffraction order to the power of the incident beam. For example, in the paper of Ambrosini & Schirripa-Spagnolo **[48]**, the diffraction efficiency has been estimated as 0.4 for the 0^{th} order and 0.31 for the +1 order. The total diffraction efficiency (the ratio of the power exiting in the desired orders to that in the incident beam) is 0.71.

On the basis of the optical geometry of the projection unit (Figure 3.6, **[48]**) it is possible to prove that the fringe period $d\xi$ is given by:

$$d\xi = P(R + D)/R$$

with P being the period of the grating, R and D the distances of the system setup defined in Figure 3.6.

The meaning of the last equation is that fringe period can be controlled by changing the distance between light source and grating (*R* in Fig. 3.6).

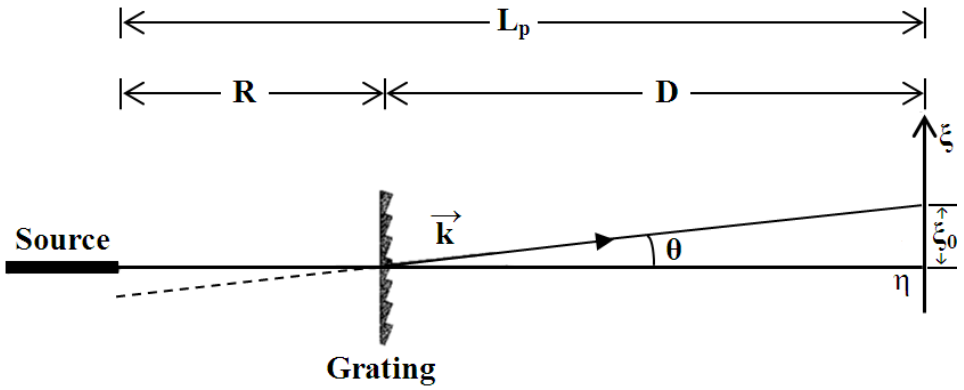

Figure 3.6: The optical geometry of projection unit (adapted from **[48])**

Quantitative evaluation of the surface shape can be obtained by the FFT phase measurement algorithm as in conventional sinusoidal grating projection techniques. This is an alternative to temporal phase shifting and can be applied provided the interference phase increases monotonically across the image.

Although this system is versatile (the fringe spacing on the test object (e.g. see Figure 3.7) can be modified for the case of the grating projection system by varying the distance between the fiber output end and the grating) and robust (quite insensitive to environmental instabilities), it shares some limitations similar to those with standard fringe projection: for high resolution one needs to analyze a small part of the test object and use a high resolution CCD camera. In addition, the problem with all triangulation approaches is that shadow may mean that the whole surface is not captured in a single measurement.

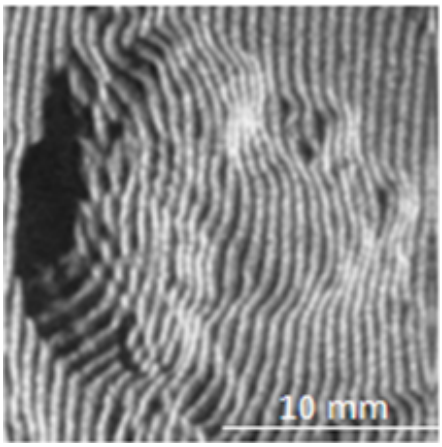

Figure 3.7: Particular of the fringe pattern projected on an ancient roman coin **[48]**

Laser induced fluorescence (LIF), a technique based on the photo-excitation of a fluorescent dye (principle shown in Figure 3.8), has gained popularity as a general-purpose visualization tool for numerous applications, in particular as a flow tracer (i.e. a dye used as a tracer to follow the flow of water or other liquids).

The principles of LIF are shown in Figure 3.8 (adapted from **[49]**).

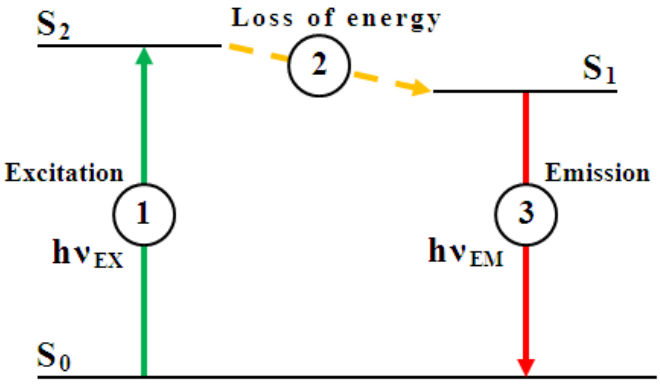

Figure 3.8: Fluorescence principle: (1) Excitation (photon of energy $h\nu_{EX}$ is supplied by an external source such as a laser and absorbed by the fluorophore, creating an excited electronic state, S_2);
(2) Excited-State Lifetime (during the excited state, typically 1 ns to 10 ns, the energy of S_2 is partially dissipated yielding a relaxed excited state (S_1) from which fluorescent emission originates. Not all the molecules initially excited by absorption (Stage 1) return to the ground state (S_0) by fluorescent emission;
(3) A photon of energy $h\nu_{EM}$ is emitted, returning the fluorophore to its ground state S_0. Due to energy dissipation during the excited-state lifetime, the energy of this photon is lower, and therefore of longer wavelength, than the excitation photon $h\nu_{EX}$. The difference in energy or wavelength represented by ($h\nu_{EX} - h\nu_{EM}$) is called the *Stokes shift*. The sensitivity of fluorescence techniques depends on this value because it allows emission photons to be detected **[49]**.

Fluorescent dyes can absorb light at one frequency and subsequently emit light at a different frequency. In some experiments, the dyes are excited by laser light with a frequency close to the excitation frequency of the dye. For example, Fluorescein (maximum excitation at 494 nm) is best excited by an Argon-Ion, Blue-Green laser with wavelengths 488 (blue) and 514 (green) nm. Once excited, Fluorescein maximum emission is at 520 nm. Because the fluoresced light is of a different frequency than the excitation light, the latter can be filtered out. In addition, only the dye that is exposed to the laser emits light, so specific planes within a flow field can

be seen. However, it has seen limited use as a quantitative tool. The reason for this derives primarily from the difficulty in separating variations in excitation illumination, surface reflectivity and optical distortion effects from fluorescent emission.

An evolution of this approach is the *emission reabsorption laser induced fluorescence* (ERLIF) technique **[50]**. The ERLIF technique was originally developed to measure oil film thickness in tribological systems, i.e. systems consisting of the surfaces of two components that are in moving contact with one another and their surroundings.

It is an optical technique that utilizes the reabsorption and emission of two fluorescent dyes to accurately measure film thickness while minimizing errors caused by variations in illumination intensity and surface reflectivity (typical problems of LIF technique). These problems can be minimized by observing the ratio of the two dye emissions **[50]**. The core of the technique relies on the use of a ratiometric approach for the purpose of suppressing excitation intensity information from the fluorescent emission.

The technique is limited in the range of film thickness that can be measured. The thickness range and resolution depends, among other factors, on the optical thickness of the system and the level of reabsorption that can be achieved.

This method demonstrates film thickness measurements in the 5-400 μm range with 1% accuracy **[50]**.

The technique known as *Ellipsometry* **[51]** has played a fundamental role as a method for thin film study, in parallel with the development of SiO_2 and other films used in highly-specialized fields of research (above all in the microelectronics industry). Ellipsometry is an optical technique for measuring the thickness and optical properties (refractive index) of thin films or layers of material simultaneously.

The method exploits Snell's law (Figure 3.9a). The basic idea is that by measuring the difference between the two reflections of a thin film sample, the thickness of the sample can be determined.

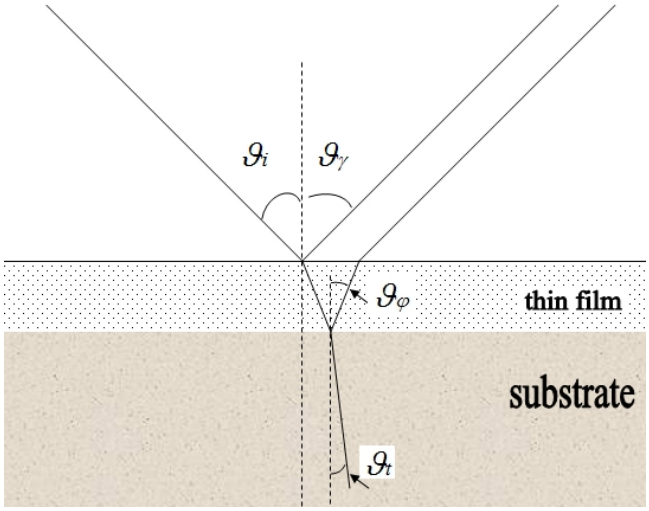

Figure 3.9a: Application of Snell's law. When a (thin film) sample with a different refractive index is illuminated with a beam of light incident at some arbitrary angle of incidence (ϑi) some will be reflected at angle ($\vartheta \gamma$), and some will pass through to the far side of the material at which point some will refract out of the sample (ϑt) and some ($\vartheta \varphi$) will reflect.

For purposes of ellipsometry, it is useful to discuss the wave's electric field behaviour in space and time, also known as polarization (Figure 3.9b).

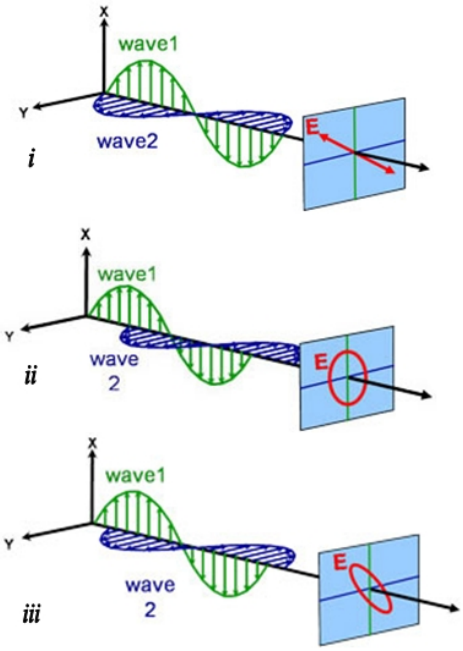

Figure 3.9b: Polarization states**:** linear (*i*), circular (*ii*), elliptical (*iii)*

The method also examines the state of polarisation of the reflected waves. When two orthogonally polarised light waves are in-phase, the resulting light will be linearly polarized (Figure 3.9b, *i*). The relative amplitudes determine the resulting orientation. If the orthogonal waves are $\pi/2$ out-of-phase and equal in amplitude, the resultant light is circularly polarized (Figure 3.9b, *ii*).

The most common polarization is *elliptical*, one that combines orthogonal waves of arbitrary amplitude and phase (Figure 3.9b, *iii*). Reflected light also undergoes a change in polarization. This change is used to calculate the refractive index.
The basic principle is shown in Figure 3.10.

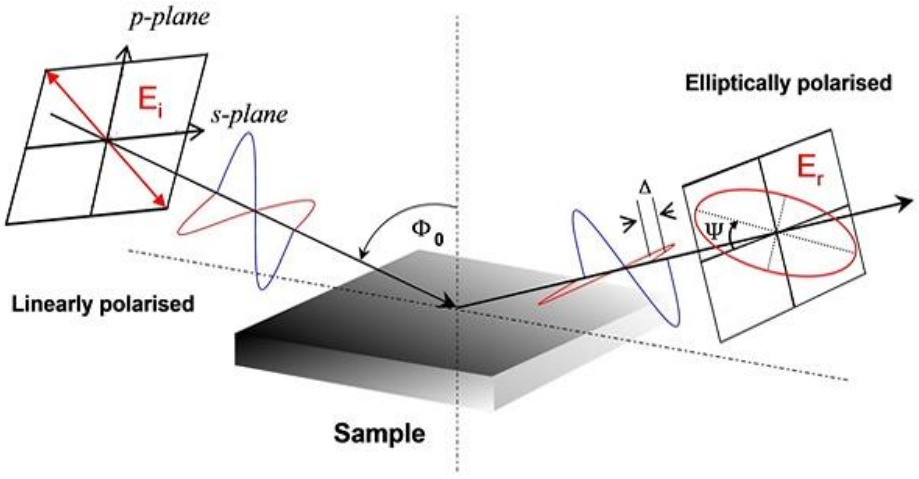

Figure 3.10: Ellipsometry, basic principle (adapted from **[52]**)

Ellipsometry measures the change in polarization of light reflected from the surface of a sample. The complex refractive index **[51]** of a material can be written as:

$$N(\lambda) = n(\lambda) + i \cdot k(\lambda)$$

Then this technique uses the change in polarization of light (after reflection) to determine real part (refractive index, $n(\lambda)$, which controls the angle of refraction) and imaginary part (extinction coefficient, $k(\lambda)$, which determines the absorption of light as it propagates through the medium) of the complex refractive index (with λ the wavelength of the electromagnetic radiation).

The concept is shown in Figure 3.11 **[51]**: light travels from air into an absorbing layer (Film 1) and then into a transparent layer (Film 2). The phase velocity and wavelength change in each material as a function of the index of refraction (Film 1: n=4, Film 2: n=2 in Figure 3.11). The amplitude of the wave decreases as it propagates through the absorbing layer, Film 1.

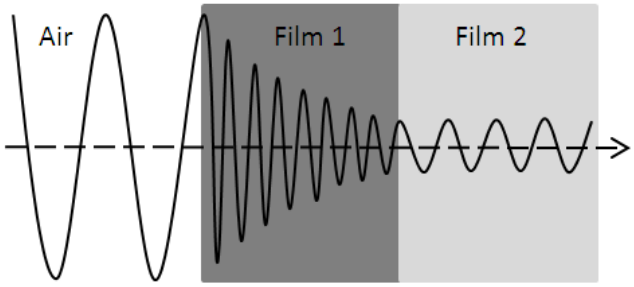

Figure 3.11: The concept of extinction coefficient (adapted from **[51]**)

Ellipsometers measure the shape of this polarization ellipse, hence the name ellipsometry. Usually a *p*-*s* coordinate system is used in order to describe the ellipse of polarization. In this system the *s*-direction, polarization direction perpendicular, is taken to be perpendicular to the direction of propagation and parallel to the sample surface. The *p*-direction is perpendicular to the direction of propagation and contained in the plane of incidence.

The polarization change is represented as an amplitude ratio, Ψ, and the phase difference, Δ. Ellipsometers measure the ratio ($\tan \Psi$) and the phase difference ($\cos \Delta$) of the reflected p- and s-components.

These two parameters are directly connected to the physical properties of the reflecting surface such as the optical constants, i.e. the refractive index *n* and extinction coefficient *k*, and the thickness of the material **[51]**.

In addition, the degree of ellipticity of the reflected light is determined by the sample properties (for example, refractive index of the thin film), and its thickness.

This approach, in principle, can be applied to the study of multi-layered structures in order to calculate the thickness and optical properties of various films (Figure 3.12, **[53]**).

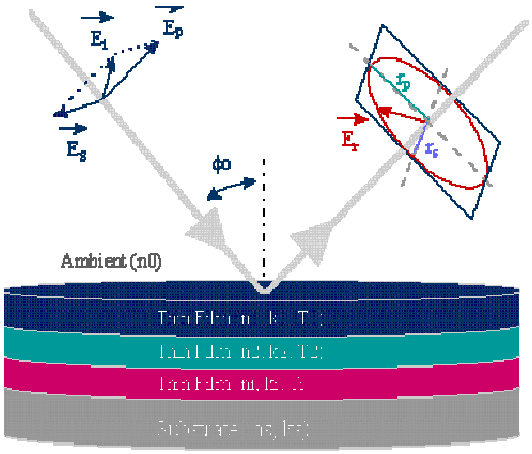

Figure 3.12: Application of Ellipsometry on multi-layered structures **[53]**

The operative realization of an ellipsometer needs some tools for collecting data: polarization generator, polarization analyser, and detector. In particular, polarization generator and analyser are made of optical components that change the polarization state: polarizers, compensators, and phase modulators. Typical ellipsometer configurations include rotating analyser (RAE), rotating polarizer (RPE), rotating compensator (RCE), and phase modulation (PME). In Figure 3.13 is shown the configuration with rotating analyser (RAE).

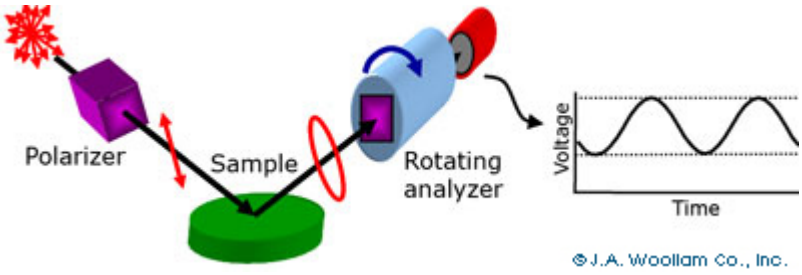

Figure 3.13: Schematics of Ellipsometer in RAE configuration (from J.A. Woollam Co., Inc.)

A light source (commonly a 632.8 nm He/Ne laser) generates unpolarized light which passes through a polarizer. Thanks to the polarizer, only light of a preferred electric field orientation can pass.

The polarizer axis is oriented between the p- and s- planes, such that both arrive at the sample surface. The linearly polarized light, when reflected from the sample surface, changes its state to elliptically polarized, and travels through a continuously rotating polarizer (Fig. 3.13). The detector converts the light intensity to an electrical signal in order to determine the reflected polarization.

This result is compared to the known input polarization to determine the polarization change caused by the reflection: in other words, the measurement of Ψ and Δ.

As a general rule, this technique is often used to measure film thickness: typically for films whose thickness ranges from sub-nanometre to a few microns.

The measurements from an ellipsometer give the product of refractive index and film thickness (this product is the optical path length) but if the index is not known or difficult to calculate accurately, thickness errors will result.

In addition, the sample being examined has to satisfy certain physical properties: it needs to have a sample composed of a small number of well-defined layers and these layers must be optically homogeneous, have identical molecular structure in all directions, and reflect significant amounts of light.

Thickness measurements need that a fraction of the light travels through the whole film and return to the surface. If this sample absorbs light, thickness measurements are limited to thin semi-opaque layers. For example, films of organic materials show a strong absorption for UV-radiation and the infrared region of the electromagnetic spectrum (IR), but are transparent to mid-visible wavelengths.

An extremely drastic case is the family of metals, which strongly absorb at all wavelengths. In this case, the maximum layer for thickness determination is about 100 nm **[54]**.

Thin film characterization generally also needs a model of the optical response of the thin film and substrate to be built, which is then compared with the experimental data, in the form of the ellipsometric parameters (tan Ψ and cos Δ).

In traditional temporal "phase shifting" interferometry, data is acquired over hundreds of milliseconds, long enough to make the results susceptible to vibration and air turbulence.

A better approach for reducing the effects of vibration is to capture all four phase-shifted frames on a single CCD camera and in a single frame of information: this idea is the basic principle of *4D – technology* systems **[55]**. For example, to analyze transient phase distributions, the system in Figure 3.14a can be used where the object and reference beams are arranged to have orthogonal polarizations and then the orientation of a birefringent material in front of the detector (CCD camera) varies the phase shift between the two beams. By using a set of 4 orientations of the birefringent material, the four phase shifted intensities can be obtained over a 2x2

group of pixels, defining a single ‘superpixel’ at which a phase measurement can be obtained. This approach has the advantage that a single acquired image can be used to determine the interferometer phase.
In either case of temporal phase shifting (see Decré & Baret paper, chapter 2) or using a birefringent mask, the phase distribution of an interferogram can be determined as **[35]**:

$$\Phi(x,y) = arctan\left[\frac{(I_4 - I_2)}{(I_1 - I_3)}\right]$$

with I_1, I_2, I_3, I_4 are the intensity distribution of the interferogram with phase shifted of 0, $\pi/2$, π and $3\pi/2$ radians, respectively and *arctan* is the inverse tangent function.

The heart of these systems is the dynamic interferometer: this incorporates a polarization based Twyman-Green configuration with a 2-D grating at the exit pupil and a phase mask in the imaging path. This dynamic interferometer with a holographic optical element produces four phase-shifted interferograms imaged simultaneously on a single detector (Figure 3.14a).

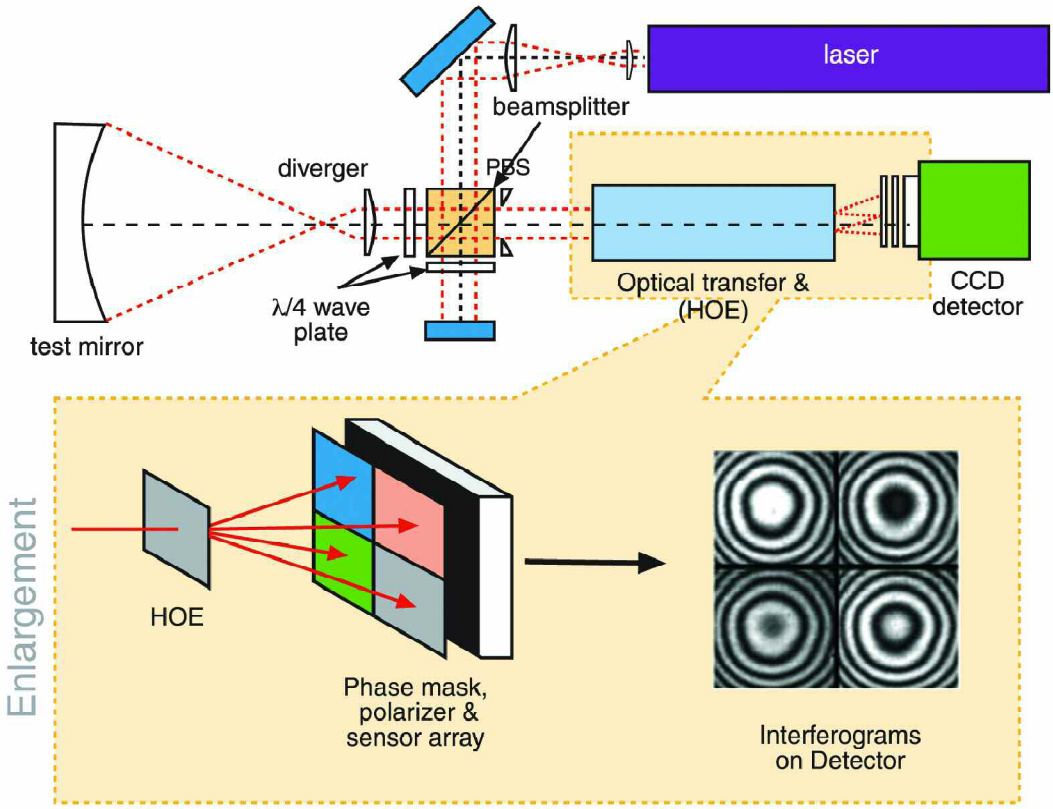

Figure 3.14a: In this arrangement, a Twyman-Green interferometer is used where the reference and test beams have orthogonal polarization. After the two beams are combined they pass through a holographic element that splits the beam into four separate beams resulting in four interferograms. These four beams pass through a birefringent mask that is placed just in front of a CCD camera. The four segments of the birefringent mask introduce phase shifts between the test and reference beams of 0, 90, 180, and 270 degrees. A polarizer with its transmission axis at 45 degrees to the direction of the polarization of the test and reference beams is placed after the phase masks just before the CCD array. Thus, all four phase shifted interferograms are detected in a single shot on a single detector array **[55]**

In particular, the grating/mask (Figure 3.14b, **[55]**) combination produces four phase-shifted interferograms imaged in parallel on a single high-resolution detector. A single frame of intensity data therefore provides the four frames necessary to compute phase. In essence, the phase shifts occur spatially, not temporally.

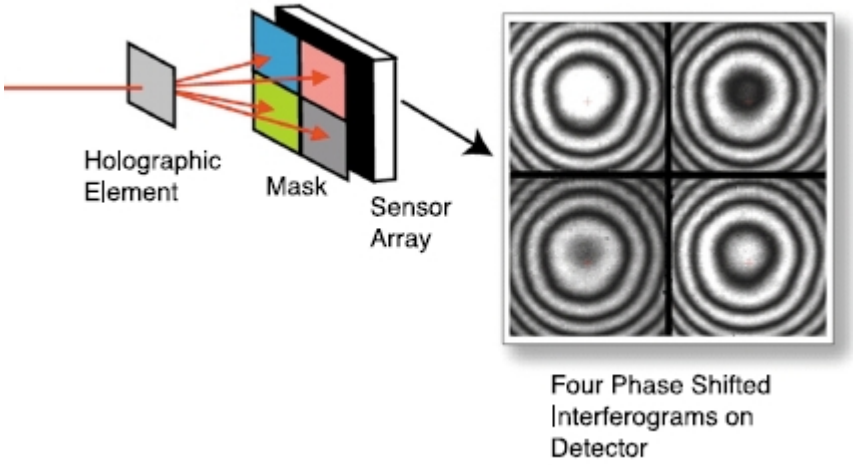

Fig. 3.14b: Four phase shifted interferograms on detector are obtained thanks to the grating/mask

Commercially available mega-pixel cameras can acquire high spatial sampling data arrays in as little as 30 μs, 5000 times faster than conventional phase shifting interferometers (from 4D Technology Corp). For example, a commercial product as PhaseCam 7000 (4D Technology Corp.) enables the measurement of substrates as thin as 300 μm (RMS Precision < 0.002 wave) with data acquisition time less than 30 μs. Data can be acquired to allow the generation of phase movies to study the dynamic motion of surfaces.

To summarize, the advantages and disadvantages of the techniques discussed so far are shown in the following table:

TECHNIQUE	STRENGTH	WEAKNESS
Time of Flight	Medium to large measurement range	Cost Accuracy is inferior to triangulation methods
Laser Scanning	High data acquisition rate Performance generally independent of ambient light	Missing data in correspondence with occlusions and shadows Operates on solid surfaces Poor resolution
Moirè	Simple Low cost	Limited to the measurement of smooth surfaces
Laser Speckle Pattern Sectioning	High flexibility of the measurement range	Slow Intrinsic requirement for a wavelength tunable laser
Photogrammetry	Simple Inexpensive	Limited to measurements at a few well-defined targets
Structured light	High data acquisition rate Good resolution via phase shifting	Missing data in correspondence with occlusions and shadows Operates on solid surfaces
Interferometry (by grating projection system)	Versatile Robust	Slow High resolution CCD camera
Laser induced fluorescence	Simple	Variable resolution and resolution is insufficient for some thin film applications
Ellipsometry	High resolution	Limited to optically homogeneous samples
4-D Technology	High data acquisition rate	Cost Potential difficulty due to parasitic fringes from substrate and exterior film

Table 3.1 Summary of the optical techniques analysed

3.2 *Summary*

Several techniques have been developed in order to measure the three-dimensional shape of the object under test and/or its thickness or the wavefront reflected from it. These techniques are based on the acquisition (passive methods) or projection (active methods) of electromagnetic energy into or from an object. Not all these methods can be applied to thin liquid film metrology. For instance, *Laser Scanning* operates on solid surfaces. In other cases, the measurement has to be limited to smooth surfaces (*Moirè* technique) or optically homogenous samples (*Ellipsometry*). Hence, a comparative table has been developed in order to highlight advantages and disadvantages of the techniques analyzed in this chapter. Two methods (*Fluorescence Intensity and Classical Interferometry*) are potentially suitable for metrology of thin fluid films despite some intrinsic limitations (variable resolution and small field of view, respectively).

The next chapter will focus attention on how to overcome these limitations by means of a suitable fluorophore solution combined with laser based fringe projection.

Chapter references

[42] CHEN F, BROWN GM, and SONG M (2000). Overview of three-dimensional shape measurement using optical methods. *Optical Engineering* **39**(1), 10-22.

[43] YOSHIZAWA T (2009). Handbook of Optical Metrology: Principles and Applications. Boca Raton, Fla: CRC Press (ISBN: 9781420019513).

[44] CREATH K and WYANT JC (1992). Moiré and fringe projection techniques. *In*: MALACARA D, ed. Optical Shop Testing, New York: John Wiley and Sons.

[45] WANG Y and HASSELL P (October 1997). Measurement of Thermally Induced Warpage of BGA Packages/Substrates Using Phase-Stepping Shadow Moiré. *In*: Electronic Packaging Technology Conference. Atlanta: Electronic Packaging Services, Ltd. Co., 283-289.

[46] MARRON JC and SCHULZ TJ (1992). 3-Dimensional, Fine-Resolution Imaging Using Laser Frequency Diversity. *Optics Letters* **17**, 285-287.

[47] GEODETIC SYSTEMS, INC. The Basics of Photogrammetry. Available from http://www.geodetic.com/v-stars/what-is-photogrammetry.aspx (Accessed: 27/05/2013).

[48] SCHIRRIPA-SPAGNOLO G and AMBROSINI D (2001). Surface contouring by diffractive optical element-based fringe projection. *Meas. Sci. Technol.* **12** (N6-N8).

[49] HAUGLAND RP (1999). Handbook of Fluorescent Probes and Research Chemicals. Eugene, OR: Molecular Probes Inc. (ISBN: 9780965224031).

[50] HIDROVO CH and HART DP (2001). Emission reabsorption laser induced fluorescence (ERLIF) film thickness measurement. *Meas. Sci. Technol.* **12**, 467-477.

[51] TOMPKINS HG and IRENE EA (2005). Handbook of Ellipsometry. Norwich, NY: William Andrews Publications (ISBN: 0815514999).

[52] Surface and Interface Physics: Ellipsometry. Available from http://www.tcd.ie/Physics/Surfaces/ellipsometry2.php (Accessed: 27/05/2013).

[53] WOOLLAM JA (2000). Ellipsometry, Variable Angle Spectroscopic. *In:* Encyclopedia of Electrical and Electronics Engineering. New York: John Wiley & Sons (ISBN: 9780471358959).

[54] WOOLLAM JA CO., INC. Spectroscopic Ellipsometry Tutorial. Available from http://www.jawoollam.com/tutorial_1.html (Accessed: 27/05/2013).

[55] WYANT JC (August 2005). Going Through A Phase. *SPIE OE Magazine*.

Part II

Materials and Methods

Chapter 4

New way to measure thin film topography

This chapter presents a new approach to measure thin (liquid) film topography. Current techniques show significant limitations as described in Section 4.1. The proposed approach makes use of suitable dyes for measuring the surface topography of thin fluid films by fluorescence based fringe projection.
Subsequent sections describe the main stages adopted in order to characterize the new method on the basis of theoretical (Beer-Lambert Law) and practical approach (flow cell application). Moreover, the conditions by which the fluorescence emission is sufficient for full field imaging in fringe projection are discussed. The chapter finishes with the identification of a dye with sufficiently strong absorption but without significant loss of emission intensity with increasing dye concentration.

4.1 *Limitations of the previous methods*

The techniques analyzed so far for metrology of thin liquid films give either (or both) the profile of the exterior surface and information on the thickness of the film. The main drawbacks of the existing methodologies are:

- *Fluorescence Intensity*: it is simple to apply but as an intensity measurement the resolution is typically >10 microns in full field applications **[38]**.

- *Classical Interferometry*: it requires high numerical aperture optics to capture reflections from surfaces at various slopes, hence gives a small field of view, usually < 1 mm **[33]**.

4.2 *Fluorescence based fringe projection*

The proposed approach will adopt a fringe projection system (main laser input power of 200 mW at 532 nm) with a high concentration of fluorophore dissolved in the fluid such that fluorescence emission is derived from the first few microns of the film.

The basic idea is to remove the dependency on high numerical aperture imaging by means of fluorescent dyes in order to overcome small field of view. Indeed, in conditions of excitation, the emitted fluorescence is approximately uniform in all directions **[56]**. In the same time, it is possible to make use of a fringe projection system with sufficient phase resolution and fringe spacing in order to potentially achieve a resolution of a few microns.

As discussed in Decré & Baret paper **[33]** classical interferometry on thin (liquid) films can produce multiple interference terms (parasitic fringes) due to reflections from the top and bottom of the fluid film. Hence, reflections from the bottom of the film can be eliminated by the fluorophore added to the fluid.

Therefore it is expected that fluorescence based fringe projection should provide ~micron resolution topography data over substantial fields of view in thin film applications.

The method developed in this thesis relies on calculation of an interference phase term and therefore also to the modulation depth of the fringes created.

In light of these considerations, the central aim of this chapter is to give an insight into the characterisation of candidate fluorescent dyes in terms of absorption, related to the depth of penetration of the incident light into the dye and their fluorescence emission spectra.

In this chapter the attention will focus on three different fluorescent dyes selected as their absorption spectra match the frequency of the laser source available (532 nm) and also the spectral sensitivity range of the CCD device. Three chemical species have been identified **[57]**: Rhodamine B Chloride (solvents: water and ethanol), DCM special (solvents: methanol) and Sulforhodamine 640 (solvents: water, methanol, ethanol).

4.3 *Fluorescence: emission and depth of penetration*

Characterisation of fluorescent dyes will be carried out based on two criteria:

- Depth of penetration: the next paragraph will analyze the candidate fluorescent dyes to assess their compatibility with the measurement of thin film surface profile by fluorescence based fringe projection.

- Fluorescence intensity: the candidate fluorescent dyes have been investigated in order to match the maximum peak of fluorescence emission with the lowest depth of penetration of the light into the fluid as needed for the investigation of thin fluid films.

4.3.1 *Depth of penetration – Theoretical Analysis via Beer-Lambert Law*

Beer's law states that the optical absorbance of a fluorophore in a transparent solvent varies linearly with both the concentration and the sample cell path length **[58]**. For liquids, the sample is held in an optically flat, transparent container called a cuvette. Absorbance (A_λ) is calculated from the ratio of the light intensity that is incident on the sample (I_0) to the intensity passing through the sample (I), **[59]**:

$$A_\lambda = \log\left(I_0 / I\right) \qquad \text{(Eq. 4.1)}$$

The absorbance of a sample depends on the molar concentration (c, [mol L^{-1}]), length of solution the light passes through (L, [cm]), and molar absorptivity (ε, [L mol^{-1} cm^{-1}]) for the dissolved substance (*Beer's law*):

$$A_\lambda = \varepsilon\, c\, L \qquad \text{(Eq. 4.2)}$$

Therefore the value of molar absorptivity, ε, can give an indication of the depth of penetration of the incident light.

Experimental measurements are usually made in terms of transmittance (T), which is defined as: T = I / Io (Figure 4.1). Transmittance is often quoted in terms of a percentage, *% Transmittance*, %T = 100 T.

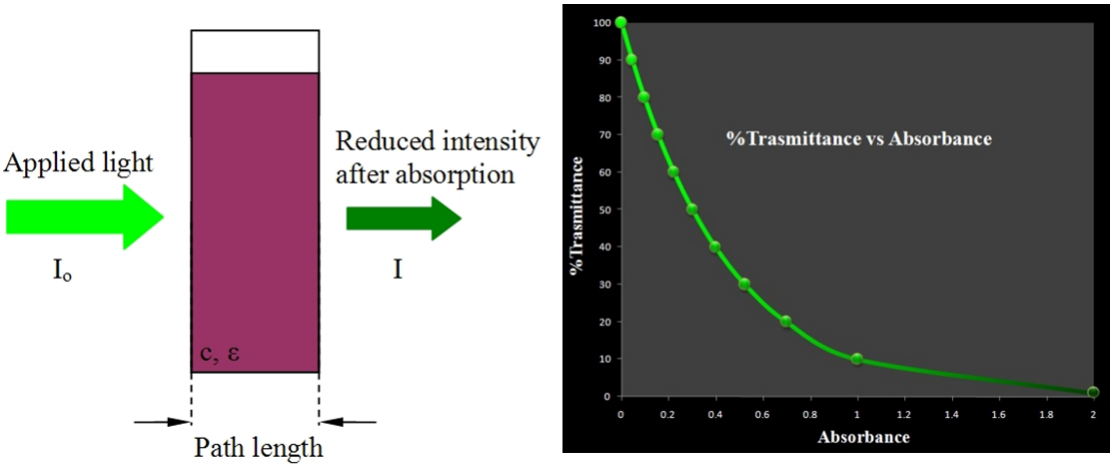

Figure 4.1: Schematics to illustrate the Beer-Lambert law. The diagram (left) shows a beam of monochromatic radiation of intensity I_o, directed at a sample solution of concentration, c and molar absorptivity, ε. Absorption takes place and the beam of radiation leaving the sample, of intensity I, is attenuated.
The Law states that the fraction of the light absorbed by each layer of solution is the same (right).

On reading the two forms of the Beer-Lambert law (Eq. 4.1, 4.2) it should be clear that there is a linear relationship between absorbance and concentration at a fixed path length and, at the same time, between absorbance and path length at a fixed concentration. Therefore, the molar absorptivity (ε) can be used to make predictions of penetration depth for the laser light passing through the dye dissolved in a solution.

All these considerations lead to a comparison of the candidate fluorescent dyes in terms of molar absorptivity for a specific laser input source (532 nm, in this case). Indeed, it should be noted that chemical species showing a higher molar absorptivity provide the best performance in terms of depth penetration for this application where it is desirable for the fluorescence emission to derive from the top layer of the thin fluid film (according to the Eq. 4.2 the higher the molar absorptivity the shortest the length of solution the light passes through).

For example, the following figures (Fig. 4.2 & 4.3) illustrate the case of Rhodamine B Chloride dissolved in Ethanol compared with two other candidate fluorescent dyes

(Sulforhodamine 640 and DCM special). It shows, for the same laser input source (532 nm), a higher molar absorptivity and therefore a shorter depth of penetration.

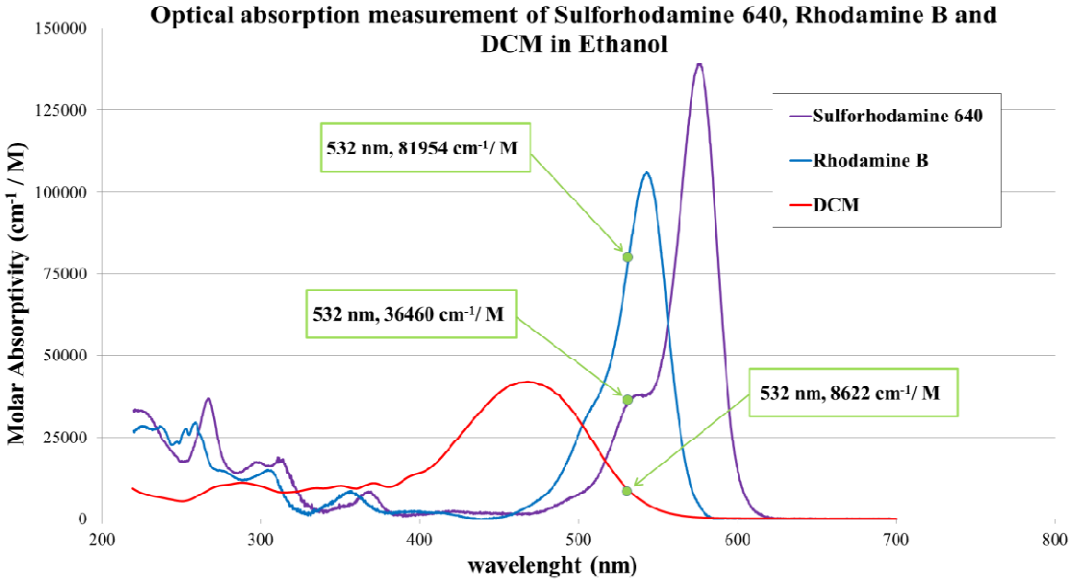

Fig. 4.2: Comparison between the absorption of three candidate fluorescent dyes. For the same incident wavelength, 532nm (indicated in green colour), Rhodamine B (Chloride) dye shows a larger molar absorptivity compared to Sulforhodamine 640 and DCM (original raw data from **[60, 61]**).

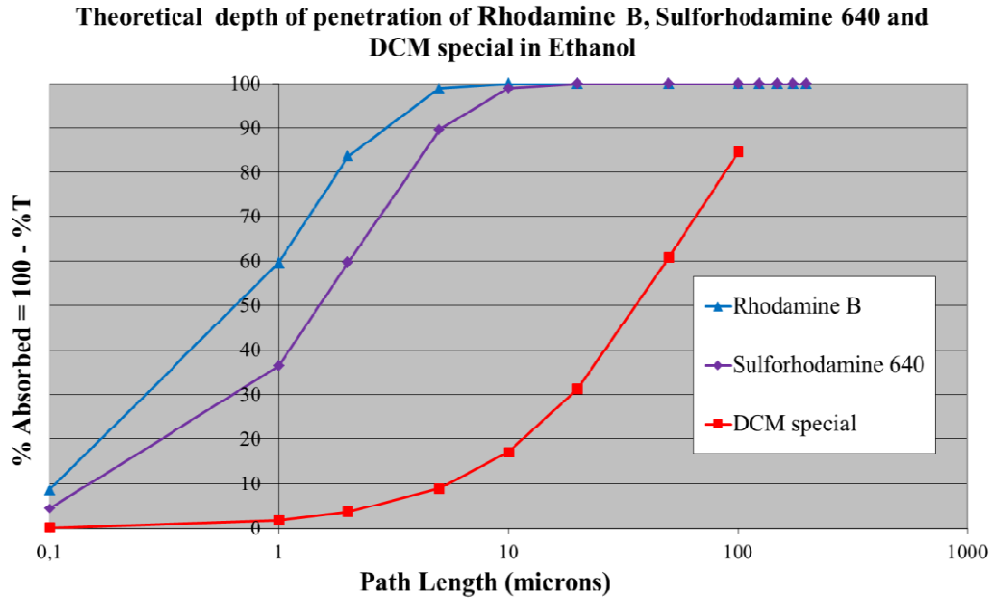

Fig. 4.3: The plot above indicates that, for the same expected absorbed light (as a percentage), three different candidate dyes show different path lengths (depth of penetration). The theoretical calculations are based on molar absorptivity values for Rhodamine B (Chloride), Sulforhodamine 640 and DCM special dissolved in ethanol and with saturated concentration levels of 48 mM, 54 mM and 10 mM, respectively.

The data in Figure 4.3 provide an initial indication that dye / solvent combinations are available to achieve the necessary absorption within the top few microns of a thin fluid film. However, this is based on a theoretical analysis and in practise there are frequently deviations from the direct proportionality of the Beer-Lambert law. The law is not obeyed at high concentrations (> 0.01 M): transmittance inherently decreases logarithmically and linearity is observed to break down at higher concentrations due to sample saturation **[62]**.

Causes of nonlinearity can be due to the following factors **[63]**:

- electrostatic interactions between molecules can produce deviations in absorptivity coefficients at high concentrations;
- presence of particulates in the sample can cause scattering of light;
- change in refractive index (the molar absorptivity, ε changes due to a variation of the incident light);

Some of these effects can be compensated. For example, losses due to scattering of light can be minimized by using high quality glass cuvettes. Others, such as the linearity breakdown at high concentrations, need a deeper investigation. Therefore some experiments (with a clear glass flow cell) have been carried out to examine the behaviour of the candidate fluorescent dyes when the solute concentration is near saturation.

4.3.2 *Depth of penetration – Experimental approach: flow cell*

A practical experimental setup can be arranged as in the following diagram (Fig. 4.4), which shows a clear quartz glass flow cell filled up with a solution made of a fluorescent dye (one dye, at any time) and a solvent (water, methanol or ethanol).

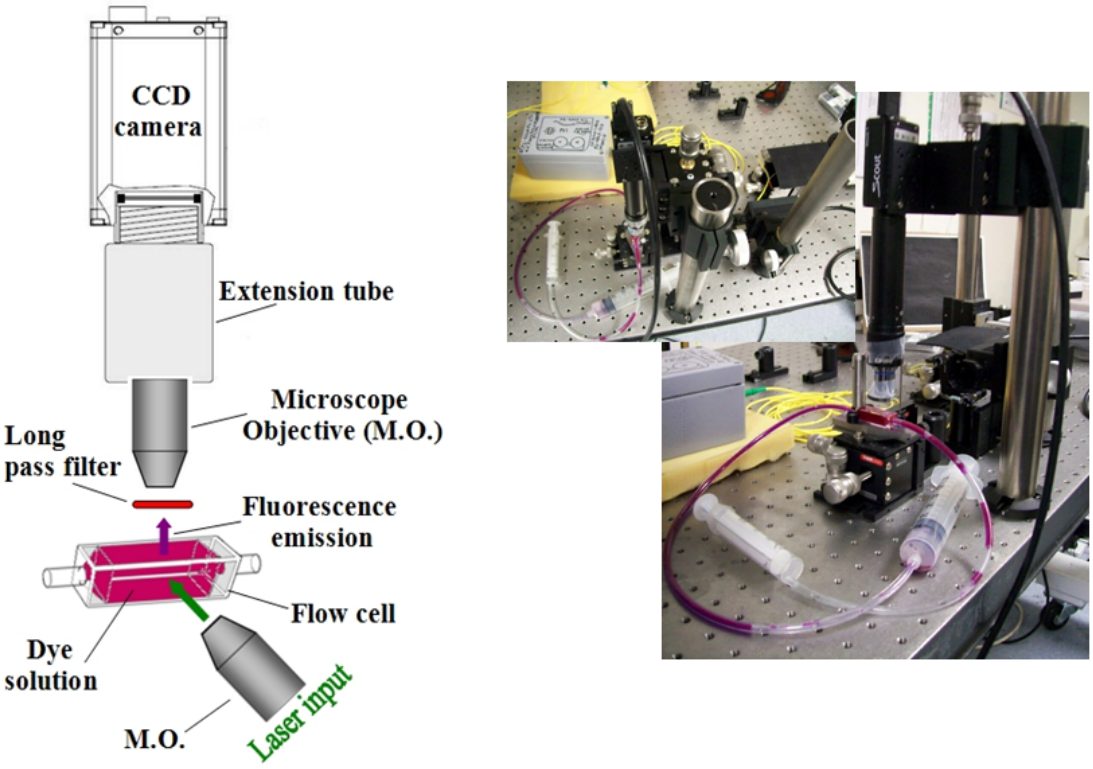

Fig. 4.4: (left) Schematic diagram of the system adopted to estimate the depth penetration into the fluorescent solution when the dye concentration is near the saturation level. Because the flow cell is made of clear glass the laser source (1mW at 532 nm) can stimulate the fluorescent solution from one side of the flow cell (marked with a green arrow). The fluorescence emission can be collected and analyzed by means of a CCD camera and suitable imaging optics (extension tube + microscope objective). Because the wavelength of the laser source (532 nm) is lower than the cut-off wavelength of the long pass filter (568 nm), only the fluorescence light passes through. (Right) Experimental setup.

The above system provides a variable magnification ranging between 9× and 21× allowing to select the portion of the image where the fluorescence emission is generated. The scale of the image has been calibrated by means of a resolution test pattern (USAF 1951 Chart, **[64]**) according to the CCD camera pixel size (6.45 × 6.45 μm).

The image was focussed using a 3-axis linear translation stage with micrometric resolution (right of Figure 4.4).

Therefore, the behaviour of the fluorophore solution can be characterized considering the results of the theoretical model (Beer-Lambert law) with the corrections gained with the experimental evaluation.

Indeed, if one shines light (532 nm wavelength, in our case) into an absorbing medium the intensity of the stimulated light is attenuated exponentially with the path length according to the Beer-Lambert law (Eq. 4.2).

On the basis of the molar absorptivity values, the experimental setup has been applied to different combinations of fluorescent dyes (Rhodamine B Chloride, Sulforhodamine 640, DCM special, a mixture of DCM/Kiton Red 620) and suitable solvents (pure water, methanol, ethanol) for different concentrations of solute. Some combinations of dye and solvent are not possible, for example, the DCM special is insoluble in water **[65]**.

Penetration depth has been investigated considering the fluorescence emission coming from the top few microns of fluid adjacent to the flow cell.

Some combinations indicate that the expected penetration depth is too large to be optimal: the emission light travels for several hundred microns within the dye solution for the DCM dye dissolved in methanol (Fig. 4.5).

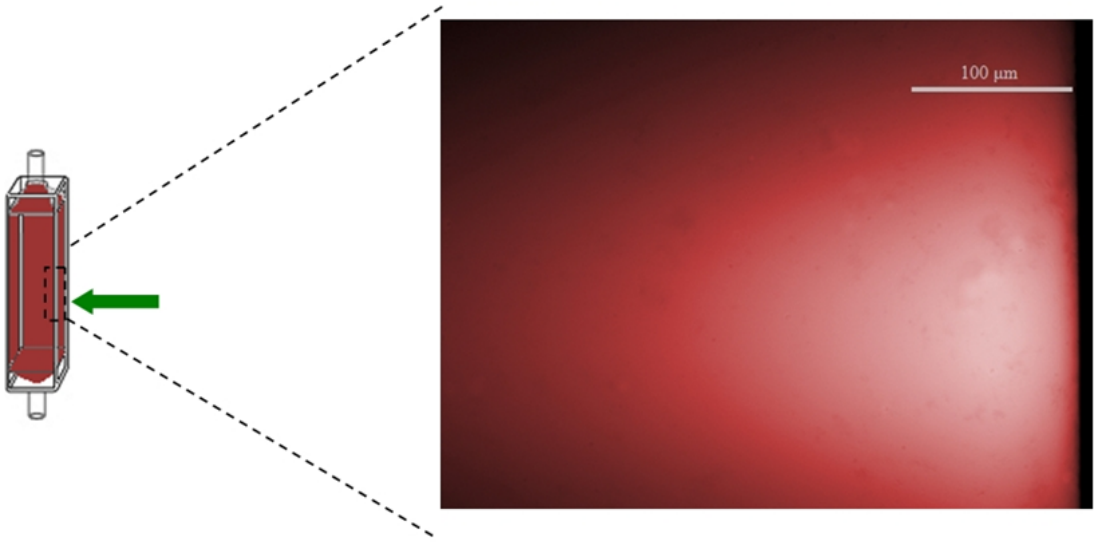

Fig. 4.5: (left) Schematic representation of flow cell device filled up with a saturated solution of DCM special in methanol exposed to the laser light (the green laser arrow).
(Right) The image, taken with the system described above, highlights the light penetration depth into the sample (a few hundred microns).

In other cases the dye-solvent combination provided a light penetration depth that varied a lot according to the solvent used, such as the case with Sulforhodamine 640 dissolved in water or in methanol (Fig. 4.6). The main reason is that the molar absorptivity of these dyes is strongly dependent on the solvent system.

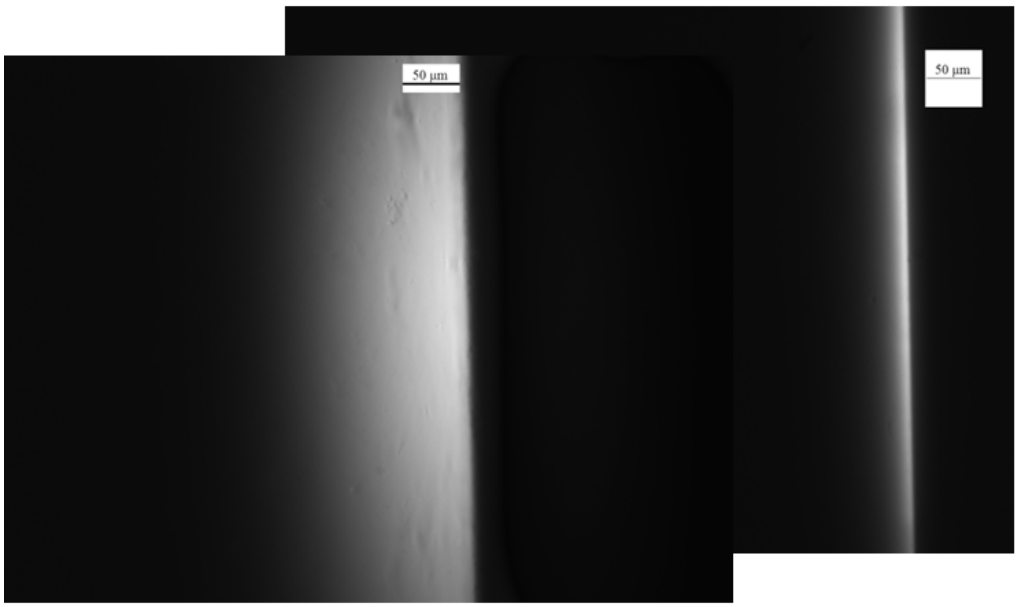

Fig. 4.6: Light penetration depth for Sulforhodamine 640 dissolved in water (left), methanol (right). Dye solution close to saturation in both cases. Saturated concentration levels of 2 mM and 53 mM, respectively. 13× magnification.

In the light of the experimental results, the following diagram (Fig. 4.7) shows that Rhodamine B dye has a suitable dye penetration of < 5 microns, where distance represents the point where the fluorescence emission intensity reduces to 50% of the surface value.

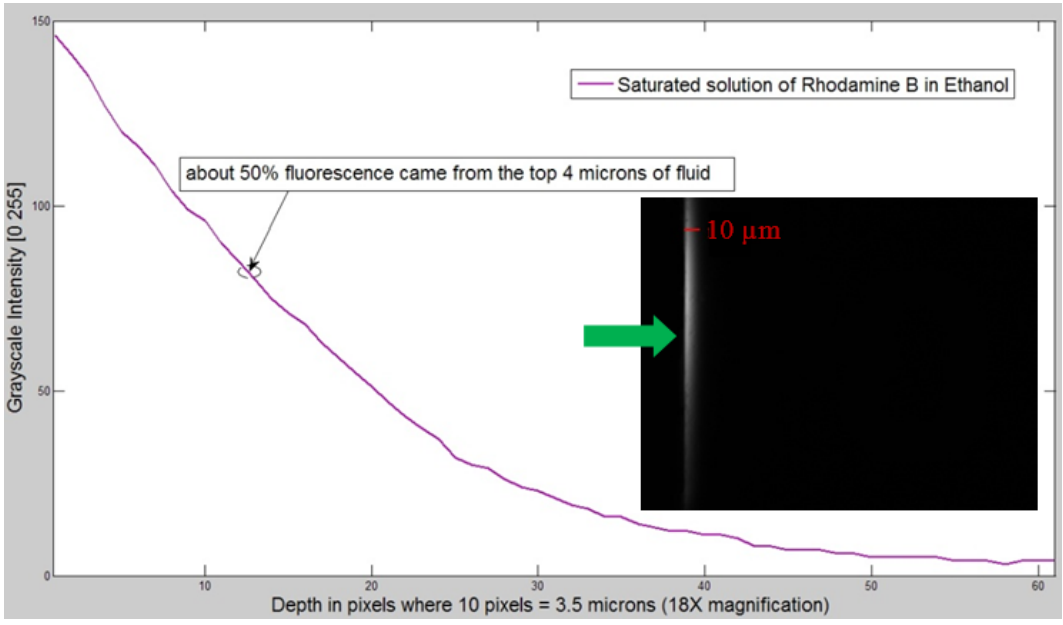

Fig. 4.7: Fluorescence penetration depth for a saturated solution of Rhodamine B in ethanol. The dotted circle represents the point where the fluorescence emission intensity reduces to 50% of the surface value.The inset also shows the experimental image collected (the green arrow indicates the laser light direction).

It has been decided to use the 50% intensity point as a quantitative measure of light penetration. Indeed, one needs to have a point which it can be used reliably to assess the depth of light absorption. Although the 50% point is somewhat arbitrary it is easily identifiable from the gray-scale intensity graph. Hence, it is enough to calculate the mean value of the peak intensity and the lowest level detected. This criterion has been verified experimentally. It should be noticed that, for any reasonable stimulated light intensity, the exponential trend (previous Fig. 4.7) tends to shift vertically along the y-axis. This doesn't practically affect its x-coordinate (in particular the 50% intensity point keeps being easily identifiable). According to the previous graph (Figure 4.7) it also means that the majority of the light will come from a film depth that is less than this thickness. In this case, the fluorophore was dissolved in ethanol (spectrophotometric grade, low absorbance in visible light **[66]**) achieving the maximum solubility[1] at 48 mM. Therefore, the basic model of Beer-Lambert law has been confronted with some candidate fluorescent dyes providing a better evaluation of light depth penetration in the saturation condition. Fig. 4.8 depicts the behaviour of Sulforhodamine 640 in methanol where the penetration depth (to 50% of the surface value of the initial fluorescence intensity) is determined over a range of dye concentrations both experimentally and theoretically.

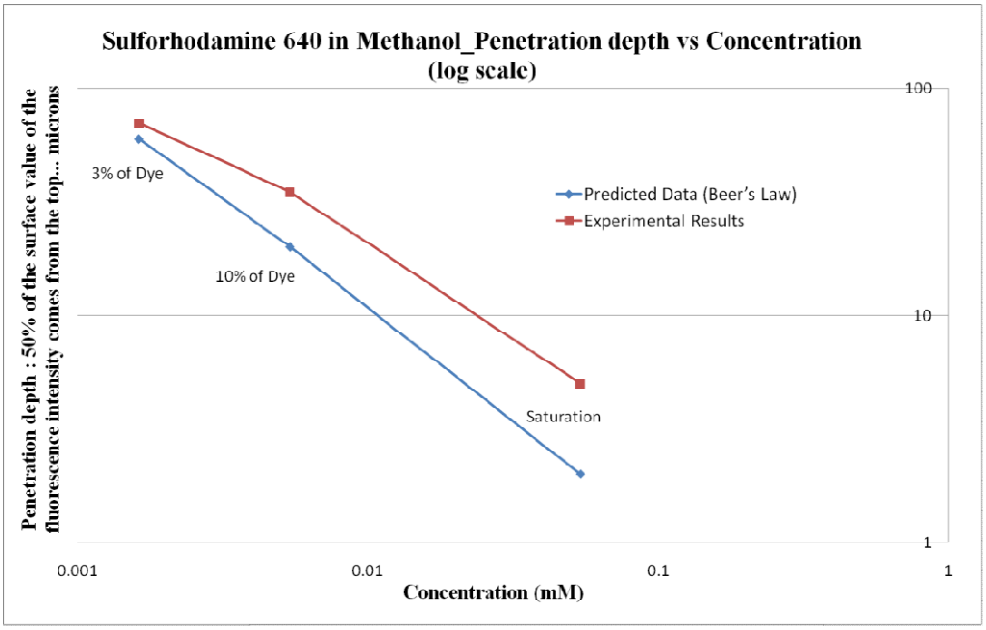

Fig. 4.8: Comparison between theoretical (Beer's law) predictions and experimental results for a dye solution of Sulforhodamine 640 in methanol. The above graph indicates that the law is not strictly obeyed for increasing concentration of solute (fluorescent dye).

([1]) The solubility of a solute is the concentration of the saturated solution

These results indicate that the deviations from the direct proportionality of the Beer-Lambert law become appreciable at higher concentrations (near saturation).
The main question is the following. For the same depth penetration, which is the best dye solution in terms of fluorescence emission?

4.3.3 *Fluorescence intensity*

If one looks at the previous figures (4.7 & 4.8) it appears that two fluorophore solutions (Rhodamine B in ethanol and Sulforhodamine 640 in methanol) provide similar performance in terms of light penetration depth (around 5-10 microns).
Hence, it important to include a further parameter in order to completely characterize the dye solutions analyzed so far.
Hence, first step is to compare the emission spectra of the two dye solutions with the CCD camera (Basler scA1400-17fm) spectral response (Figure 4.9).

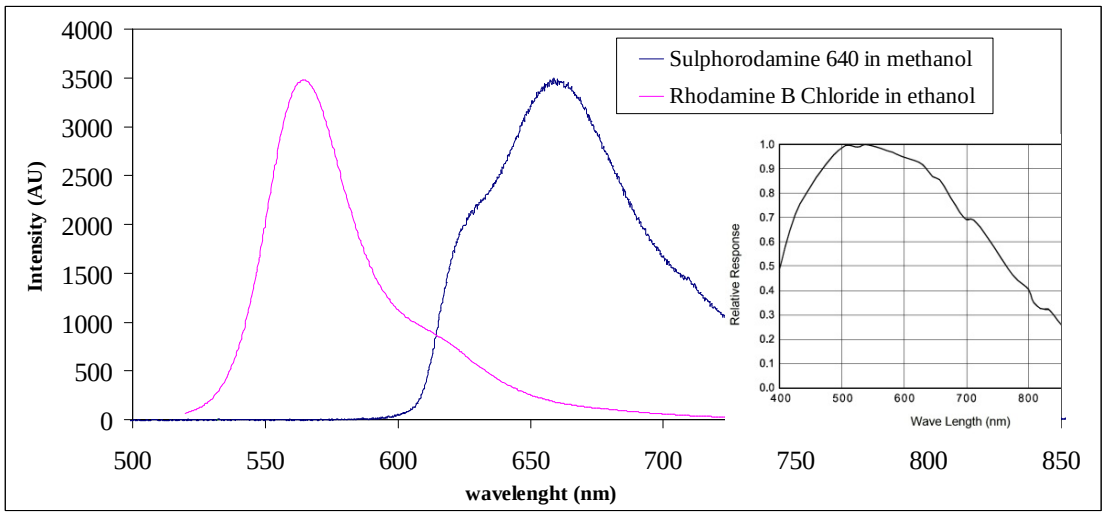

Fig. 4.9: Fluorescence emission spectra for Rhodamine B chloride (in ethanol) and Sulforhodamine 640 (in methanol). For the same fluorescence emission, Rhodamine B matches the maximum sensitivity of the CCD camera shown in the inset (Rhodamine B raw data from **[60, 61]**; camera data from Basler scout user's manual).

Figure 4.9 highlights that, for the same fluorescence emission intensity, the system CCD camera would provide a better performance with the dye solution showing an emission spectrum where the CCD camera efficiency is higher, in this case

Rhodamine B dye in ethanol. Therefore, a fluorescence detection system has been identified in order to measure the average fluorescence emission for the previous fluorescent dyes. Four essential elements of the fluorescence detection system can be identified from the preceding discussion:

- an excitation light source (532 nm, green light);
- a fluorophore (DCM special, Rhodamine B Chloride, Sulforhodamine 640);
- a specific wavelength filter to select the emission spectrum isolating the excitation spectrum;
- a detector that registers the emission spectrum converting the intensity into a digital signal to be processed;

Figure 4.10 illustrates the fluorescence detection system developed.

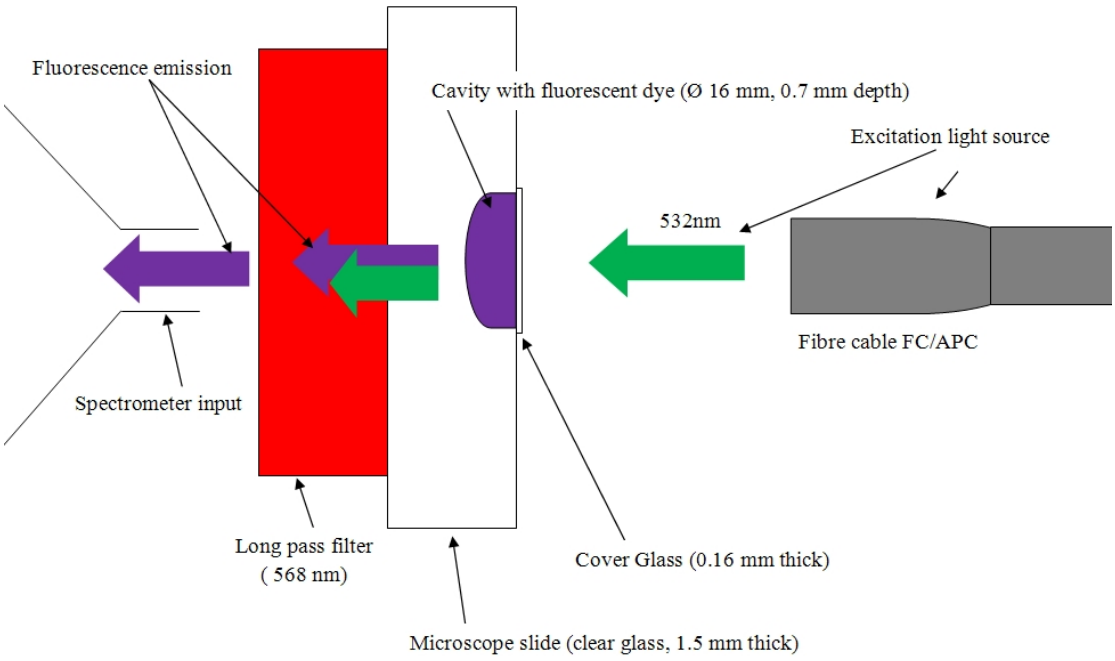

Fig. 4.10: Schematic diagram of the proposed fluorescence detection system which is composed of an excitation light source (via a fiber cable), a microscope slide with a concave cavity in the middle suitable for the dye solution, a long pass filter (568 nm), and a spectrometer (Ocean Optics HR-2000) connected to a computer via USB port. The role of the long pass filter is to reject (attenuate) the incident light source (~1mW at 532 nm).

In addition, the long pass (568 nm) filter used did not significantly block the fluorescence. The transmission spectrum of the long pass filter has been confirmed experimentally (Figure 4.11).

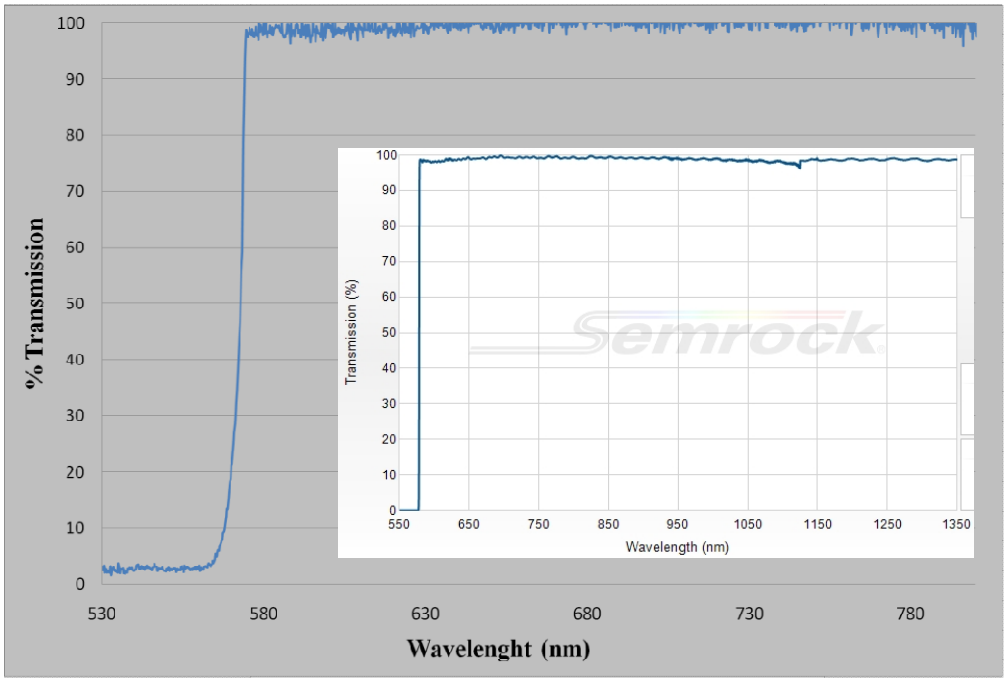

Fig. 4.11: Measured transmission spectrum for the long pass filter (568 nm) used for the fluorescence detection. The experimental data are in good agreement with the manufacturer data sheet (inset of the figure; courtesy of Semrock, Inc.).

In order to get reliable measurements the raw spectra collected have been normalised to remove the illumination spectra and any instrument response functions (due to the fibres, spectrometer).

The average fluorescence intensities have been taken at different concentrations of the solute dissolved into a suitable solvent (starting from 1% of solute concentration up to saturation).

Eventually, the resulting emission spectrum has been integrated to give an overall intensity for the particular dye concentration and solvent under the same condition of excitation light source (~ 1mW at 532 nm).

However, with no fluorophore present the intensity obtained was exactly zero up to the saturation.

For instance, the following graph illustrates the fluorescence emission data for Rhodamine B dissolved in ethanol and Sulforhodamine 640 in methanol (Figure 4.12).

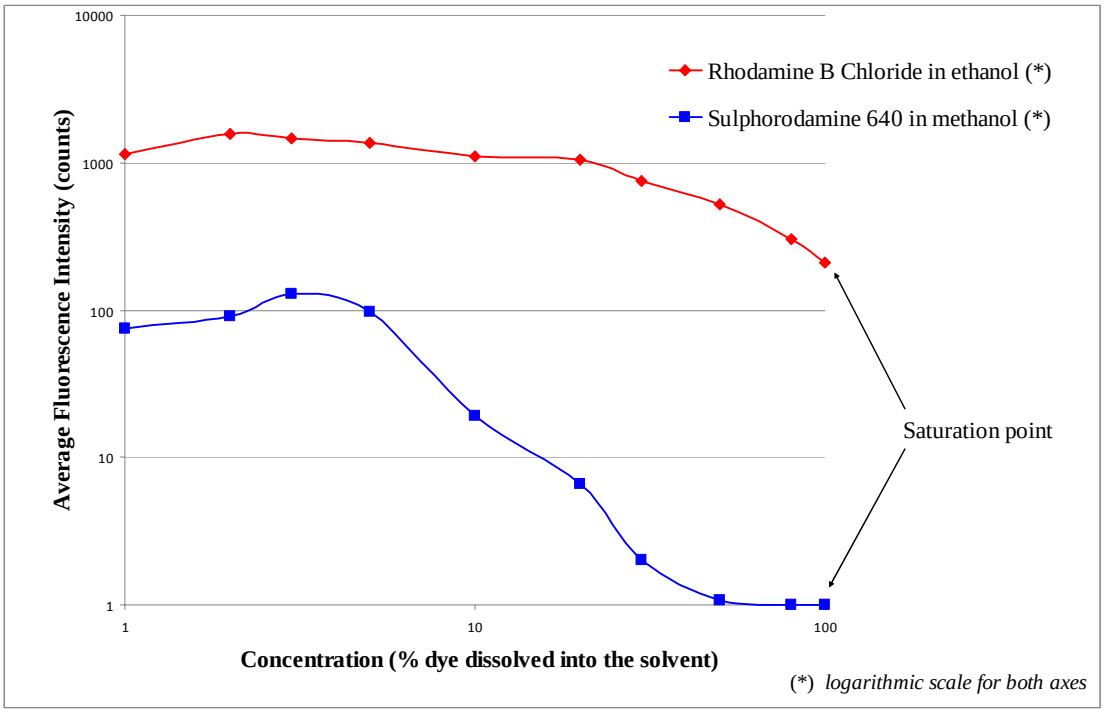

Fig. 4.12: Emission of fluorescence for Rhodamine B (in ethanol) and Sulforhodamine 640 (in methanol) dyes. The former shows a relevant fluorescence emission up to saturation. The latter shows a fluorescence emission strongly dependent on the solute concentration.

From the data collected one can be able to answer the previous question. Figure 4.12 highlights that the two dye solutions show a significant difference in terms of fluorescence efficiency. In particular, for the same expected light penetration depth (~5-10 μm, at the saturation point shown in Fig 4.12), the ratio of the relative fluorescence intensities is 1:200 for Sulforhodamine 640 in methanol to Rhodamine B dye dissolved in ethanol.

It would be clear that the solvent in which the dye is dissolved plays an important role in terms of fluorescence efficiency **[67]**. Indeed, the fluorescence efficiency is a function of how the dye dissolves in the solvent and any intermolecular forces acting that may affect the absorption and emission bands of the fluorophore.

In addition, a number of processes can lead to a reduction in fluorescent intensity (*quenching*) and hence, they have to be considered during the data collecting process.

Indeed, the emission (intensity) of fluorescence is proportional to the concentration of the fluorophore in a reasonable range of concentrations. In other terms, at high concentrations of fluorescent dyes the proportionality is no longer satisfied due to short-range interactions between the fluorophore and the local molecular environment (*self-quenchin*g or inner filter effect, **[68, 69]**). This effect can be quite pronounced as shown for Sulforhodamine 640 in methanol (Fig. 4.12) where it is thought that the high dye concentration gives re-absorption of the fluorescence emission.

Photobleaching occurs when, under high-intensity illumination conditions, an excited fluorophore permanently loses the ability to fluoresce due to photon-induced chemical damage. Extent of photobleaching is dependent on the duration and intensity of exposure to excitation light **[70]**. Therefore this effect has been reduced in two ways: the fluorescent dyes (dissolved into the solvent) were exposed to the same light power of 1 mW (at 532 nm) and their emission spectra recorded with the same exposure time of the CCD detector (100 ms, average of 10 frames) and fresh dye was moved into the cuvette for each measurement.

Finally, a comparative graph (Figure 4.13) is presented showing the average fluorescence intensities and the depth of penetration for the different combinations of dye-solvent examined. The solute concentration ranges from 1% to saturation (100%). In correspondence of the saturated solutions (text labels on the right side of Figure 4.13) an evaluation of light depth penetration is reported for each dye-solvent combination. These last values come from the experimental measurements (previous Section 4.3.2) where the 50% intensity point as a quantitative measure of light penetration. For instance, it is interesting to note that Sulforhodamine 640 dissolved in methanol, and Rhodamine B in ethanol show high differences in fluorescence emission intensity although the estimated light depth penetration is similar (5 μm and 4 μm, respectively).

Other combinations of dye and solvent, as Sulforhodamine 640 in water and DCM in Methanol, highlight which the expected penetration depth is too far to be optimal (> 100 microns). In other cases, such as the saturated solution of Sulforhodamine 640 and ethanol, although the fluorescence emission intensity is sufficiently strong the emission light travels for more than one hundred microns within the dye solution (about 120 μm).

Therefore, the best candidate dye is Rhodamine B (chloride) dissolved in ethanol because it shows sufficiently strong absorption but without significant loss of emission intensity with increasing dye concentration (up to the saturation where the expected penetration depth has been experimentally estimated).

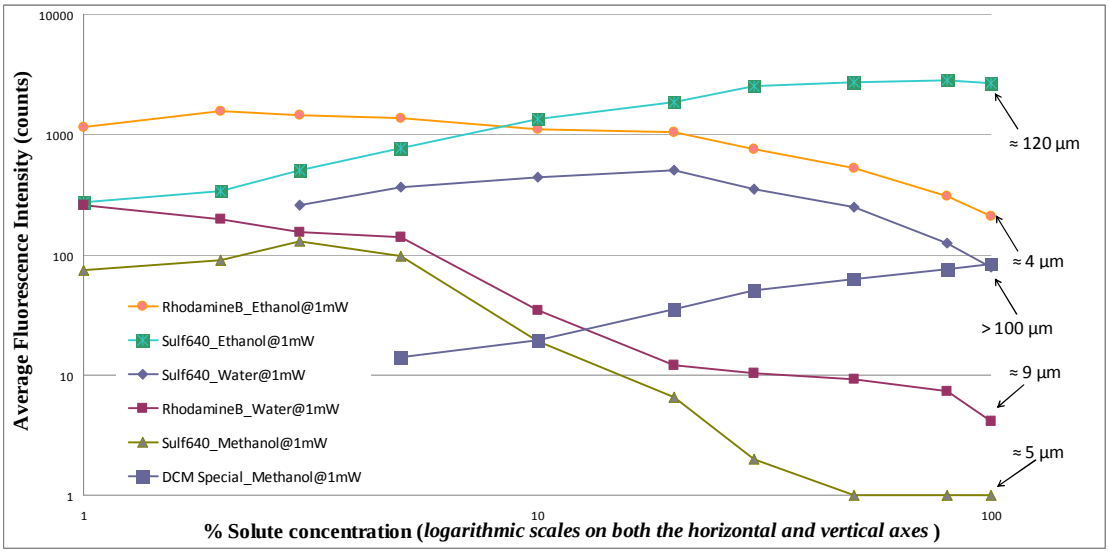

Fig. 4.13: The above graph plots the average fluorescence intensity (vertical axis) against the solute concentration (this last expressed as a percentage; 100%, represents the saturation point for a particular dye-solvent combination). The text labels on the right side of the graph provide the expected penetration depth as experimentally estimated (see Section 4.3.2) for each saturated combination (dye + suitable solvent). Some combinations are far too be optimal because they show either a weak light absorption (e.g., Sulforhodamine 640 in water and DCM in Methanol) or strong absorption but a significant loss of emission intensity (Sulforhodamine 640 dissolved in methanol). The combination of Rhodamine B chloride and ethanol is the best one because it shows sufficiently strong absorption (light depth penetration of about 4 µm) but without significant loss of emission intensity with increasing dye concentration up to the saturation (where the expected penetration depths have been estimated).

4.4 *Summary*

The data in Figure 4.13 brings together the depth of penetration and fluorescence emission intensity available for a range of dye and solvent combinations and from dilute to saturated concentrations. Suitable dyes for measuring the surface topography of thin fluid films by fluorescence based fringe projection require the emission to be derived from the minimum thickness of the film, i.e. the top few microns. However, it is also necessary that under these conditions the fluorescence emission is sufficient for full field imaging in fringe projection. Therefore the identification of a dye with sufficiently strong absorption but without significant loss of emission intensity with increasing dye concentration is required. The best candidate dye against these criteria is Rhodamine B chloride dissolved in ethanol.

The next chapter will start with some experimental setups for generating structured light by the interference between two coherent waves by means of a diffraction grating and a twin fibre system. The approach developed in this thesis will make use of a narrow band laser illumination (532 nm, green light at 200mW) in order to provide a stable excitation for the fluorescent dye dissolved in the fluid.

Chapter references

[56] Spectral Modelling in Fluorescence Microscopy. Available from http://www.semrock.com/Data/Sites/1/semrockpdfs/whitepaper_spectralmodelinginfluorescencemicroscopy.pdf (Accessed: 27/05/2013).

[57] PHOTONICS SOLUTIONS LTD. Laser Dye Properties. Available from http://www.photonicsolutions.co.uk/dyeinfo.asp (Accessed: 27/05/2013).

[58] INGLE JDJ and CROUCH SR (1988). Spectrochemical Analysis. New Jersey, USA: Prentice Hall (ISBN: 0138268762).

[59] HECHT J (1992). The Laser Guidebook. New York: McGraw-Hill, Inc. (ISBN: 9780470088906).

[60] DIXON JM, TANIGUCHI M, and LINDSEY JS (2005). PhotochemCAD 2. A Refined Program with Accompanying Spectral Databases for Photochemical Calculations. *Photochem. Photobiol.* **81**(1), 212-213.

[61] DU H, FUH RCA, LI J et al. (1998). PhotochemCAD: A computer-aided design and research tool in photochemistry. *Photochem. Photobiol.* **68**(2), 141-142.

[62] TURNER DESIGNS, INC. Absorbance Theory & Application. Available from http://www.turnerdesigns.com/t2/doc/appnotes/S-0075.pdf (Accessed: 27/05/2013).

[63] RAY G (2008). Photochemestry. Meerut: GOEL Publishing House. (ISBN: 8129711540).

[64] EDMUND OPTICS, INC. 1951 USAF Contrast Resolution Target.

Available from http://www.edmundoptics.com/testing-targets/test-targets/resolution-test-targets/1951-usaf-contrast-resolution-target/1331 (Accessed: 27/05/2013).

[65] PHOTONICS SOLUTIONS LTD. DCM (fluorescent dye). Available from http://www.photonicshop.co.uk/FE/Pdf/DCM.pdf (Accessed: 27/05/2013).

[66] CHRISTIAN GD (2003). Analytical chemistry. New York: Wiley. (ISBN: 0471214728).

[67] SAUER M, HOFKENS J and ENDERLEIN J (2011). Handbook of fluorescence spectroscopy and imaging: from single molecules to ensembles. New York: Wiley (ISBN: 9783527316694).

[68] MORRIS MC (2010). Fluorescent biosensors of intracellular targets from genetically encoded reporters to modular polypeptide probes. *Cell. Biochem. Biophys.* **56**(1), 19-37.

[69] MORRISON LE (2008). Basic principles of fluorescence and energy transfer. *Methods Mol. Biol.* **429**, 3-19.

[70] INVITROGEN CORPORATION. Introduction to Fluorescence. Available from http://probes.invitrogen.com/resources/education/tutorials/1Intro/player.html (Accessed: 27/05/2013).

Chapter 5

Building the optical system

This chapter describes the experimental setups studied in order to obtain structured light by the interference between two coherent waves: by means of a diffraction grating (grating based fringe projection) or a pair of single mode fibres (twin fibre system) in order to illuminate the object under observation.
The analysis continues considering the performance of the above techniques against the noise. Moreover, this chapter will focus attention on the construction of a fringe projection system based on a 200 mW laser at 532 nm (green light). Some improvements of the basic system will be analysed in section 5.2 (hardware section) and section 5.3 (software section). The principle of fringe projection forms the basic concept behind the surface mapping of the fluid film (static and dynamic) developed in the next following chapters.

5.1 *Experimental setup for producing laser based fringes*

The use of projected fringes is a well-established technique for measurement of surface shape **[71-78]**.
The technique involves projecting fringes at an angle to the direction observation, i.e. it is a triangulation approach.
The basic idea is that the shape of the observed fringes gives information about the surface profile.
In order to become familiar with all the elements involved in this method (fringe source, CCD camera, image acquisition and image processing) a range of experimental setups for producing laser based fringes were studied. Whereas the majority of fringe projection systems use digital projectors as the fringe source, in the approach developed in this thesis narrow band laser illumination is necessary to give sufficient excitation for the fluorescent dyes dissolved in the fluid. Therefore, experimental setups were evaluated for the production of laser based fringes.

Figure 5.1 shows the standard set-up used for the measurement by projected fringes.

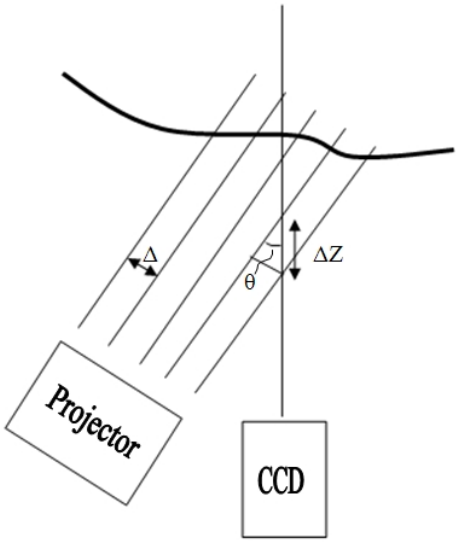

Figure 5.1: Schematics of projected fringes system (projector, camera CCD) and its parameters, Δ (fringe separation at object), θ (projection angle), ΔZ (fringe depth observed from the camera) (see also Fig. 5.5).

The "projector" represents the system used to project fringes onto the object under observation. In this thesis the projector is either a grating system [section 5.1.1] or a twin fibre system [section 5.1.2].

The CCD camera captures an image of the fringe pattern from an angularly displaced viewpoint compared to the projector and the images are saved into the computer for post processing.

Quantitative analysis of the shape can be carried out by extracting the phase distribution of the fringes. Usually methods based on temporal phase shifting or Fourier transform phase analysis of the pattern, are used to do this.

The former has been mentioned (chapter 2) in reference to the work of Decré and Baret **[33]**; the latter in the paper of Ambrosini & Schirripa-Spagnolo **[48]** (see Chapter 3).

Generation of a stable fringe pattern requires some considerations over the physical phenomenon known as *interference*: light waves, when superimposed, will add if they meet in phase or the troughs will cancel the crests if they are out of phase; these phenomena are called constructive and destructive interference (Figure 5.2).

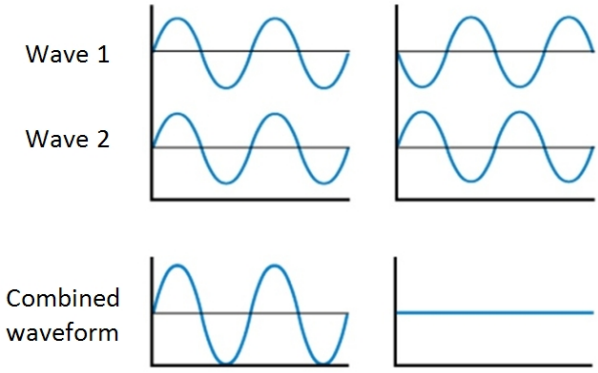

Figure 5.2: Constructive and destructive interference (adapted from solar-center.stanford.edu). In practice, light waves vary as a function of time very rapidly with a bandwidth far in excess (about 6×10^{14} Hz at 532 nm, green light) of that of a detector. Therefore what is actually captured is the time average of the interference intensity (e.g. by means of photodiodes, CCD cameras).

Interference fringes are bright (constructive interference) or dark (destructive interference) bands caused by beams of light that are in phase or out of phase with one another. Stable interference patterns are formed only by radiation emitted by *coherent sources* (i.e. the phase difference between the waves is constant). In addition, if two (or more) beams are to interfere to produce a stable pattern, they must have very nearly the same frequency **[79]**.

In accordance with the principle of superposition, it is possible to derive the two-beam interference equation (between two waves of the same frequency) **[80]**:

$$I = I_1 + I_2 + 2\sqrt{I_1 \cdot I_2}\cos\delta \qquad \text{(Eq. 5.1)}$$

where I_1 and I_2 represent the irradiance of the individual beams, I is the total irradiance (i.e. the time-average energy flux of the light wave) of the two light waves, and δ is the phase difference between the two waves at any location.

A significant frequency difference would result in a rapidly varying, time-dependent phase difference, and consequently the interference term would average to zero during the detection interval.

So, it is necessary to adopt a laser (532 nm, green light, in our experimental setup), with suitable temporal and spatial coherence, as the light source in the system shown in Figure 5.1. A narrow bandwidth laser, unlike an incandescent source, produces a beam in which all the components bear a fixed relationship to each other.

5.1.1 *Grating based fringe projection*

A practical system can be constructed using fringe projection with a *grating*: a diffraction grating consists of a transparent material into which a very large number of uniformly spaced wires have been embedded. Alternatively the periodic structure can be formed by repeated variations in the thickness of the grating. One section of such a grating is shown in Figure 5.3. At certain points in the forward direction the light passing through the spaces (or slits) in between the wires will be in phase, and will constructively interfere. The interaction of a light wave with the grating can be broken down into a directly transmitted component and a series of diffraction orders either side of the directly transmitted beam.

The diffraction orders appear at angles such that the waves diffracted by neighboring slits of the grating are in phase.

The condition for constructive interference can be understood by studying Figure 5.3. Whenever the difference in path length between the light passing through different slits is an integral number of wavelengths of the incident light, the light from each of these slits will be in phase, and will form an a bright diffracted image order at the specified angle. Mathematically, the relation is known as *grating equation* **[81]**:

$d \cdot \sin\theta = m \cdot \lambda$ (for normal incidence and m = …-2,-1,0,1, 2,… is an integer)

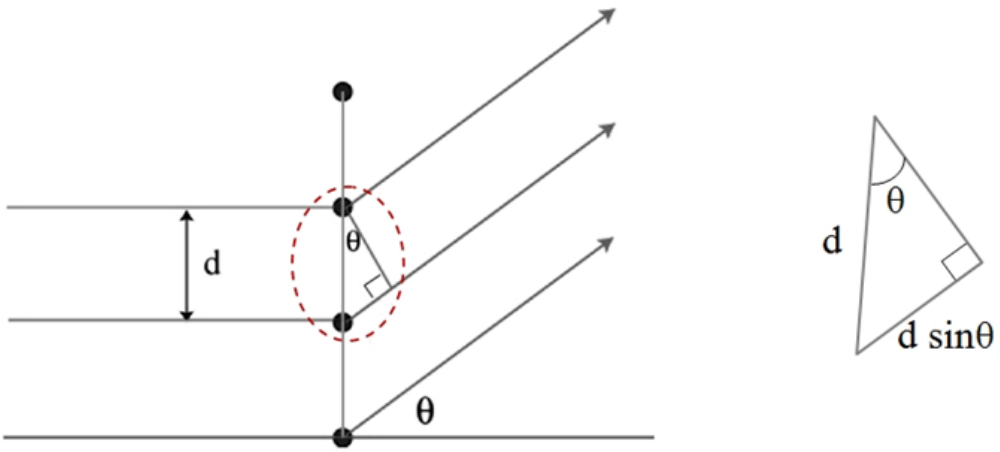

Figure 5.3: Geometry determining the conditions for diffraction from a multi-wire grating (d, grating pitch, is the distance between adjacent slits, θ is the angle the re-created image makes with the normal to the grating surface as shown in the inset picture; adapted from **[81]**)

If a monochromatic light source shines on the grating, images of the light will appear at a number of angles θ_1, θ_2, and so on (Figure 5.4a, adapted from **[81]**).
The image created at θ_m is called the m_{th} order image. The 0_{th} order image is the light that shines straight through the grating.
For application to fringe projection the laser beam must be expanded to illuminate the desired field of view and in general it is possible to observe the overlapping of the zero and first orders as in the image captured in the laboratory (Figure 5.4b).

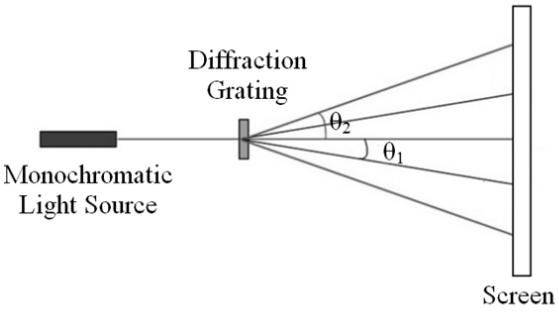

Fig. 5.4a: Geometry of diffraction orders (see Fig 5.6 for further details)

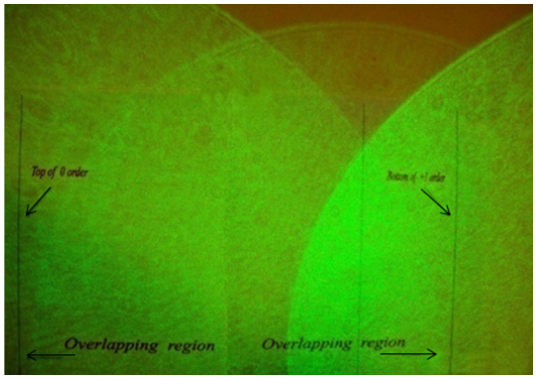

Fig. 5.4b: Image of 0_{th} and 1_{st} order diffraction

A grating with a high (833/mm) number of slits (grooves) has been selected because the resolving power is directly proportional to the total number of grooves.
In accordance with the right-angled triangle in Figure 5.5, the ratio between fringe separation at object (Δ) and sine of projection angle (θ) equals fringe depth as viewed from the camera (Eq. 5.2). This last determines the depth resolution achievable.

$$\frac{\Delta}{\sin\theta} = \Delta Z \qquad \text{(Eq. 5.2)}$$

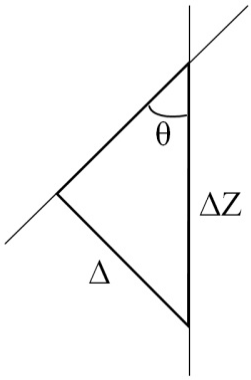

Figure 5.5: Definition of system parameters: Δ (fringe separation at object), θ (projection angle), ΔZ (fringe depth from camera).

For example, if the expected phase resolution (fraction of one fringe) is 250 and the depth resolution target is 2 μm then the fringe depth from the camera is 500 μm. This last multiplied by the sine of projection angle (θ) gives the required fringe separation at the object as seen from the projector (Δ).

Figure 5.6 shows a layout of the laser based fringe projection system with the grating: according to the grating equation, for normal incidence, in our setup the first order diffracted angle occurs at about 26.3º (532 nm, laser wavelength and 1200 nm, grating pitch). R and D are 1 mm and 310 mm, respectively. Microscope objectives are suited to focusing collimated laser beams since a collimated laser is essentially a point source at infinity. In our setup, the microscope objective (Thorlabs RMA40) next to the grating has a magnification of 40×, working distance of 1.2 mm and NA, numerical aperture (i.e. the measure of the objective's ability to collect diffracted light) of 0.65. The NA is defined as the sine of the angle β.

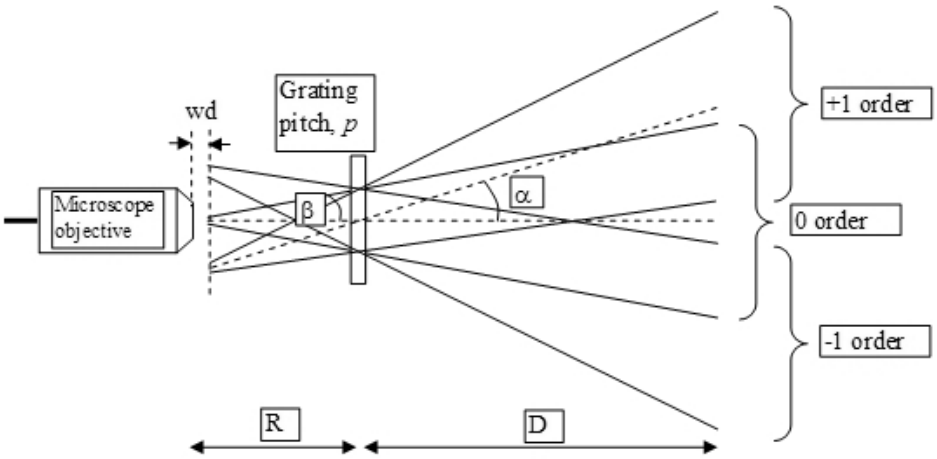

Fig. 5.6: Geometry of grating fringe illumination system (α, angle between diffraction orders; wd, microscope objective working distance; R, distance between laser output and grating; D, distance between grating and screen; β, the sine of this defines numerical aperture of microscope objective)

A high value of this last parameter is desirable because a value between a third and a quarter of numerical aperture is useful at the distance of projection.

If one considers interference caused by overlap of the 0 and +1 beams (previous Figure 5.6) then the lateral extent of projected fringes corresponds to the overlapping region between the 0 and +1 order diffraction orders. By using a microscope objective with NA = 0.65 angle β is about 40.5º (in practice a lower angle than this is useful as power drops off towards the edges). Overlap between the orders occurs between the top of the zero order and bottom of the first order. In the setup of Figure 5.6 an overlapping region of about 345 mm has been created at the screen at a distance of 310 mm from the grating (as shown in previous Figure 5.4b).

The practical grating ‘projector’ is composed of: 532 nm (50 mW) laser, fiber optics (single mode, 460 HP from Thorlabs), three microscope objectives with different magnification/numerical aperture (10×/0.18, 20×/0.40, 40×/0.65) and the diffraction grating (1200 nm, grating pitch) as shown in Figure 5.7a.

In addition a CCD camera (Basler scA1400-17fm) acquires images at 1280 × 960 pixels with 15 fps. The camera provides good sensitivity to light at 532 nm and has been selected to match the frequency of the laser and also is suitable in the orange (600-620nm) which corresponds to the emission wavelength of popular fluorescent dyes (Fig. 5.7b).

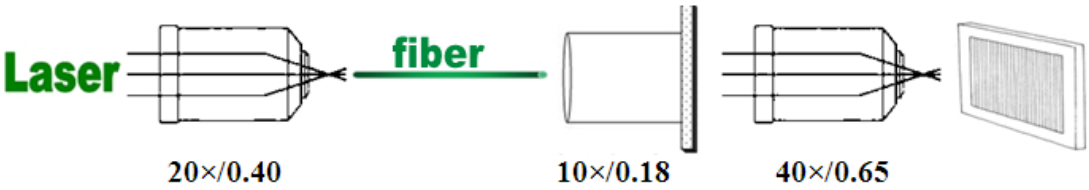

Figure 5.7a: Practical fringe projection system with grating: 20×/0.40 microscope objective (m.o.) collimates light coming from laser into the fibre; 10×/0.18 m.o. is used to collimate the light from the fibre; finally the last m.o. focuses light on the diffraction grating in order to generate fringe pattern.

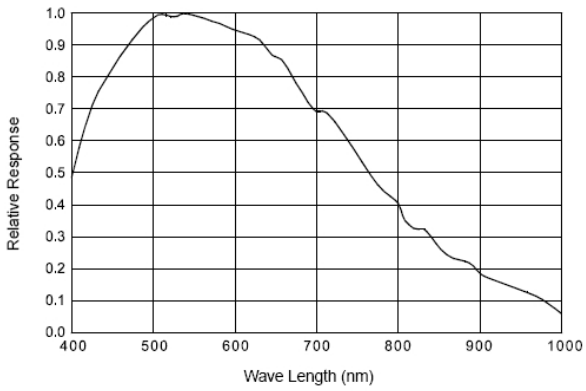

Figure 5.7b: CCD camera spectral response. Maximum sensitivity corresponds to the green light (data from http://www.graftek.com/pdf/Manuals/basler/ScoutUsers_Manual.pdf).

The system has been tested by using fringes that were being viewed scattered from a white panel (opposite the diffraction grating) and imaged by the camera located to the side of the grating.

In Figure 5.8 it is possible to see a typical image (with 20 fringes / cm).

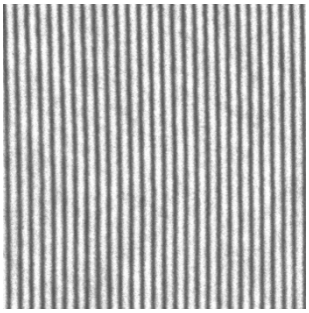

Figure 5.8: Fringe pattern: by using D=310 mm and R=1mm, the fringe period was measured as being slightly less than 500 microns at the object.

The system has also been tested using two microscope objectives (by removing the 10×/0.18 microscope objective) in order to improve image quality with less optical components in the system. The performance of the grating fringe projector system is presented in section 5.1.3.

5.1.2 *Twin fibre system*

The system based on amplitude splitting interferometers operates by observing the phase interference between two beams of light split from a single source.
Fibre optic interferometers of this type are based on the classic Michelson interferometer (Figure 5.9, adapted from 2006 Encyclopaedia Britannica, Inc.).

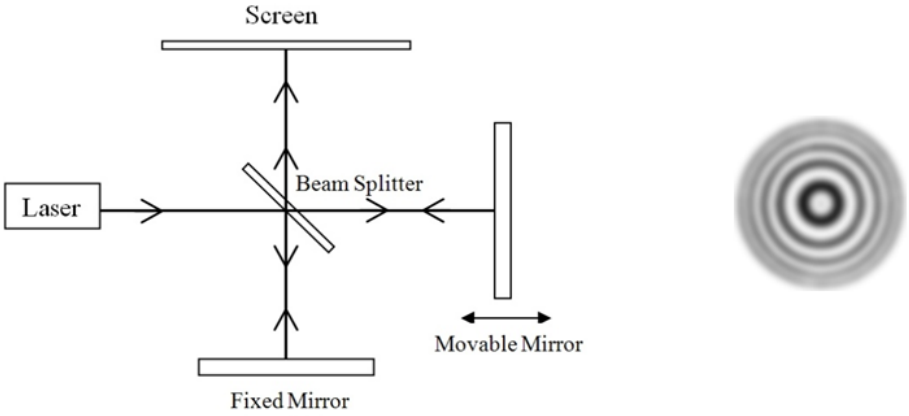

Figure 5.9: Michelson interferometer. In the interferometer pictured on the left, the light from a monochromatic source is split into two beams which recombine to form a visible pattern of areas of constructive and destructive interference (i.e. bright and dark fringes, on the right). When the effective length of one of the optical paths is changed by some means, then any given point on the interference pattern shifts from light to dark or vice-versa for each half-wavelength of path length change.

However, the use of fibre allows greater miniaturization and flexibility compared to the rigid mirror based Michelson interferometer.

A fibre optic amplitude splitting interferometer uses a narrow band laser (in our setup, 532 nm, green light) as a source (see schematics, above, and physical realization, below of Figure 5.10).

In this case, coherent fringes can be generated by means of a pair of single mode fibres (460 HP, Thorlabs) via a single coherent source and directional coupler (2×2, 50:50 ratio).

Alternatively, coherent fringes can be formed by bringing the two output fibres parallel and with a small separation **[82, 83]**.

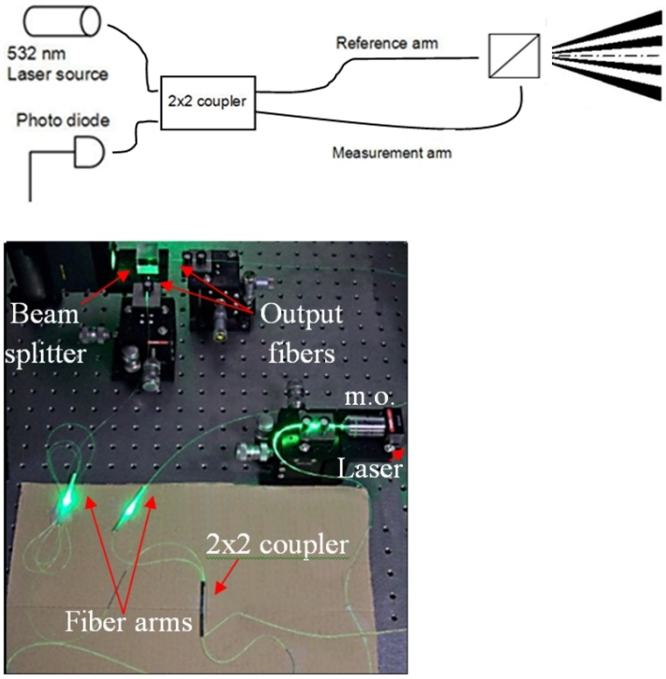

Figure 5.10: A twin fibre based fringe projector. The source is launched into one arm of a 2×2 coupler. As it passes through the coupler, the light beam is then split into two equal intensity arms, reference arm and measurement arm. These are brought together via a beam splitter to project onto the object. The virtual spacing of the two distal fibre ends generates an interference function and the projected fringes (see also Fig. 5.11). The light travelling down the two output fibres (that form the projected fringes) generate back reflections from the distal ends of the fibres. These back reflections return through coupler to the photodiode at the 4th arm where an interference signal is detected that depends on the relative optical path lengths of the two output fibres.

A 4% reflection of light results from the change in refractive index between the fibre and air interface at the distal ends of the fringe projection fibres. By measuring the light intensity, the path length difference between these fibres can be measured. In a fibre laser interferometer, the two beams of light from the reference and measurement arms interfere with each other when they are caused to overlap.
Depending on the phase difference, the interference may range from totally constructive to totally destructive (Figure 5.11).

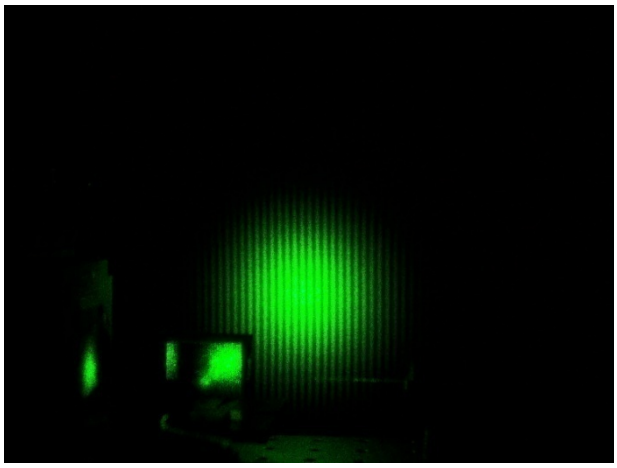

Figure 5.11: Experimental image showing fringe pattern. Note the beam splitter and the two fibre ends in the foreground.

However, the main problem of this technique is that the phase of the projected fringes is sensitive to variations in fibre length caused by environmental instabilities: temperature and vibration.
In general, in an interferometer, the desired measured length and undesired environmental disturbance both contribute to the change in path length and corresponding phase change **[84]**. One way of predicting the resultant amplitude of two interfering beams is to consider the intensity of each as a vector in the complex plane. Considering two different light waves, $\vec{E}_1$ and $\vec{E}_2$ (same frequency, λ) are superimposed then (for simplicity it is assumed the plane waves are both linearly polarized and propagating along the x-axis, see Appendix A):

$$\vec{E}_1 = \vec{A}_1\, e^{j(kx-\omega t+\varphi_1)} \quad \text{and} \quad \vec{E}_2 = \vec{A}_2\, e^{j(kx-\omega t+\varphi_2)} \qquad \text{(Eq. 5.3)}$$

where $\vec{A}_1$ and $\vec{A}_2$ are the vector complex amplitudes, $k = \frac{2\pi}{\lambda}$ is the wave number, $\omega = 2\pi\nu$ is the circular frequency (with ν the temporal frequency), and φ_1, φ_2 being the initial phases for the light waves, $\vec{E}_1$ and $\vec{E}_2$, respectively.

Hence, in the ideal case the time average intensity (irradiance) recorded at the detector will be given by **[79, 80]**:

$$I = I_1 + I_2 + 2\sqrt{I_1 I_2}\cos(\varphi_1 - \varphi_2) \qquad \text{(Eq. 5.4)}$$

Where $I_1 = A_1^2$ *and* $I_2 = A_2^2$, φ_1-φ_2 is the phase difference between the two fields superposing at the detector.

In reality, the phase terms that are the argument of the cosine term in equation 5.4 will contain an additional component due to the environmental disturbances.

The basic idea for minimizing these disturbances is to induce an equal and opposite change in path length to the system (compared to that induced by the environmental disturbance) by using a fibre wrapped around a piezoelectric material **[84]**.

In general, the thermal disturbance of the environment (fluctuations of the fringe pattern) causes a change in relative length between reference and measurement arm in the interferometer, which can be measured in terms of wavelengths of light.

An active phase stabilisation was explored and whilst it operated correctly (in terms of fringe pattern stabilization over the measurement interval **[72]**) it was found that phase stabilisation was not very robust. Furthermore, LabView code had been developed to acquire the images needed for temporal phase shifting sufficiently quickly that stabilisation was found practically to be unnecessary (Section 5.3).

5.1.3 *Noise Analysis: comparison of 3 sets of projected fringes*

Quantitative phase imaging is useful to provide the surface height information. Each fringe in an interferogram represents an area of data ranging from [0; 2π] or [-π; π]; indeed, as seen in Decré & Baret paper (Chapter 2, **[33]**), the interference phase is given from the arc tan function of a set of phase stepped intensities. The final phase map obtained from a series of phase stepped interferograms (or from Fourier fringe analysis of a single interferogram) also contains 2π ambiguities because of the principal value range of the arc tangent function.

Phase maps (called *wrapped phase maps*) need to be "unwrapped" by removing 2π ambiguities to obtain a contiguous phase distribution representing the measurand.

The procedure of constructing the continuous natural phase is called *phase unwrapping*. That being stated, three sets of projected fringes have been compared in our experiments: using the grating system with three microscope objectives, using the grating system whilst removing the objective to collimate the light from the fibre and using the twin fibre fringe projection system. The performance of each configuration has been compared by examining the noise present in the unwrapped phase across an image row (orthogonal to the direction of the fringes).

A single image was obtained using each fringe projection system. By using Fourier transform phase analysis the wrapped phase distribution was determined. Then, the Matlab 1-D unwrap function was used to generate a smooth phase distribution and assess the noise level against a low (cubic) order polynomial fit (see Appendix B). Finally, the standard deviation of the residual errors between the unwrapped phase and the fitted phase distributions has been taken as a measure of the phase noise in the projected fringe patterns. Figure 5.12 highlights the phase resolution obtained with the grating setups was poor compared to the value gained with the twin fibre system.

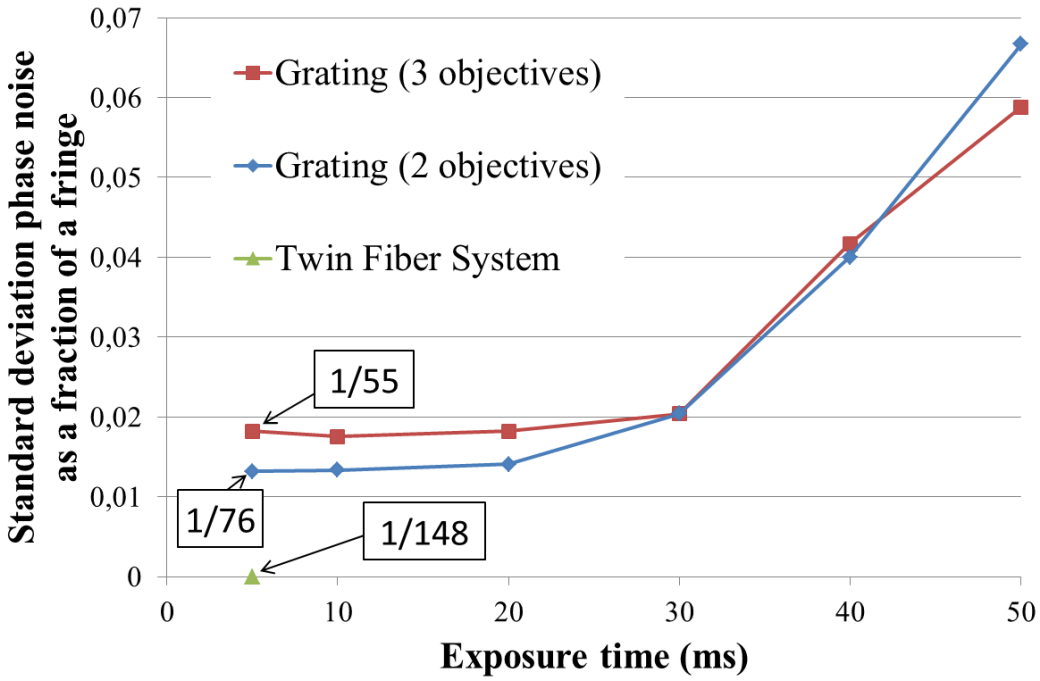

Figure 5.12: The above plot relates to the grating system with two and three microscope objectives. For reference, the twin fibre system is also reported but only for an exposure time of 5 ms in order to not saturate the camera CCD. The images have been evaluated using Fourier based phase analysis: by keeping constant the F number (diaphragm of 50 mm lens used with camera CCD), several images of phase profile of the fringes have been captured (taking care not to saturate the camera CCD); the central row of data has been examined by taking 3 rows across the fringe images (1/4, 1/2 and 3/4 of each image) and each one has been analysed using the FFT and noise analysis codes checking the unwrapped phase was monotonic before recording the phase noise. Exposure times between 5 ms and 50 ms.

However, it is important being careful to avoid saturation of the fringes as this causes error in the wrapped (and unwrapped) phase and verify that the unwrapped phase is monotonic before recording the phase noise: one needs to take care not to saturate the camera CCD (high exposure times) or capture images too dark (very low exposure times).

For example, all conditions being equal, beyond 10 ms the unwrapped phase is no more monotonic with a twin fibre system (Figure 5.13) owing to saturation of the camera.

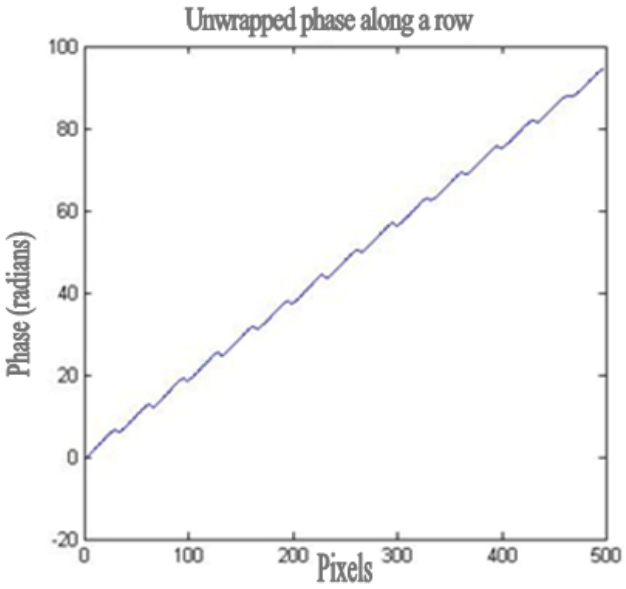

Figure 5.13: Loss of monotonicity in the unwrapped phase (twin fibre system, 15 ms exposure time)

Set of values obtained using three microscope objectives setup show noise levels higher (on average) than two microscope objectives setup (previous Figure 5.12). Probably, some quality improvement may be achieved as there would be less optical components in the previous system (with two microscope objectives).
Images obtained with twin fibre system show a net improvement about noise level (Figure 5.14).

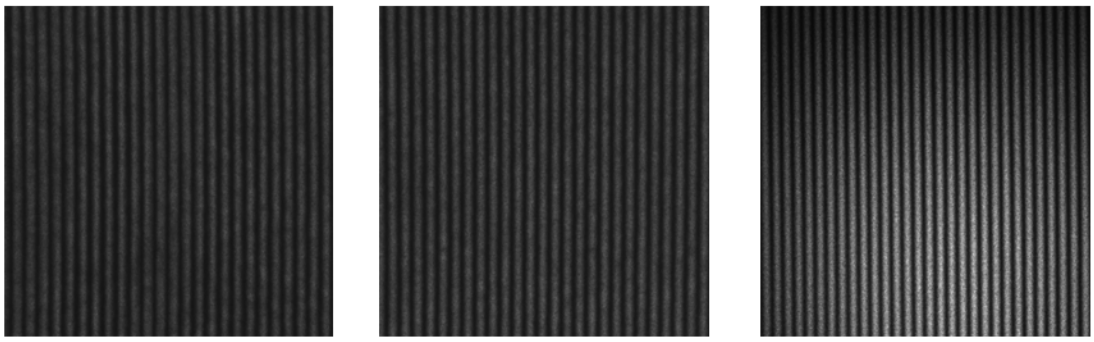

Figure 5.14: Twin fibre system (right) shows a noise level lower (1/148 of a fringe) than 2 objectives (middle, 1/76 of a fringe) and 3 objectives (left, 1/55 of a fringe) grating system setups (5ms, exposure time for each image). See previous Figure 5.12 for further details.

For example, the standard deviation (STD) phase noise (as average of 3 rows) is 1/148 of a fringe (5 ms, exposure time) by adopting the twin fibre system. In general, the twin fibre system produces better phase resolution but it inherently suffers stability problems from environmental effects.

In the light of these results one can draw conclusions. The three setups show a different performance towards environmental instabilities: the grating setup (2 and 3 objective system) gives inherently stable fringes as the interfering beams are generated in air which has more stable optical properties; the fringes from the twin fibre setup are quite unstable as the interfering beams propagate in different fibres and the fibre is very microphonic (i.e. it picks up acoustic vibrations) which changes the phase of the light in the fibre hence giving interference instabilities.
However, the grating system gives comparatively poor phase resolution, it is believed that the loss of resolution is due to imperfections in the grating itself. The twin fibre setup gives a very good phase resolution as the beams only propagate in air from an idealised point source (the end of the fibre).
The following sections will study the solutions adopted in order to reduce the environmental sensitivity of the fibres for the twin fibre setup.

5.2 *Improvement of Twin Fibre System - Thermal Enclosure System*

The fringe projection configurations described in the previous sections show that the coherent fringes can be generated by means of single mode fibres and a coherent source (laser).
In particular, the flexibility and versatility of the twin fibre system opens the door to phase stepping techniques applied to determine the (fringe) phase map from static and dynamic fluids.
For example, it would be clear that a twin fibre based fringe projector provides a higher flexibility compared to traditional systems such as a Michelson interferometer.
The idea of mounting one of the output fibres on a 3-axis translation stage allows control of the spacing of the projected fringes by adjusting the separation of the fibre ends (Figure 5.15). Indeed, the fibres and beam splitter configuration performs an analogous role to the slits in the traditional Young's double-slit experiment **[85]**.

The separation (w) of two consecutive maxima or two consecutive minima, near the center of the projected field (point O in Figure 5.15, where θ is very small), is given by $w \cong \frac{D \cdot \lambda}{d}$

where D is the distance from the sources to the target and d is the separation of the two output fibers[1] (by analogy with the train of plane light waves incident on a barrier containing two narrow slits separated by a distance d, see also previous Fig. 5.3).

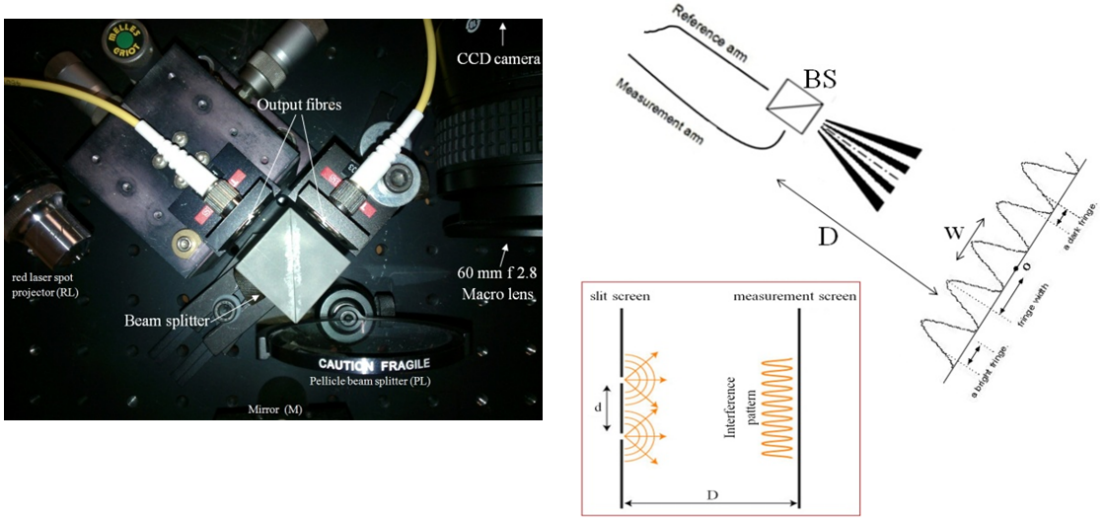

Figure 5.15: Fringe projection configuration (laboratory arrangement, left). Fringe projector (beam splitter and output fibres), CCD camera and the other system elements have been mounted on a breadboard in order to have all the elements rigidly connected to each other (see Fig. 6.5- 6.6, chapter 6 for details). By adjusting one of the two output fibres the separation of the projected fringes can be changed. The schematic (right, not to scale) shows the physical principle: coherent light from the unfolded output fibres can be recombined into the beam splitter (BS) in a configuration analogous to Young's double-slit experiment (see inset picture in red).

However, implementation of phase stepping algorithms and data capture software requires the environmental sensitivity of the fibres to be compensated (over the measurement period).

Optical fibres make it possible to have long, noise-free paths in a small place, so that high sensitivity can be achieved.

([1]) The interference pattern is assumed to be far away from the sources (D >>d). For this reason, this analysis is often referred to as the "far-field approximation".

Therefore, the twin fibre configuration has been readapted in order to make the overall system much more flexible (with the view to phase stepping implementation) whilst being able to tolerate the intrinsic environment sensitivity of the fibres. The optical setup is shown below (Figure 5.16).

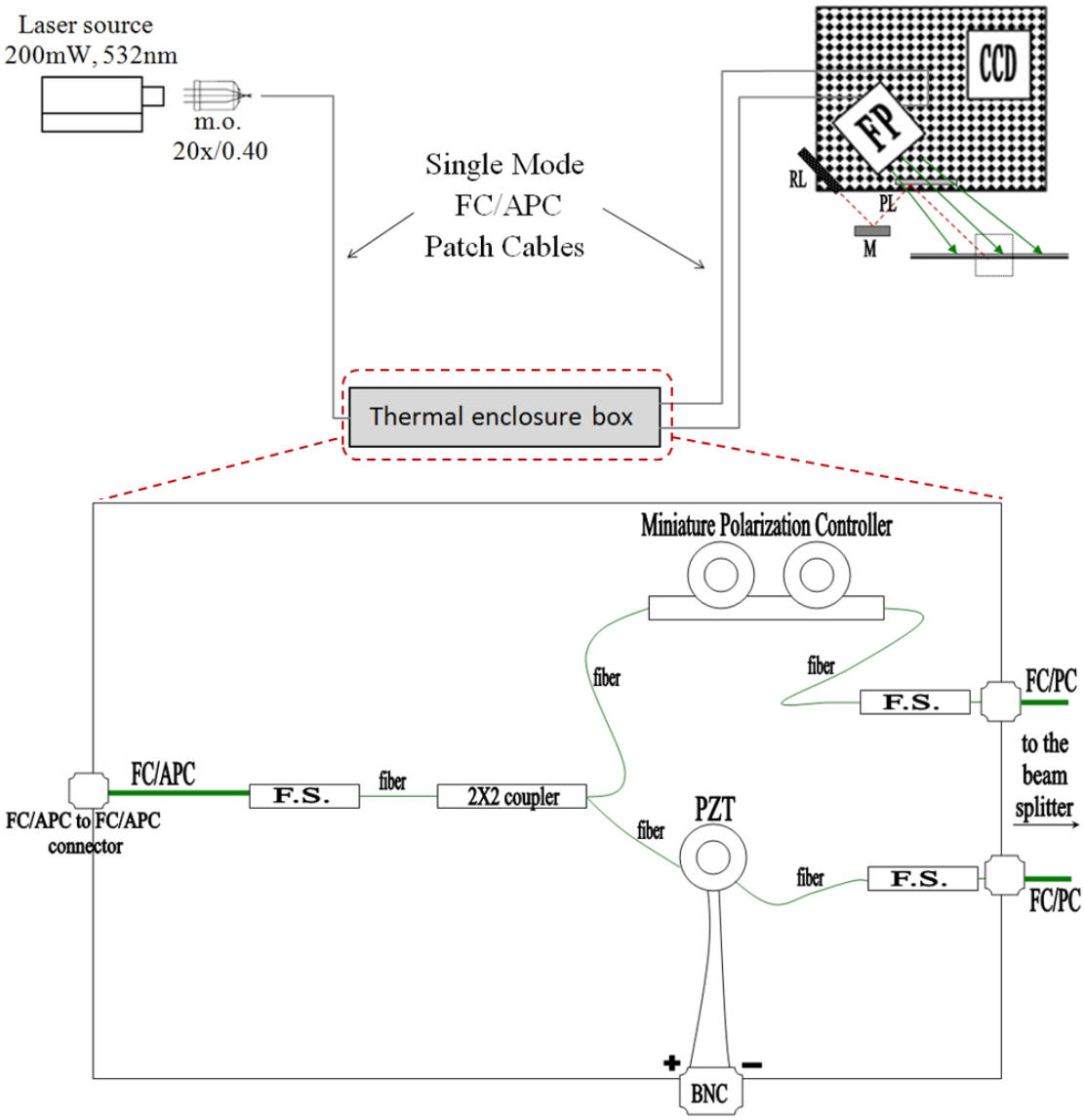

Figure 5.16: The optical setup used for the experiments. (Top left) 20×/0.40 microscope objective (m.o.) collimates light coming from laser into the FC/APC cable which is ideal to reduce back reflections. The narrow key connector utilizes a ferrule that has an 8° angle polished tip, ensuring return losses lower than -60 dB. (Top right) Fringe projector, FP (see Fig. 5.15, left) mounted on a bread board with the CCD camera and the other calibration elements (see Fig. 6.5, chapter 6 for details). The central block ("thermal enclosure box") assembles the bare fibre with the 2×2 single mode fibre coupler (used to divide and recombine the beams), the piezoelectric transducer (PZT; two meters of fiber used) suited to allow phase shift by applying a voltage at the BNC connector (see section 5.3), the polarization controller adopted to optimize the output fringe visibility **[86]**. Fusion splices (F.S.) join two bare fibres together with minimal loss.

5.3 *Improvement of Twin Fibre System - Phase Stepping Algorithm Implementation*

As explained in the chapter 2 the phase distribution of an interferogram can be determined as **[35]**:

$$\Phi(x, y) = arctan\left[\frac{(I_4 - I_2)}{(I_1 - I_3)}\right]$$

where I_1, I_2, I_3, I_4 are the intensity distribution of four different fringe patterns with 0, $\pi/2$, π and $3\pi/2$ radian phase shifts respectively and *arctan* is the inverse tangent function.

To determine the phase difference between the two interfering beams, one must measure the intensity of the interference fringes while the phase difference between the two interfering beams is changed in a known manner.

Typically, the phase is changed by $\pi/2$ radians between consecutive intensity measurements. Since there are three unknowns, at least three intensity measurements must be made.

A phase shifter will vary the phase difference between the two interfering beams **[87]**.

The simplest way to generate controlled phase steps is to wrap one of the fibres from the coupler around a cylindrical piezoelectric transducer which is driven with an appropriate voltage. The phase change between detector readouts occurs by varying the phase in discrete steps (phase-stepping).

The four-frame phase stepping algorithm is implemented in LabView and can be monitored, in real time, via an oscilloscope. Essentially the optical path difference between the interfering wavefronts is changed in equal steps.

As illustrated in Figure 5.17, the computer controls the phase difference between the two interfering beams sending a phase stepping waveform voltage via the analogue output channel of a multi-channel voltage controller (PXle-1073, National Instruments).

The LabView program is also responsible for the actual frame capture from the frame grabber (usually 15 fps). A solid-state detector (CCD camera) has been adopted to collect the modulated interference fringe pattern at a very large number of points (1280 × 960 pixels).

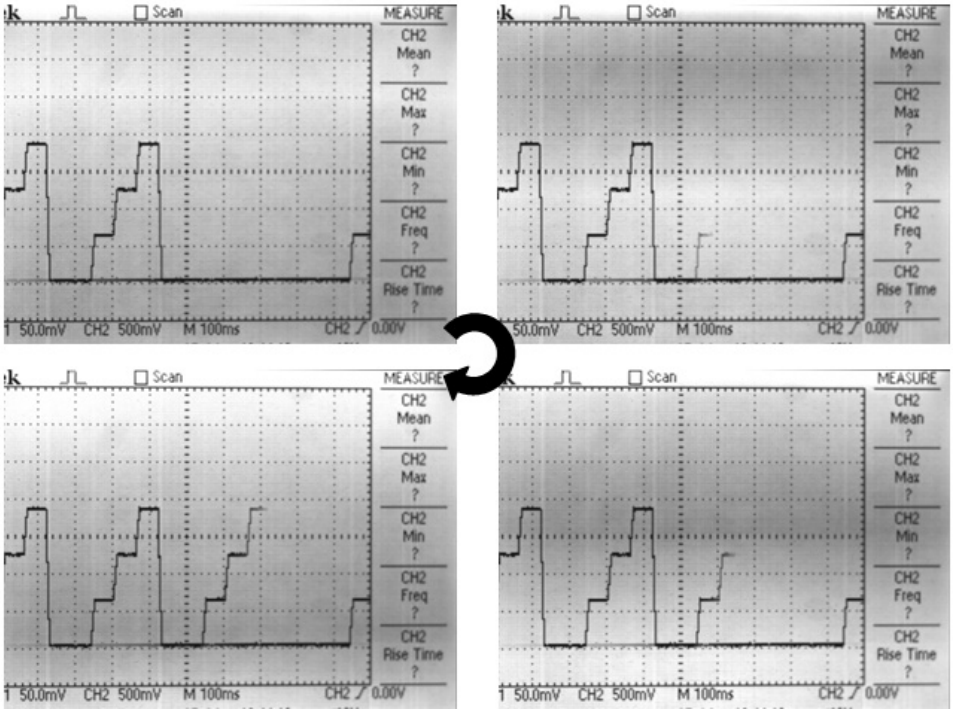

Figure 5.17: Modulation of phase difference: phase-stepping sequence shown from the oscilloscope display. Each screenshot in the sequence illustrates the voltage applied to the PZT in order to generate a $\pi/2$ radian phase change.

The best synchronization between the four stepped images and the CCD camera has been achieved by means of a digital stopwatch with $1/100^{th}$ second readout in order to match the maximum CCD frame rate with the phase stepping interval time (Figure 5.18).

The idea was simple but efficient, making optimal use of the tools involved.

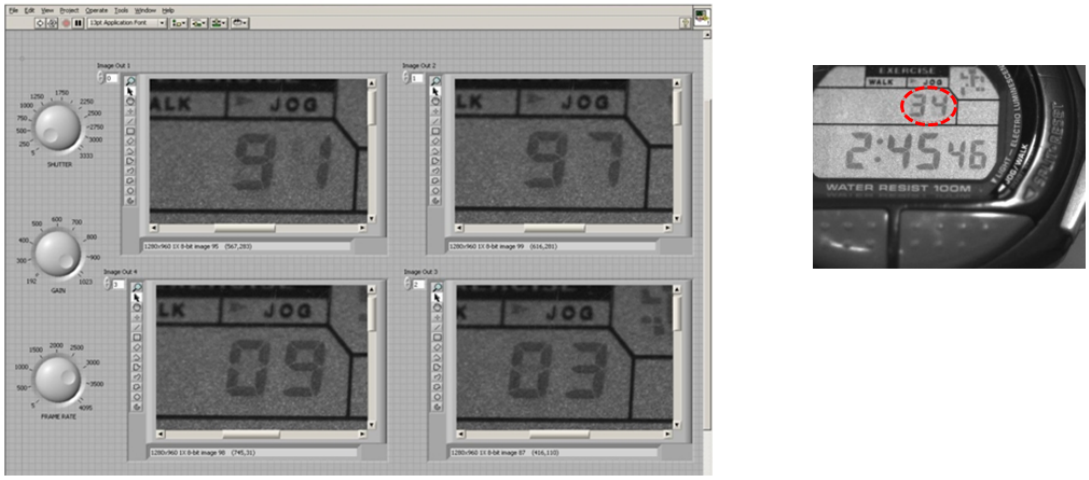

Figure 5.18: Synchronization sequence. (left) The user interface (Labview) shows four frames separated by 6 hundredths of a second (60 ms). (right) Each frame screenshot is taken from a stopwatch (1/100 of a second accuracy).

Finally, the digitized output data can be read directly into computer memory. The LabView program generates a sequence of output frames (typically 6 sets of the four stepped images) according to a first-come, first-served (FCFS) behaviour.

The post-process section relies on a Matlab code which allows the user to select the best 4-frames in terms of phase shift accuracy and intensity range (0-255, 8-bit data), as illustrated in the next figure (Figure 5.19).

The mean phase step, α (ideally 90° at each pixel) has been calculated by means of the Carré algorithm **[88]** applied to the intensity distribution of the four different fringe patterns acquired (I_1, I_2, I_3 and I_4) as follows:

$$\alpha = arctan\sqrt{3\frac{(I_2 - I_3)-(I_1 - I_4)}{(I_1 - I_4)+(I_2 - I_3)}} \qquad \text{(Eq. 5.5)}$$

Hence, the histograms in Figure 5.19 represent the calculated mean phase shift at each pixel of the camera (1280 × 960 pixels). These histograms are a good indicator of the system strength. If these histograms look wider than the ideal value ($\pi/2$) this may mean that vibration issues occur within the system **[88]** as depicted in the top of Figure 5.19.

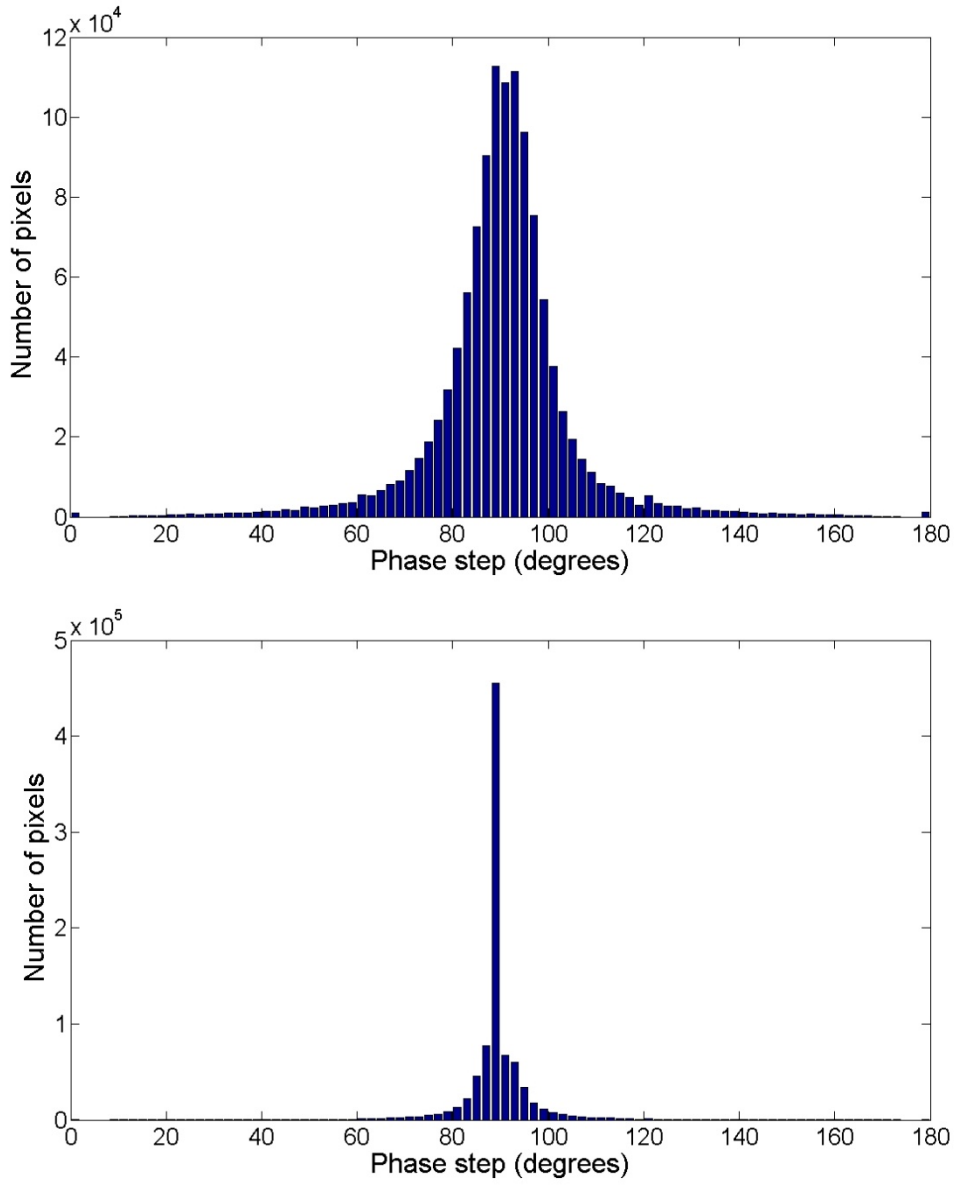

Figure 5.19: Phase shift accuracy. The above Matlab screenshot shows the phase shift distribution for a poor (above) and good (below) four stepped images set. Phase step centered at 90 degrees.

Taking measurements with phase-shifting techniques can be both fast and accurate. The environment in which the measurements are made is critical to ensuring accuracy, because vibration or air turbulence can change the phase difference between the two beams in unknown ways and hence introduce large errors.

To reduce the effects of vibration, all of the phase-shifting frames are taken at a certain exposure time (typically 10-40 ms). In general phase shifting techniques are preferred to Fourier **[89]** analysis (where a single interferogram is collected and processed) as any discontinuities in the phase distribution may produce unwanted

effects (such as ringing) and hence increased errors in the calculated phase in the neighborhood of the discontinuity **[90]**.

The following diagram (Figure 5.20) summarizes the main steps carried out by the operations above.

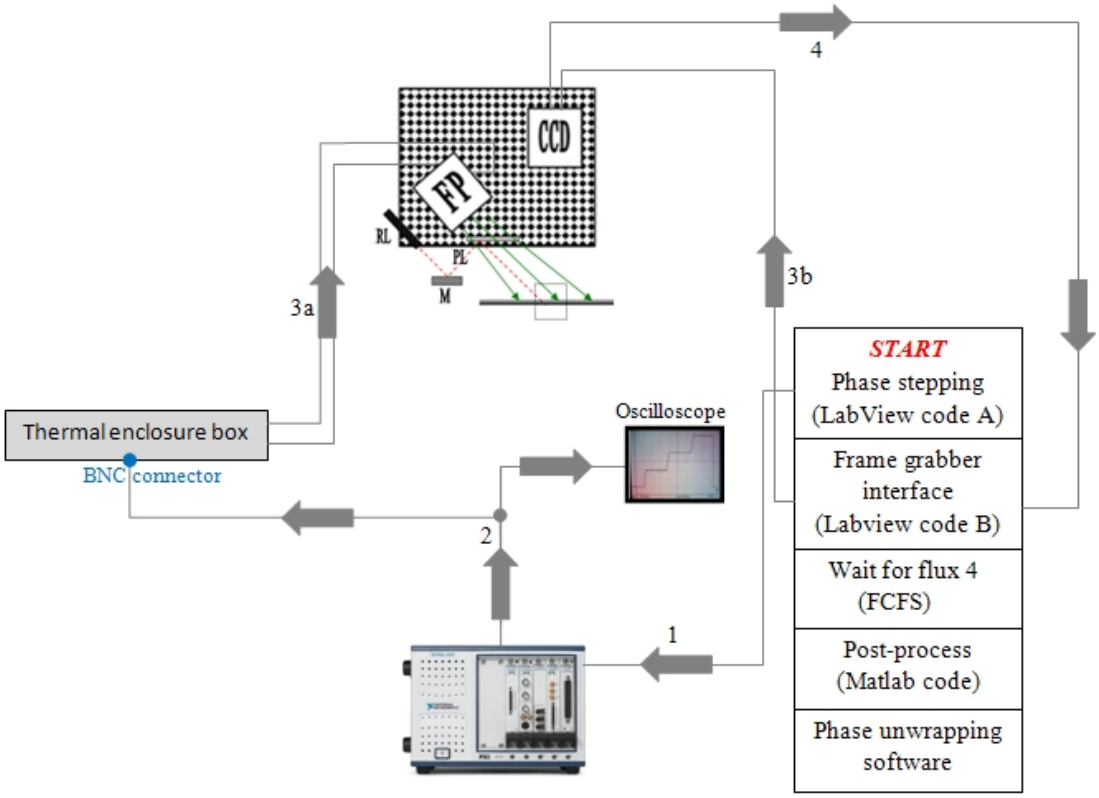

Figure 5.20: The schematic diagram summarizes the main steps of the phase stepping process.

(1) The LabView program output represents the input signal for the voltage controller. (2) This device drives a piezoelectric transducer in order to modulate the phase between the two interfering beams (3a).

The frame grabber interface sends the trigger input to the CCD camera (3b) and accepts (4) the digital streams in output.

5.4 *Summary*

This chapter has described the required experimental setups for generating structured light by the interference between two coherent waves by means of a diffraction grating and a twin fibre system. The approach developed in this thesis makes use of a narrow band laser illumination (532 nm, green light at 200mW) in order to give sufficient excitation for the fluorescent dyes dissolved in the fluid. Therefore, experimental setups have been evaluated for the production of laser based fringes. The setups studied show a different performance towards environmental instabilities and phase resolution: the grating setup (configurations with two and three microscope objectives) gives inherently stable fringes as the interfering beams are generated in air which has more stable optical properties; the fringes from the twin fibre setup are quite unstable as the interfering beams propagate in different fibres and the fibre is very sensitive to vibration or thermal changes in the environment which changes the phase of the wave transmitted by the fibre and hence cause interference instabilities. However, compared with the twin fibre approach the grating system gives poor phase resolution, presumably the loss of resolution is due to imperfections in the grating itself. The twin fibre setup gives a very good phase resolution as the beams only propagate in air from an idealised point source (the end of the fibre). In addition, some improvements have been developed in order to make the twin fibre system robust against the environmental instabilities (thermal enclosure system, section 5.2) and suitable for fast acquisition of temporal phase stepped images by means of a LabView code (phase stepping algorithm implementation, section 5.3). Ideally the thermally isolated temporal phase shift setup provides phase resolution results similar to the ones obtained by FFT analysis from a single image.

The following chapter will describe the calibration process needed to get the relationship between the phase distribution, modulated in the projected fringe patterns, and the height of the object under test.

Chapter references

[71] TOWERS CE, TOWERS DP and JONES JDC (2005). Absolute fringe order calculation using optimized multi-frequency selection in full-field profilometry. *Optics and Lasers in Engineering* **43**, 788-800.

[72] TOWERS CE, TOWERS DP, and JONES JDC (June 2003). Optimum frequency selection in multifrequency interferometry. *Optics Letters* **28**(11), 887-889.

[73] REEVES M, MOORE AJ, HAND DP, and JONES JDC (October 2003). Dynamic shape measurement system for laser materials processing. *Optical Engineering* **42**(10), 2923-2929.

[74] TOWERS DP, BUCKBERRY CH, STOCKLEY BC, and JONES MP (1995). Measurement of complex vibrational modes and surface form-a combined system. *Meas. Sci. Technol.* **6**(9), 1242-1249.

[75] ZHANG Z, TOWERS CE, and TOWER DP (July 2006). Time efficient color fringe projection system for 3D shape and color using optimum 3-frequency selection. *Optics Express* **14**(14).

[76] ZHANG Z, TOWERS CE, and TOWERS DP (August 2007). Uneven fringe projection for efficient calibration in high-resolution 3D shape metrology. *Applied Optics* **46**(24).

[77] SANSONI G, TREBESCHI M, and DOCCHIO F (2009). State-of-The-Art and Applications of 3D Imaging Sensors in Industry, Cultural Heritage, Medicine, and Criminal Investigation. *Sensors* **9**(1), 568-601.

[78] BUCKBERRY CH, TOWERS DP, STOCKLEY BC et al. (1996). Whole-Field Optical Diagnostics for Structural Analysis in the Automotive Industry. *Optics and Lasers in Engineering* **25**(6), 433-453.

[79] HECHT E (1987). Optics. New York: Addison-Wesley (ISBN: 9780201116090).

[80] VEST CM (1979). Holographic interferometry. New York: Wiley (ISBN: 0471906832).

[81] *Measuring wavelengths with a diffraction grating* (2005). Available from http://www.amhslions.com/Science/Phys%20Files/Unit%207%20%28CJWaves%29/Diffraction%20Lab.pdf (Accessed: 27/05/2013).

[82] VALERA JD and JONES JDC (1993). Phase stepping in projected-fringe fibre-based Moiré interferometry. *Electronics Letters* **29**(20), 1789-1791.

[83] LALOR MJ, ATKINSON JT, BURTON DR, and BARTON P (1993). A fibre-optic computer-controlled fringe projection interferometer for surface measurement. *In*: JUPTNER W and OSTEN W, eds. Proc. Fringe '93, Automatic Processing of Fringe Patterns, Berlin: Akademie Verlag.

[84] CREATH K. *Phase-Measurement Interferometry Techniques*. Tucson, AZ 85719, USA: WYKO Corporation 1955 East Sixth St.

[85] YOUNG T (1804). Experimental Demonstration of the General Law of the Interference of Light. Philosophical Transactions of the Roy. Society of London **94**.

[86] KERSEY AD, MARRONE MJ, DANDRIDGE A, and TVETEN AB (1988). Optimization and Stabilization of Visibility in Interferometric Fiber-Optic Sensors Using Input-Polarization Control. *Journal of Lightwave Technology*. **6**(10), 1599-1609.

[87] CREATH K (1993). Temporal phase measurement methods. *In*: ROBINSON DW and REID GT, eds. *In:* Interferogram Analysis: Digital Fringe Pattern Measurement Techniques, Philadelphia: Institute of Physics Publishing, 94-140.

[88] WYANT JC. Phase Shifting Interferometry (1998). Available from http://fp.optics.arizona.edu/jcwyant/Optics513/ChapterNotes/Chapter05/Notes/Phase%20Shifting%20Interferometry.nb.pdf (Accessed: 27/05/2013).

[89] TAKEDA M, INA H, and KOBAYASHI S (1982). Fourier-transform method of fringe-pattern analysis for computer-based topography and interferometry. *J. Opt. Soc. Am.* **72**, 156-160.

[90] FALAGGIS K, TOWERS DP, and TOWERS CE (2009). Phase measurement through sinusoidal excitation with application to multi-wavelength interferometry. *J. Opt. A.: Pure Appl. Opt.* **11**.

Chapter 6

Calibration procedure

The *fringe projection profilometry system* described so far is summarised in the flow chart of Figure 6.1a where the first block represents the system hardware component and the two last blocks the software components.

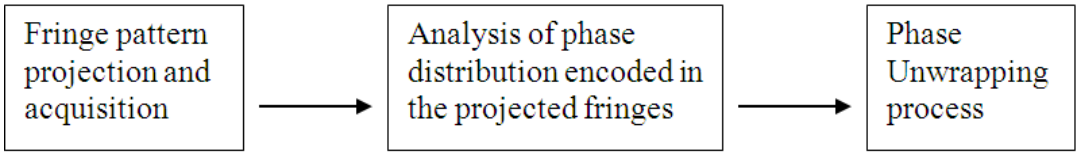

Figure 6.1a: Schematic diagram of the fringe projection profilometry system

In order to allow the conversion of fringe phase maps (unwrapped phase distribution) to surface height distribution it is necessary to introduce a final fourth block (Figure 6.1b), in the above diagram, called *calibration procedure*.

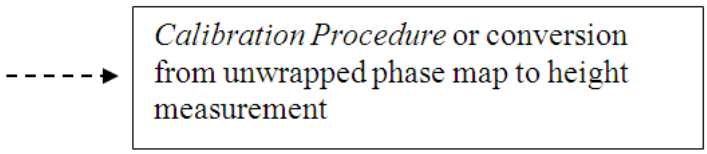

Fig. 6.1b: Final step: phase-to-height calibration of the measurement system

To understand the role played by the calibration process it is useful looking at the fringe projection system developed so far. Indeed the accuracy of 3D height measurement lies on a precise determination of the relative orientation of the CCD camera to the fringe projector.

It was therefore decided to adopt a convenient solution in terms of field of view and mutual location of CCD camera and fringe projector to the object under test (see Figure 6.2).

The adoption of a solid aluminium bread board allows a rigid body motion of the shape measurement system in order to provide a calibration independent of the camera CCD and fringe projector locations. Indeed, once CCD camera parameters (focus, field of view, focal ratio) and fringe separation have been fixed the rigid

body rotation can happen only in the y-z plane (see Figure 6.2). Therefore the overall system is rigid for any rotation in the y-z plane and translation along the z-axis.

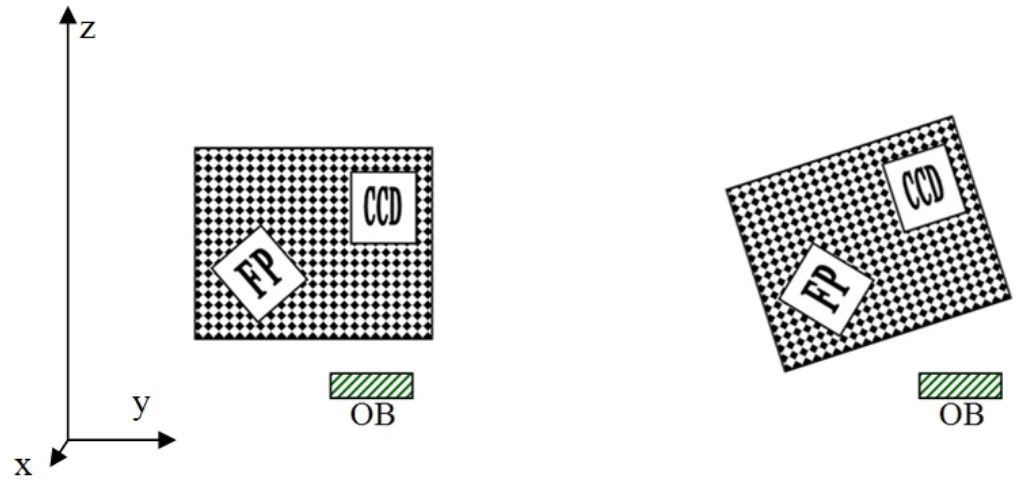

Figure 6.2: Schematic of the measurement system. A solid aluminium bread board allows the object under test (OB) to be illuminated by the fringe projector (FP) at different angles of incidence.

6.1 *Phase-to-height relationship in phase measurement profilometry*

A well-known result is that the phase distribution modulated in the projected fringe patterns corresponds to the height of the object under test **[91]**. It was reported (see Chapter 2, [36]) that for a Twyman-Green interferometer, once the phase of the wavefront (Φ) is known, the surface height (d) at the location (x, y) can be written as

$$\Phi(x, y) = \frac{4\pi}{\lambda} d(x, y) \qquad \text{(Eq. 6.1)}$$

More generally speaking a direct correspondence between the measured phase $\Phi(x, y)$, for each point in the calibration volume, and the height distribution can be found as

$$h(x, y) = f\{\Phi(x, y)\} \qquad \text{(Eq. 6.2)}$$

where f represents a (generally) non-linear relationship between the height distribution, h and the measured phase map, $\Phi(x, y)$. Indeed, the non-parallel axes of the camera and fringe projector generate variable period fringes across a plane orthogonal to the viewing axis (see previous Figure 6.2). This translates into a non-linear relationship between phase and object height distribution **[76]**. Hence, a common approach is based on the search for a polynomial fit in order to relate phase to height at each pixel (x, y) of the image **[73, 92]**.

Usually in the case of experimental data (affected by noise and/or measurements errors) an approximation of the data is more appropriate than an exact interpolation. Normally one might determine the polynomial coefficients[1] by minimising the difference between the polynomial and the original data points ('residuals') in a least squares manner (i.e. instead of solving the equations exactly, the target is to minimize the sum of the squares of the residuals, **[93]**).

Generally the degree of the polynomial used should be as low as possible in order to avoid bad-conditioned phenomena **[94]**.

Moreover, the choice of the polynomial order relies on some geometric optics assumptions. Ideally, the plane perpendicular to the optical axis of an imaging system which contains the focal point of the imaging system (focal plane) should be flat but, in reality, off-axis light usually focuses closer to the objective than it does on-axis light. Hence, a curved field only coincides with a flat detector (CCD camera) at one off-axis distance (Figure 6.3, **[95]**).

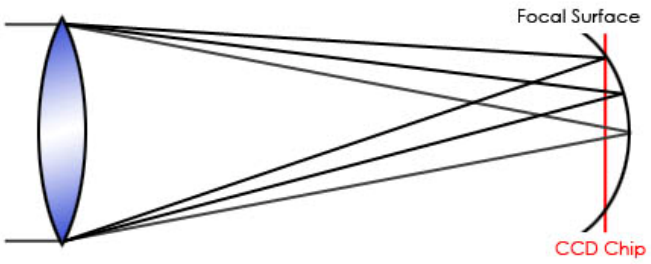

Figure 6.3: The schematic shows the effect of field curvature in the optical system **[95]**.

([1]) On considering n distinct data points (x_1, y_1), (x_2, y_2), …, (x_n, y_n) the order of the polynomial $a_{n-1}x_{n-1} + a_{n-2}x_{n-2} + \ldots + a_2x_2 + a_1x + a_0$ would be < (n-1) (with polynomial degree (n-1) there is a direct correspondence between the number of knowns and unknowns)

In our case, one has to consider the non-linear effect due to field curvature within the field of view of the camera CCD-lens system. According to Figure 6.4 an indicator could be the numerical aperture object (N.A.$_{object}$).

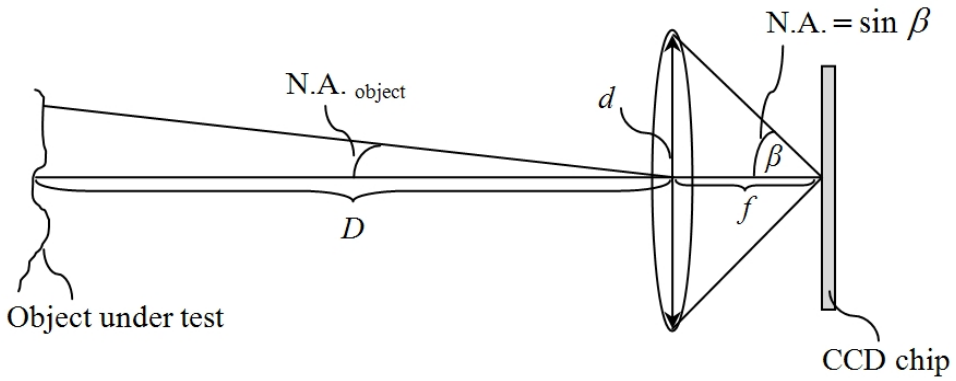

Figure 6.4: Showing the basic concept of N.A. $_{object}$ compared to N.A. of an optical system

In theory, a low value indicates that the field curvature is small compared to the field of view (typically, 16.3 × 12.2 mm, in our measurements). On the basis of the distance between the object under test to the lens, *D* (in previous Figure 6.4) then the current value for the N.A.$_{object}$ has been evaluated. As the largest lateral dimension of the field of view is about 16.3 mm and the distance from the object to the lens is about 210 mm then the expected value is about 0.04, i.e. the angle subtended by the object with the optical axis of the lens is about 2 degrees only. Similar optical setups in the literature have operated with similar values (for example, previous **[73]**) and it confirms that a low order polynomial fit (second-third degree) would be appropriate for calibration purpose. In the light of these considerations, the calibration procedure is shown schematically in Figure 6.5.

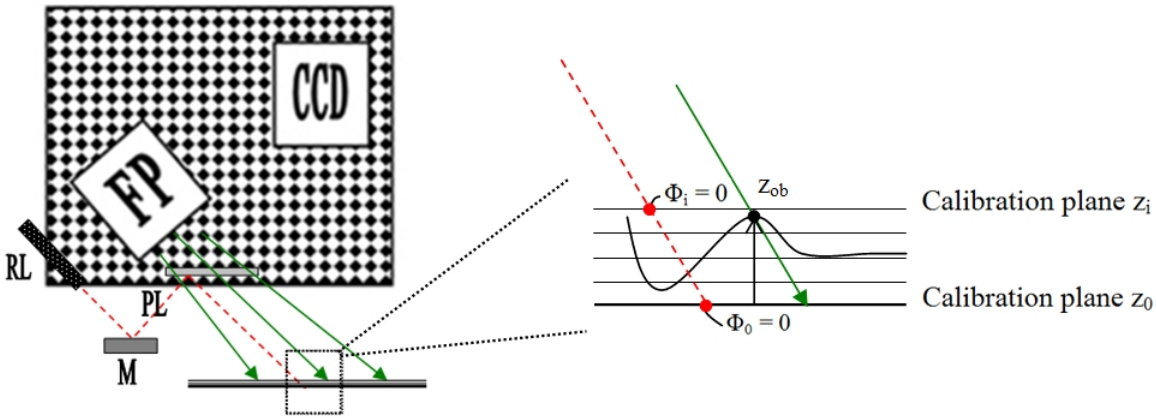

Figure 6.5: Calibration procedure. Parallel planes of equal height are used in order to define the relationship between phase distribution and height of the object under test. RL is the red laser spot projector. The reference laser is brought to be co-linear with the fringes via a pellicle (PL, see Fig. 6.6 for details) and a mirror (M). Image not to scale.

According to Figure 6.5 the calibration procedure needs several phase map planes (parallel planes) corresponding to the number of chosen height positions. In order to identify the 0^{th}-order fringe in each calibration plane it has been chosen to employ a second collimated beam (RL) parallel to one of the projected fringes. The projected spot has to be aligned with that fringe during the calibration process.

Therefore adopting a pellicle beam splitter proved to be a versatile and elegant solution: the red laser beam travels parallel to one of the projected fringes while the beam intensity of the projected fringes is transmitted almost unaltered (Figure 6.6).

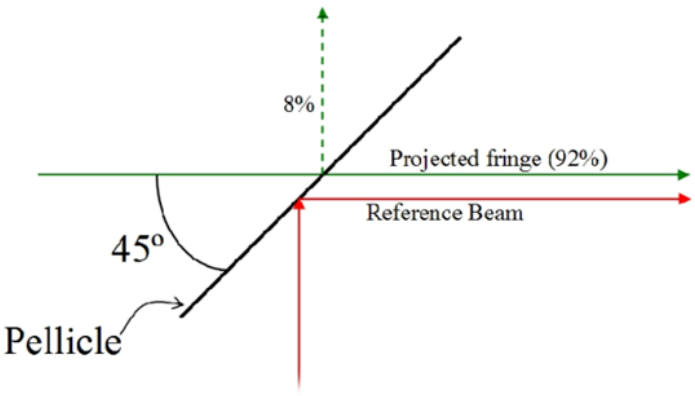

Figure 6.6: Diagram of pellicle (a very fine, 2 μm thick membrane) beam splitter operation

In addition the pellicle is adjustable for height and rotation.

Therefore, in the experimental setup six positions of the calibration plane are used (i.e. Z_n with n = 0, 1...5) where the position of the laser spot is well known.
Indeed, at each calibration plane, an unwrapped phase map can be calculated by capturing the projected fringe pattern as a sequence of four images with a phase shift of 90 degrees. On the basis of surface continuity the unwrapped phase maps have been generated by means of a suitable spatial phase unwrapping algorithm[2] **[96, 97]**. The gradients expected mean that the fringe patterns will be sufficiently contiguous that a spatial unwrapping algorithm is appropriate.

Directly afterwards, the information about the laser spot position is collected into a fifth image (Figure 6.7). The total data capture time, for the 5 images, ranges from 300 ms up to 420 ms according to the exposure time (10-40 ms).

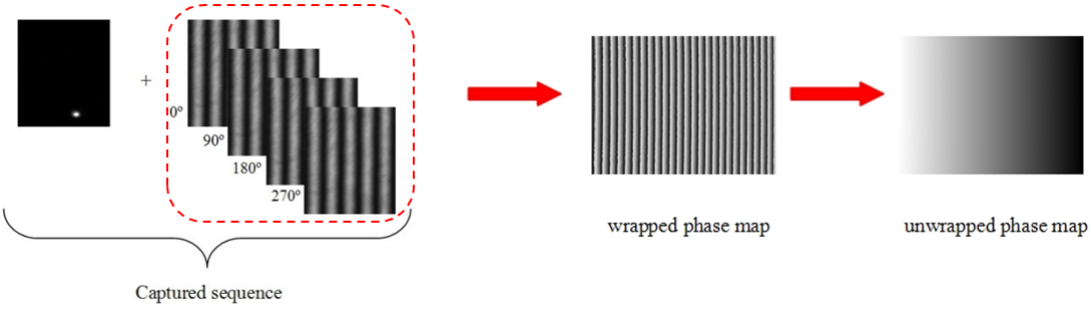

Figure 6.7: Image acquisition (left): projected spot location and phase stepped images. The Fringe Analysis (right) is applied to the four images phase-stepped by π/2 rad.

It is interesting to note that the presence of the projected spot introduces a (local) error in the height. For example, a lack of data information at the spot location is shown in the Figure 6.8.

([2]) *TWIG* by C.E. & D.P. Towers. 32bit edition, Alpha test v.0.01, March 1996 **[97]**

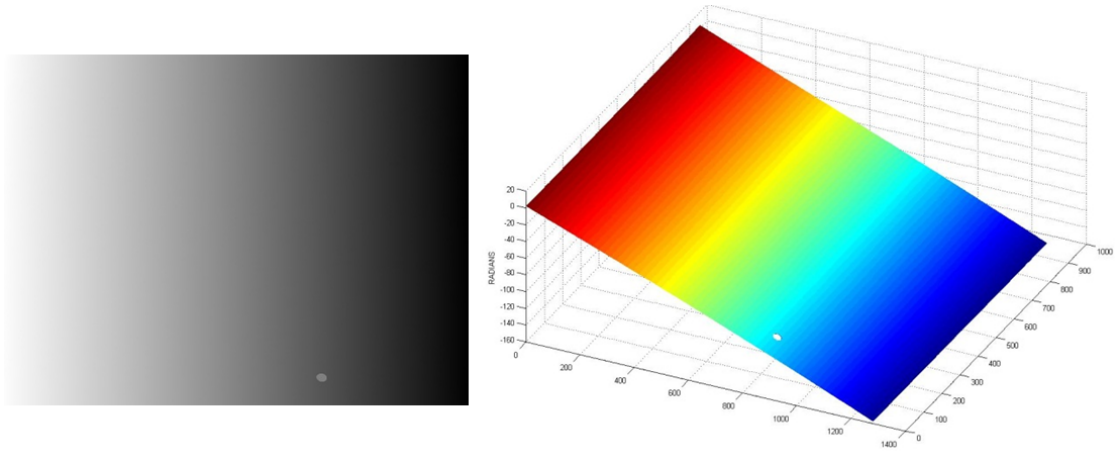

Figure 6.8: (Left) The projected spot on the unwrapped phase map. (Right) 3-D Matlab data representation showing the lack of data information right by to the spot location.

It is therefore necessary to record the projected fringes and the reference spots (one for every single calibration plane) sequentially in different frames.
The solution adopted consists of implementing a transistor as an electronic switch driven by a LabView code written *ad hoc* for this application (Figure 6.9).

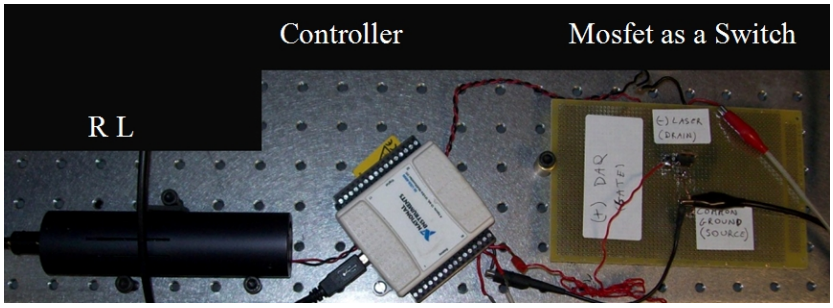

Figure 6.9: MOSFET transistor as a switch (ON/OFF) to control the Red Laser spot projector (RL)

Experimentally, the 6 positions of the calibration plane (with the location of any of the spot locations too) have been reconstructed adopting an open-top vessel filled up with Rhodamine B Chloride (at the saturation concentration) dissolved in ethanol.
Therefore, the set of above unwrapped phase maps (previous Fig. 6.7) constitutes input to a Matlab algorithm, employed to calculate either a 2^{nd} or 3^{rd} order polynomial fitting to provide a phase-to-height relation at each pixel (x, y) within the field of view.

In mathematical terms, the relation can be expressed as (the (x, y) dependence has been dropped for clarity):

$$z = a_0 + a_1 \cdot \varphi + a_2 \cdot \varphi^2$$

where φ is the (unwrapped) phase difference given by

$$\varphi(x, y) = \varphi_m(x, y) - \varphi_{m,cm}$$

with $\varphi_m(x, y)$ being the measured unwrapped phase map unwrapped from some arbitrary *(x,y)* point and $\varphi_{m,cm}$ is the value of the above unwrapped phase map calculated at the centre of mass of the corresponding reference laser location (the red spots in the previous Figure 6.5). Due to the small height changes being determined it is necessary to determine the reference spot location to sub-pixel resolution via a centre of mass calculation. The corresponding value of the unwrapped phase, $\varphi_{m,cm}$, is obtained by linear interpolation. The calibration is performed using a set of 6 measured unwrapped phases at known heights (*z* positions), z_i, and the corresponding $\varphi_i(x, y)$ unwrapped phases after subtraction of the phase at the reference spot location. This approach avoids making use of a fixed reference plane (for example, artificially generated). The coefficients a_0, a_1, a_2 (and a_3 in case of a 3rd order polynomial) have been generated by the *polyfit* function in Matlab (doing a fit between the set of known *z* positions and the unwrapped phase, in a least squares sense).

Therefore, the Matlab *polyval* function returns the value of a polynomial of degree either two or three evaluated at each pixel (x, y) of the unwrapped phase φ (with $i = 0, 1, \ldots, 6$).

It is important to remember that the polynomial coefficients a_0, a_1, a_2, are calculated independently at each pixel (x, y). In other terms, the above coefficients can be written as

$$a_i(x, y) \qquad \textit{with } i = 0, \ldots, 2 \;\; \& \;\; \forall (x, y) \in \textit{field of view}$$

covering the all field of view of the CCD camera (1280 × 960 pixels).

The following 3D Matlab plot (Figure 6.10) depicts the six reconstructed planes used for calibration purposes. The calibration volume dimension is approximately 250 microns deep (each plane is separated by about 50 microns from the next one).

The use of a fluid for the calibration surfaces ensures that the object is flat and care was taken to make sure that the measured region was sufficiently far from the edges of the vessel that surface tension effects were negligible (i.e. adhesion of fluid to the walls of the vessel results in a meniscus which turns upward at the edges of the vessel). A micropipettor was used to remove fluid from the vessel to generate each calibration surface and modify the z_i value. The solvent evaporates with time and would produce some considerable uncertainty in the height change between calibration planes. Therefore, the reference laser spot was used to determine the height change between calibration planes based on a previous measurement of the angle of the laser spot with respect to the calibration fluid surface and measurement of the *(x, y)* image scale.

The standard deviation (STD) for each plane is shown in Figures 6.11. As each reconstructed plane can be represented as a matrix (1280 × 960 pixels), the Matlab function **[98]** called *std* returns a row vector containing the standard deviation of the elements of each column of the matrix (by comparing the resolution achieved to 1 standard deviation one expects 68.2% of all individual measurements will fall within one standard deviation of the mean **[99]**).

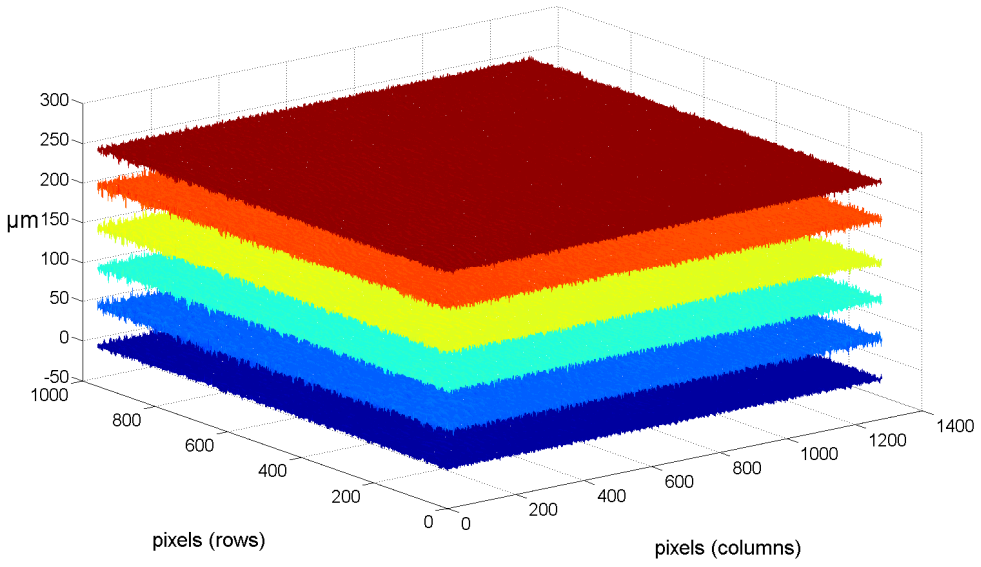

Figure 6.10: Reconstructed planes of calibration (z-scale in microns)

An independent measurement at another height *z* was not obtained and hence the noise analysis is conducted using the unwrapped phases from the calibration planes and hence the noise levels are not equal for each plane as would otherwise be expected.

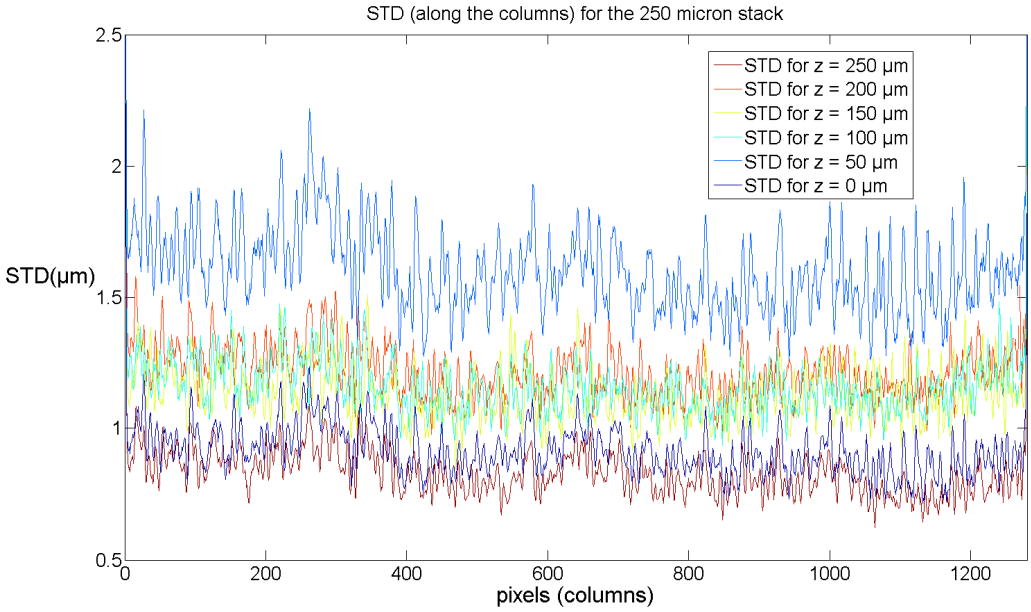

Figure 6.11: Standard deviation (STD, in microns) for the previous planes of calibration. The really low standard deviation (less than two microns, for each plane) indicates that the data set tends to be very close to mean.

In particular, the average standard deviation for the six calibration planes is plotted in the next Figure 6.12 (as usual the Matlab function called *std* returns a row vector containing the standard deviation of the elements of each column of the matrix). From simulations of the fitting process using artificial data, the average standard deviation noise over each plane is representative of the noise determined by an independent measurement.

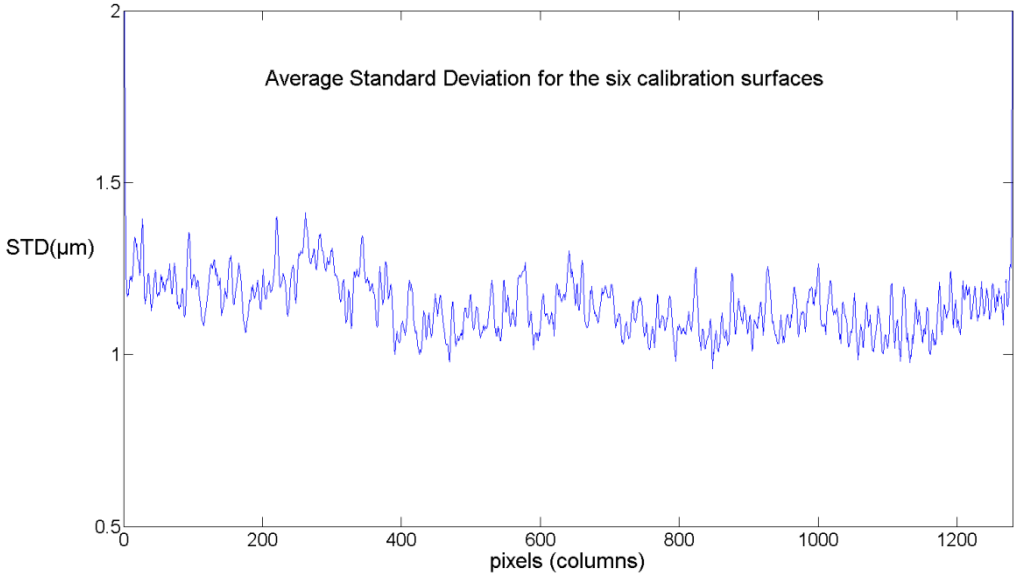

Figure 6.12: The average standard deviation (for the six calibration planes) is less than 2 microns

Hence, the standard deviation of the measured calibration depth is less than 2 microns across a field of view of about 16.3 × 12.2 mm.

The initial idea has been confirmed experimentally: order two polynomial trend lines give an accurate height mapping for these studies.

Indeed, tests with a third order polynomial fit don't seem to improve the accuracy (the average standard deviation, for the six calibration planes, results to be more than 3 microns). Moreover, the polynomial fit results are badly conditioned.

6.2 *Summary*

The calibration process involves a sequence of steps needed to relate the phase distribution (i.e. the modulated projected fringe pattern) to the height of the object under test. The approach followed in this chapter makes use of a set of six measured unwrapped phases at known heights and their corresponding unwrapped phases after subtraction of the phase at the reference spot location. Experimentally, the six positions of the calibration plane have been reconstructed by means of an open-top vessel filled up with a saturated solution of Rhodamine B Chloride and ethanol (according to the results achieved in the previous chapters 4 & 5 about the dye performance in terms of penetration depth and light intensity of emission as a function of concentration and solvent). This approach avoids the need to use a fixed reference plane. The final result translates into a low order polynomial fit (in a least squares sense) yielding a relationship between phase to height at each pixel (x, y) of the image. The average standard deviation, for the six calibration planes, results to be less than 2 microns. The effectiveness of the described procedure is demonstrated by experimental results that are provided in the next chapter.

Chapter references

[91] CREATH K (1988). Phase measurement interferometry techniques. *In*: WOLF E, ed. Progress in Optics, New York: Elsevier, 349-383.

[92] SALDNER HO and HUNTLEY JM (1997). Profilometry using temporal phase unwrapping and a spatial light modulator-based fringe projector. *Opt. Eng.* **36**(2), 610-615.

[93] THE MATHWORKS, INC. Least Squares (February 15, 2008). Available from http://www.mathworks.co.uk/moler/leastsquares.pdf (Accessed: 27/05/2013).

[94] HULTQUIST PF (1988). Numerical methods for engineers and computer scientists. Menlo Park, Calif.: Benjamin/Cummings Pub. Co. (ISBN: 080534652X).

[95] Optical Aberrations. Understanding the causes of aberrations in optical systems. Available from http://starizona.com/acb/basics/equip_optics101_curvature.aspx (Accessed: 27/05/2013).

[96] GHIGLIA DC and PRITT MD (1998). Two-dimensional phase unwrapping. New York: Wiley and Sons (ISBN: 0471249351).

[97] TOWERS DP, JUDGE TR, and BRYANSTON-CROSS PJ (1991). Automatic Interferogram Analysis Techniques Applied to Quasi Heterodyne Holography and ESPI. *Optics and Lasers in Engineering, special issue on Fringe Pattern Analysis* **14**, 239-281.

[98] THE MATHWORKS, INC. (2013). Standard deviation. Available from http://www.mathworks.co.uk/help/matlab/ref/std.html (Accessed: 27/05/2013).

[99] FREEDMAN D, PISANI R, and PURVES R (1997). Statistics. New York: Norton, W.W. (ISBN: 039397121X).

Part III

Experiments and Results

Chapter 7

Experiments on static fluids

The purpose of this chapter is to present the results from some experiments on static fluids in order to familiarize with fringe projection using fluorescent dye solutions (Section 7.1) and, at the same time, focusing attention on the study of this kind of fluids in the static condition by means of the phase stepping technique (Section 7.2). Further, the aim of this investigation is twofold: (a) to gather experimental data with a suitable dye-solvent solution in order to generate a stable fluorescence emission, under laser stimulation, for measurements which depend on the thickness of the film (Section 7.1), and (b) to investigate the outer geometry of static fluid films by means of the best dye-solvent combination in terms of light absorption-emission intensity (previous Chapter 4) with the phase-height relationship described in Chapter 6.

7.1 *Twin fibre system*

The following experiment has been performed in order to evaluate the ability of the twin fibre system, in combination with a fluorescent solution, to combine phase resolution, fringe stability and good sensitivity of the CCD camera (in the green and orange). Indeed, a practical system can be constructed using the twin fibre system and a dye with an emission wavelength close to the peak sensitivity of the CCD camera (Figure 7.1).

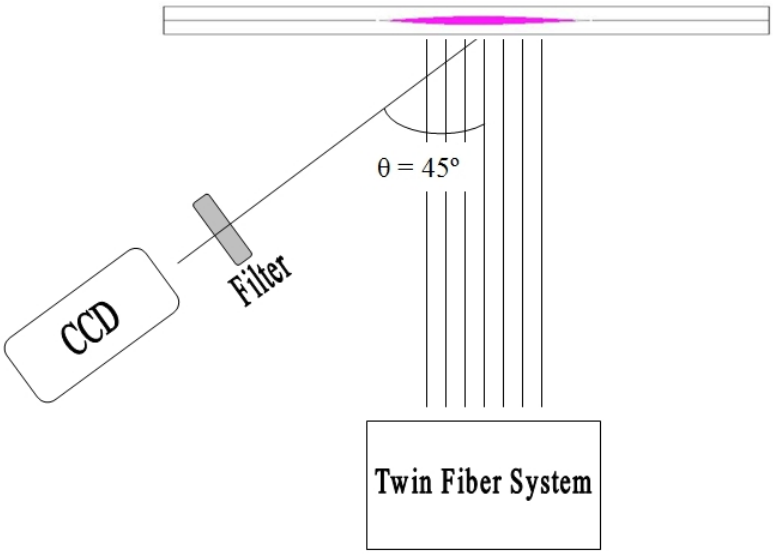

Figure 7.1: The practical system architecture proposed is based on the twin fibre system, CCD camera with good sensitivity in the orange (600-620nm) which corresponds to the emission wavelength of the typical fluorescent dyes, a filter in order to block the 532 nm excitation and only capture the fluorescence, and a pair of microscope slides (top of this image) containing the dye in the middle (not to scale). The microscope slide has a round convex cavity in the centre. The angle (θ) between the CCD camera and the twin fibre system can be modified (between 0º and 45º) in order to accentuate the object shape by projecting the fringe pattern.

In order to develop this experiment it was decided to use, according to the results gained at end of Chapter 4 (see previous Figure 4.13), a solvent-dye combination showing a good fluorescence emission intensity at concentrations lower than the saturation point (i.e. the concentration has to be sufficient to generate a detectable stimulated fluorescence emission inside the convex concavity of the two microscope slides) and with a low evaporation rate (such as to be easily encapsulated into the microscope slide structure, Fig. 7.1 and 7.2). The dye used for this experiment is Sulforhodamine 640**,** a red fluorescent dye, known also “Texas red”. Texas Red

fluoresces at about 610 nm, and the peak of its absorption spectrum is at 578 nm (in ethanol), making it appear more purple than red in colour **[100]**.

Figure 7.2a shows a clear glass microscope slide with a single convex cavity in the centre used in this experiment. A sandwich structure (Figure 7.2b) of two microscope slides provides a cheap solution in which the dye can be excited by laser light with a frequency close to its excitation frequency. The overall structure is shown in Figure 7.2c.

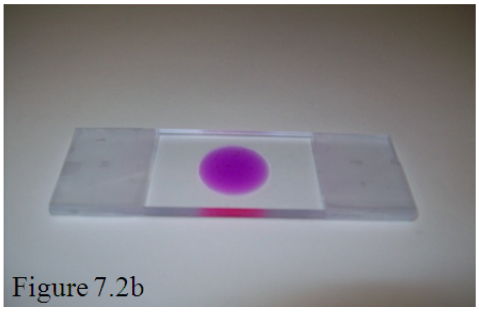

Figure 7.2a: Microscope slide with a single convex cavity (Ø approx. 15-18 mm, depth cavity approx. 0.6 to 0.8 mm, capacity approx. 0.1 to 0.2 ml, thickness approx. 1.2 to 1.5 mm, courtesy of Marienfeld Laboratory Glassware).

Figure 7.2b: A sandwich structure of two microscope slides with the dye solution in the middle

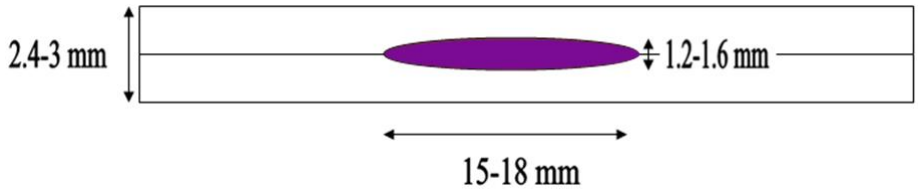

Figure 7.2c: Typical dimensions of the sandwich structure of two microscope slides (not to scale)

The choice of the solvent and dye concentration is a really critical step as seen in Chapter 4. For example, a very low concentration would not be enough to generate the photo-excitation of the fluorescent dye to give a detectable image. For measurement of the external surface profile of a fluid film a high dye concentration is needed such that the emitted light comes from the top layer of the surface. For measurements that will depend on the thickness of the film a lower dye concentration would be needed such that the laser light can pass through.

In this case the solution is made of pure water with a dye concentration of 10 mg per 100 ml of water, which corresponds to 1.5×10^{-4} Molar concentration (molar mass of 629.71 g/mol from Exciton data sheet **[101]**).

The following figure (Figure 7.3) indicates that the overall system works: it is possible to observe clearly defined fluorescent fringes with this medium level of dye concentration. The image was obtained via a filter to block the 532 nm excitation and only capture the fluorescence. The fringes are notable as they do not exhibit the typical ‘speckled’ appearance that is usually obtained with narrow linewidth laser sources, which is due to the bandwidth and lack of coherence of the fluorescence emission.

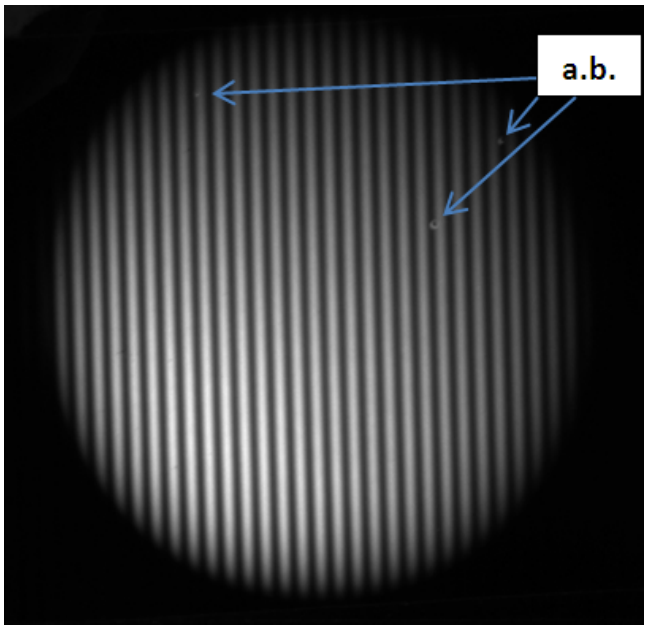

Figure 7.3: Fluorescent fringe pattern. About 20 fringes per cm, fringe separation ≈ 500μm (60 ms, exposure time). Normal incidence (θ = 0º). The three imperfections are tiny air bubbles (a.b.) trapped under the surface.

By knowing the number of projected fringes and the cavity diameter an estimate can be given of the fringe separation at the object (e.g. see previous Figure 7.3).
This last value is useful to get an estimate of the fringe depth from the camera if the projection angle is known (see Figure 5.1 and Figure 5.5, Chapter 5 for further details): in this experiment the angle was 45° with different fringe separations (e.g. see Figure 7.4a and Figure 7.4b).

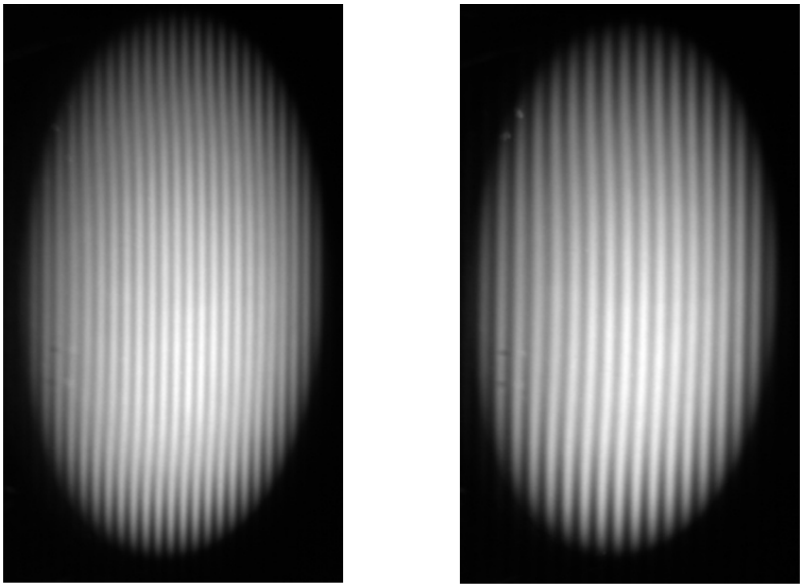

Fig. 7.4a: Fringe separation ≈ 700 µm, fringe depth from camera ≈ 990 µm (60 ms, θ = 45º)

Fig. 7.4b: Fringe separation ≈ 500 µm, fringe depth from camera ≈ 700 µm (60 ms, θ = 45º)

From a phase stepping analysis of these data (using 4 images at 90° phase steps) the standard deviation phase noise (as an average over three rows) was found to be 1/163 of a fringe (60 ms exposure time). The unwrapped phase along a row (around the centre of the image) shows a nonlinear behaviour (related to the sample shape) as the dye is inside the microscope slide convex cavity (Figure 7.5).

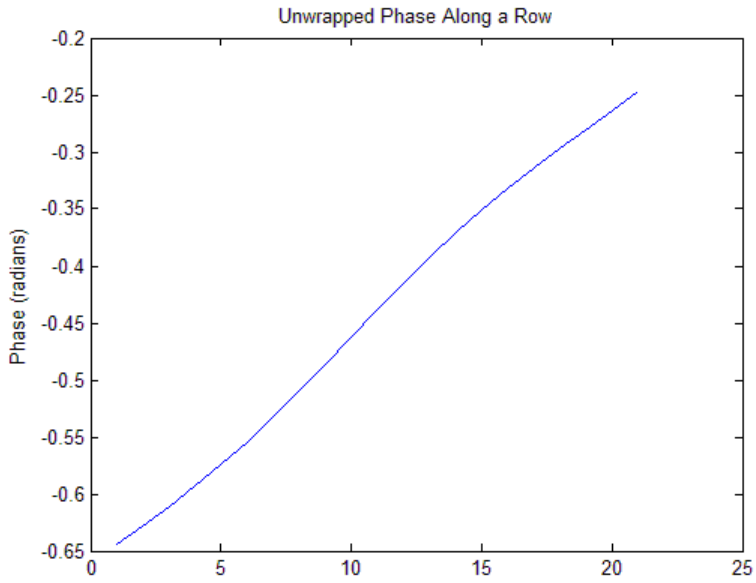

Figure 7.5: The unwrapped phase along a row brings out the non-flat surface

The convex cavity is clearly shown in Figure 7.6 and can be identified from the spatial deviation of the fringes from the edge of the cavity towards the centre. A variation in fringe contrast **[79]**, defined as $\frac{I_{max}-I_{min}}{I_{max}+I_{min}}$ where I_{max} and I_{min} are the maximum and minimum intensities that can be obtained at a point, is also observed at this medium level of dye concentration. Fringe contrast is high at the edge of the cavity where there is a low film thickness and appears to follow a periodic modulation as the film thickness increases towards the centre of the cavity.

Figure 7.6: The fringe pattern shows the presence of non-flat surface. The fringe separation is less than 500 µm. Lens 105mm f/2.8, 60 ms.

7.2 *Phase measurement profilometry*

The optical setup described in Chapter 5 has been adopted for the study of phase measurement profilometry. This solution provides a very flexible system: good phase resolution (twin fibre system), robustness against environmental disturbances (thermal enclosure) and software implementation (four-frame phase stepping). This last element will be the focus of this section. Phase-stepping methods provide the phase value at each image pixel independently. Hence, the presence of interrupted field of views (for example, apertures with holes inside) is less problematic than methods based on full image phase detection such as Fourier transformation **[102]**.

The aim of this method (4-Phase algorithm) is to determine the phase map from a set of phase stepped interferograms differing from each other by a known phase value (usually $\pi/2$ radians). The phase map (wrapped phase) contains phase gaps of 2π because of the principal value range of the arc tangent function.

These ambiguities can be eliminated by an algorithm called *phase unwrapping* which delivers a smooth (contiguous) phase map **[91]**.

In fringe projection profilometry, the technique based on phase stepping profilometry provides the 3-D profile of the measured object from the unwrapped phase of every single pixel **[103]**.

Therefore, the overall system described in Chapter 5 (Sections 5.2 & 5.3) has been employed to measure the thickness of static fluids within suitable containers (such as for the purpose of calibration) or the shape of fluids on discontinuous objects (topographies).

For example, one can consider an interferogram with a fringe pattern such as the one represented on Figure 7.7 (Field of view ≈ 8.3 × 6.2 mm; 20ms, exposure time).

Figure 7.7: Instantaneous interferogram (flow cell filled up with ethanol and Rhodamine B)

In this case, a clear glass flow cell has been filled up with a saturated solution made of Rhodamine B (Chloride) dissolved in ethanol.

Figure 7.8 shows the 4 phase shifted interferograms, obtained with phase steps of 0, $\pi/2$, π and $3\pi/2$ respectively (in a clockwise direction from top left). The limit of solubility[1] occurs at 48 mM.

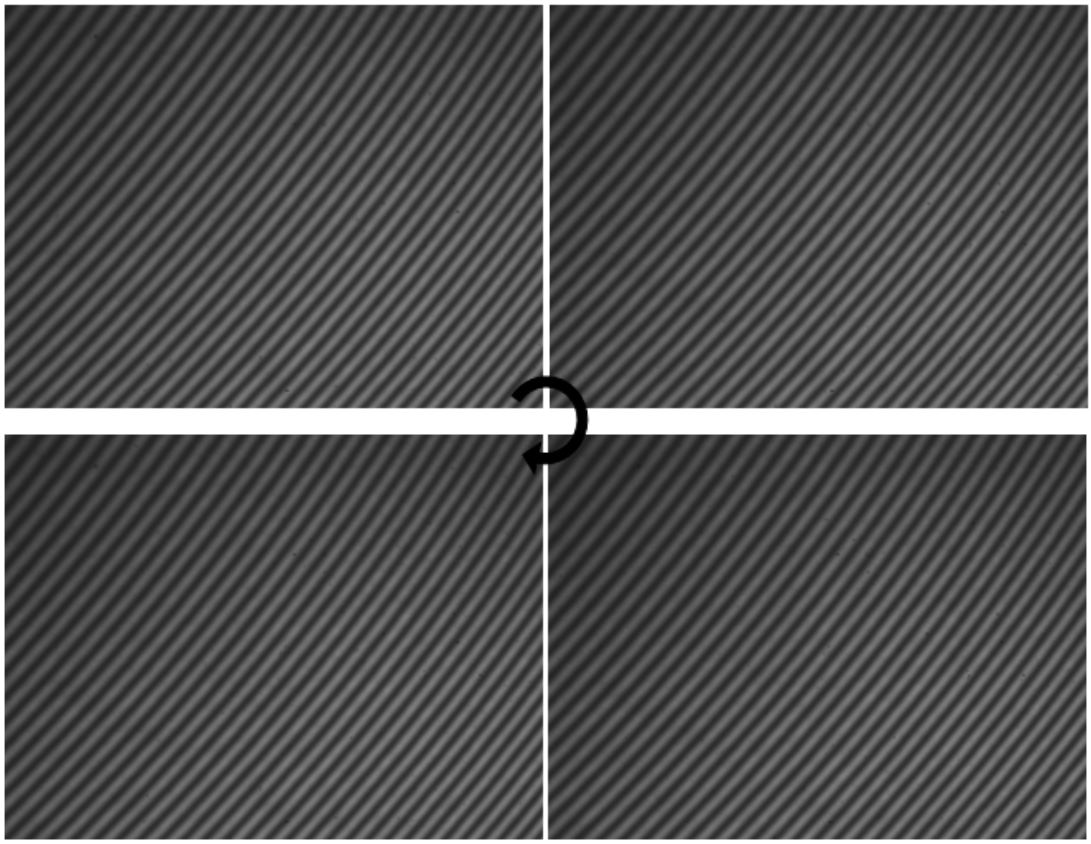

Figure 7.8: Phase shifted interferograms. The circular arrow indicates the direction of progressive increase of the phase step value ($\pi/2$).

([1]) It is the concentration of the saturated solution

As it has been seen previously (Chapter 2), the phase can be calculated using the following relation **[35]**:

$$\Phi(x,y) = arctan\left[\frac{(I_4 - I_2)}{(I_1 - I_3)}\right]$$

where I_1, I_2, I_3, I_4 are the intensity distribution of the interferogram with 0, π/2, π and 3π/2 radian phase shifts respectively and *arctan* is the inverse tangent function.
Figure 7.9 shows the results obtained after applying the algorithm to the 4-shifted interferograms.

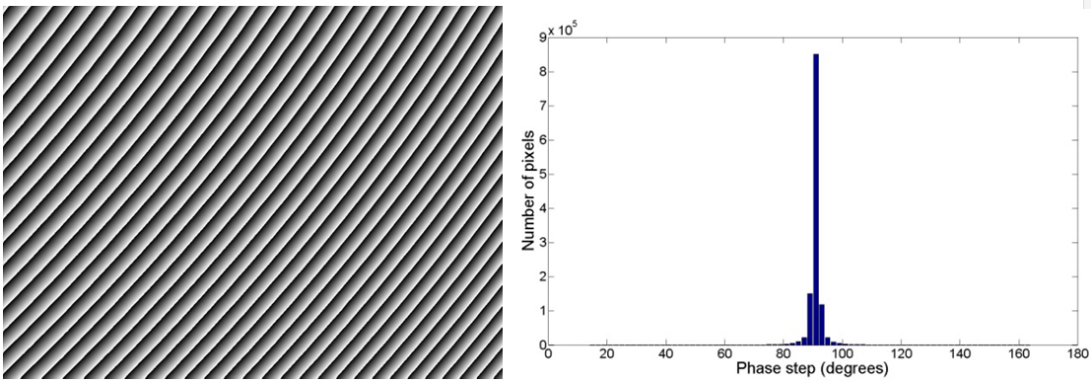

Figure 7.9: (left) Wrapped phase estimated using the 4 shifted interferograms.
(Right) Phase shift accuracy. The Matlab screenshot shows the phase shift distribution for the four stepped frames. Phase step centered at 90.947 degrees (see Eq. 5.5, Chapter 5, Section 5.3).

The phase is only obtained modulo 2π, thus producing the phase jumps observed on the figure **[104]**. A suitable spatial phase unwrapping algorithm[2] delivers the result shown on Figure 7.10.

([2]) *TWIG* by C.E. & D.P. Towers. 32bit edition, Alpha test v.0.01, March 1996 **[97]**

Figure 7.10: Unwrapped phase map (1280 × 960 pixels)

This process has been used to generate a smooth phase distribution (unwrapped phase) and thereby assess the phase noise level against a low (cubic) order polynomial fit.

Finally, one can take the standard deviation of the residual errors between the unwrapped phase and the fitted phase distributions as a measure of phase noise. This approach is similar to the one described in Chapter 5, Section 5.1.3.

One can examine three rows across the unwrapped phase map (selected at 1/4, 1/2 and 3/4 of the height of the phase map). The variations are expected to be because of fringe modulation (and therefore illumination) differences across the image.

The following results were obtained (Table 7.1).

	Rows across the unwrapped phase map selected at 1/4, 1/2 and 3/4 of the height of the phase map			
	1/4	1/2	3/4	Average of 3 rows
Standard deviation phase noise as fraction of a fringe	**1/205**	**1/221**	**1/243**	**1/223**
Standard deviation phase noise in radians	**0.031**	**0.028**	**0.026**	**0.028**

Table 7.1: Standard deviation of the residual errors between the unwrapped phase (see Fig 7.10) and the fitted phase distributions as a measure of phase noise. Three rows across the unwrapped phase map (selected at 1/4, 1/2 and 3/4 of the height of the phase map) have been examined. The results are both shown as a fraction of a fringe and in radians (fringe separation ≈ 250 μm).

Therefore, the standard deviation phase noise (as average of three rows) is 1/223 of a fringe (20 ms, exposure time).

In the light of the considerations developed in Chapter 6, one needs the system to be calibrated in order to get an analytical relationship between height and phase.
Indeed, according to the results achieved in Chapter 4, a saturated solution of Rhodamine B Chloride in ethanol is the best candidate for the investigation of external surface profile of a fluid film because the emitted light comes from the top layer of the surface (≈ 5 microns). Figure 7.11 shows the fringe projector and the rig used for the study of static fluid films.

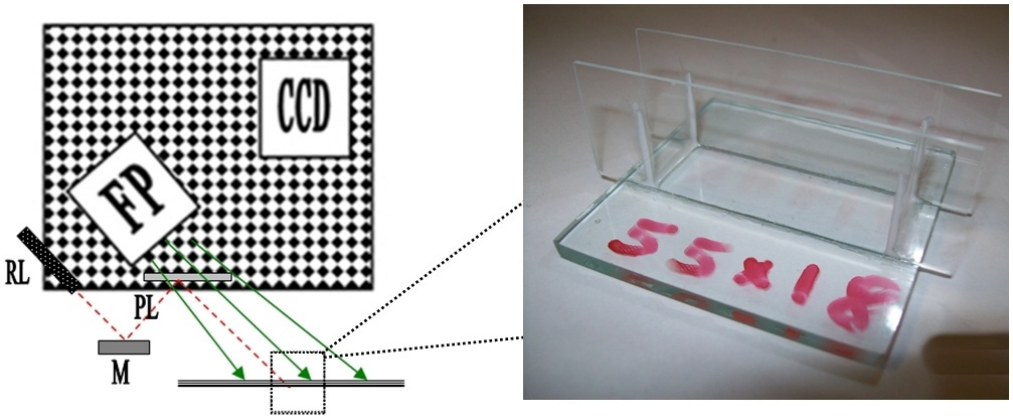

Figure 7.11: Fringe projector (FP) block and rig (open-top vessel) used in the present study (image not to scale, see previous Figure 6.5, Chapter 6, for details).

After the system was calibrated, it was tested first by measuring the shape of the (liquid) planes at arbitrary *z* values within the open-top vessel used for calibration (Figure 7.12a).

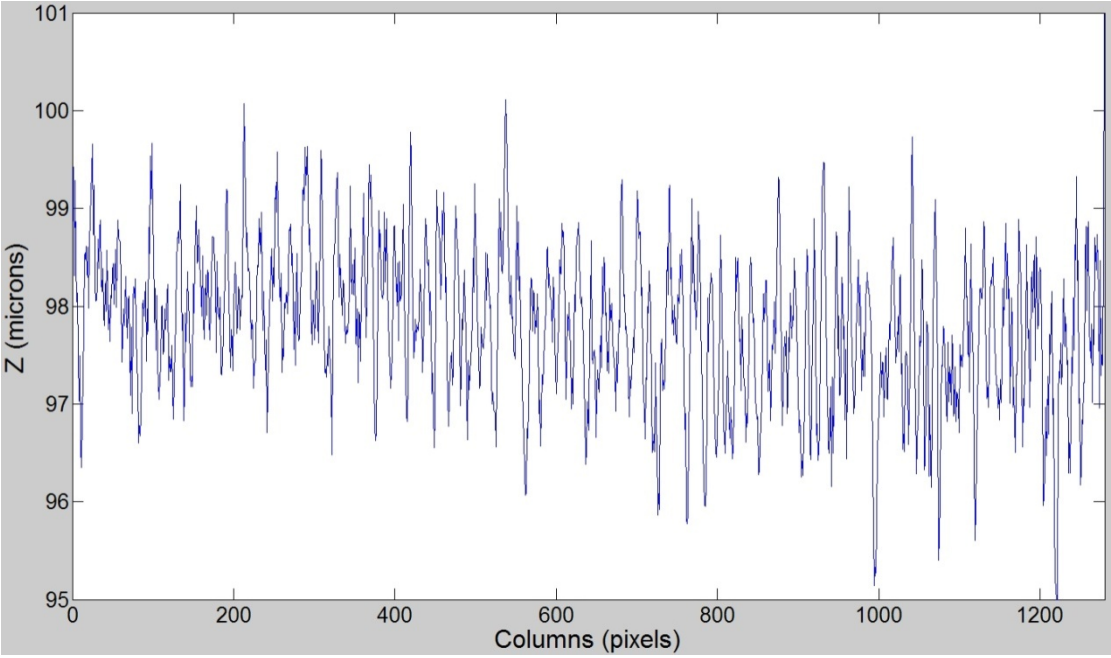

Figure 7.12a: Cross section of a measured profile of a (liquid) surface, positioned at z = 98 microns

The standard deviation (compared to a cubic fit) is illustrated in the Figure 7.12b. The actual field of view is about 16.3 × 12.2 mm (1280 × 960 pixels).

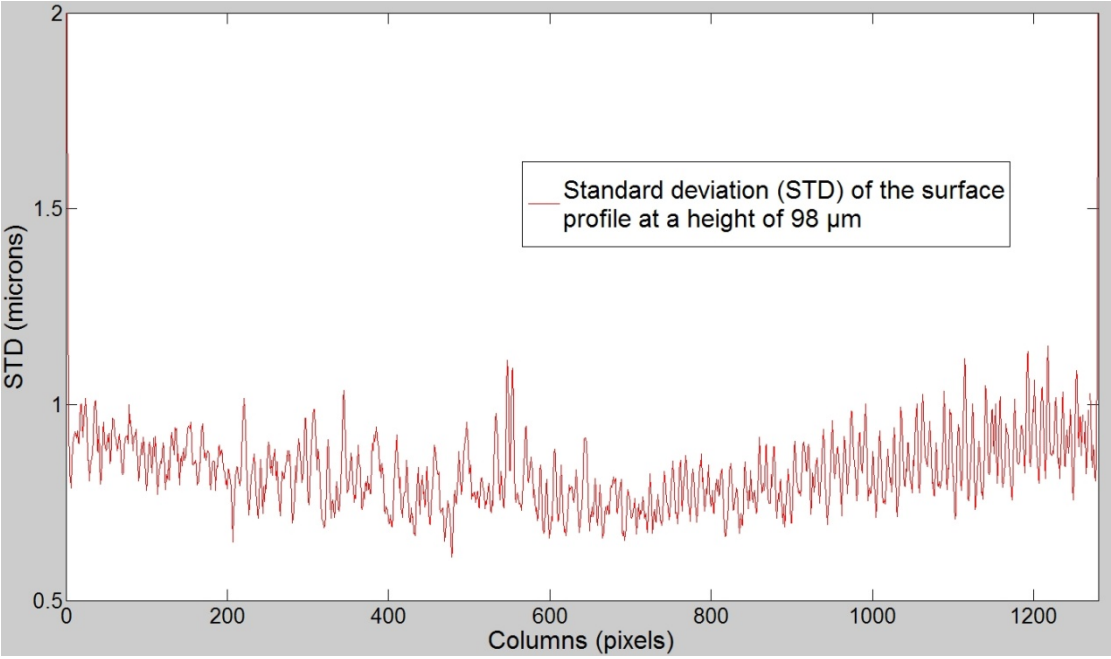

Figure 7.12b: The standard deviation (STD) for the previous surface profile. The low standard deviation (less than one micron) indicates that the data set tends to be very close to mean.

The overall shape of the curve (lower in the middle than at the edges) is probably due to higher intensities at the middle and hence better phase resolution.

However, the standard deviation of the surface profile is calculated as 0.83 µm, which is about 1/250 of the depth of the measurement volume (200 µm).

For reasons of clarity, the standard deviation values have been plotted along the columns of the image only.

The following example (Figure 7.13) illustrates the case of a system including a flow cell (filled up with a solution of Rhodamine B and ethanol, 48 mM) and a 100µm thick blade of a feeler gauge. Images were obtained from the top of the dye solution in the flow cell both with and without the feeler gauge placed underneath the cell to give a known height change.

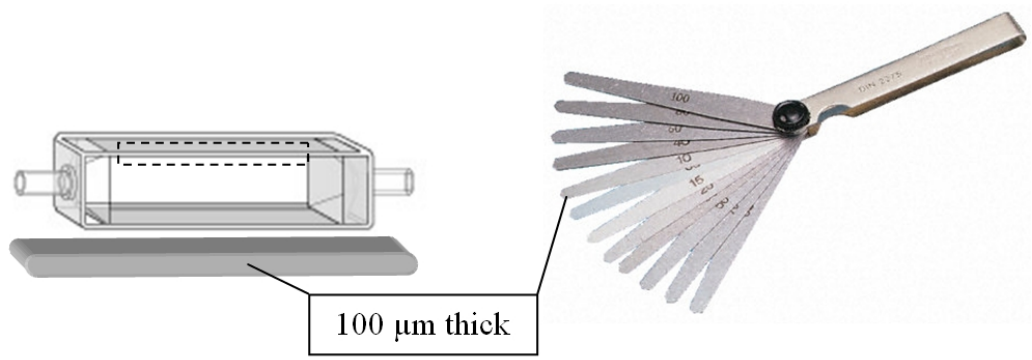

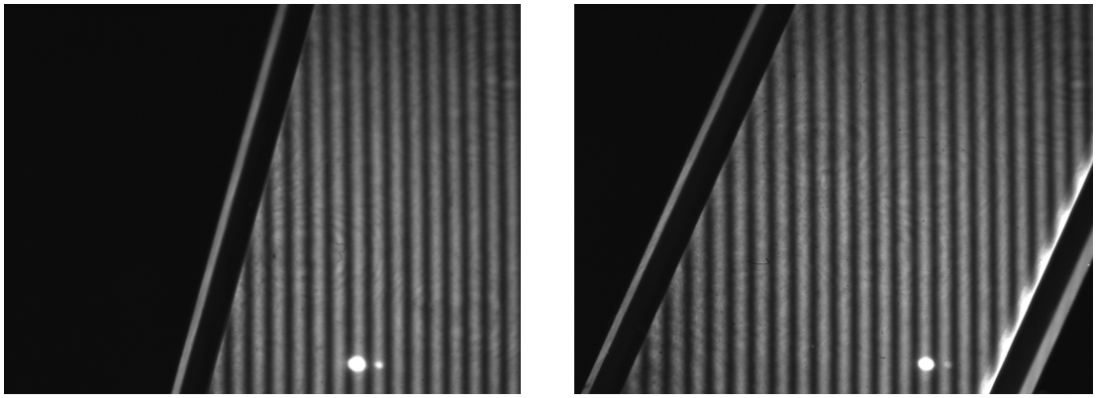

Figure 7.13: (Top) Schematic showing the clear glass flow cell and the 100 µm thick blade, from a calibrated feeler gauge[3], used for the thickness measurement. The dashed area is the sample area. (Bottom) The laboratory images (top view) show the flow cell with (left) and without (right) the 100 micron thickness. The projected fringes, generated from fluorescence emission, select the measurement area of the flow cell. For reasons of clarity, the bright spot of the laser spot projector has been included into the images. This reference laser spot is introduced to give an absolute zero in the unwrapped phase. The field of view is about 16 × 12 mm.

It would be interesting to notice that missing-data do not affect the rest of the image because the phase-stepping method calculates the phase value of each image pixel independently (Figure 7.14).

([3]) Courtesy of RS Components

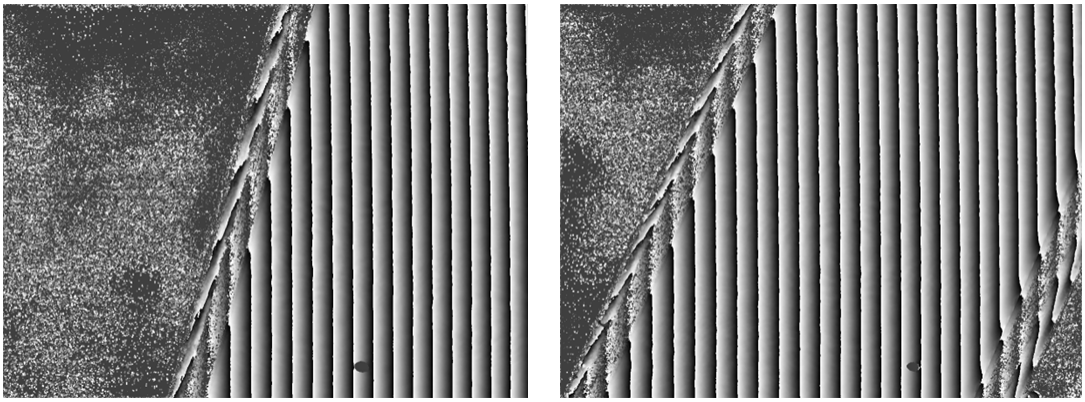

Figure 7.14: (left) Wrapped phase map in presence of the 100 µm metal thickness and without (right). The sample area is detected by the area where the intensity is modulated (the fringe pattern is visible in the two images).

By knowing the unwrapped phase to height relationship from the calibration height range (0-200 µm) the expected height difference, between the two measurements with and without the feeler gauge, can be reconstructed starting from the unwrapped phase maps.

The following images (Figures 7.15a & 7.15b) show the unwrapped phase maps for the sample areas.

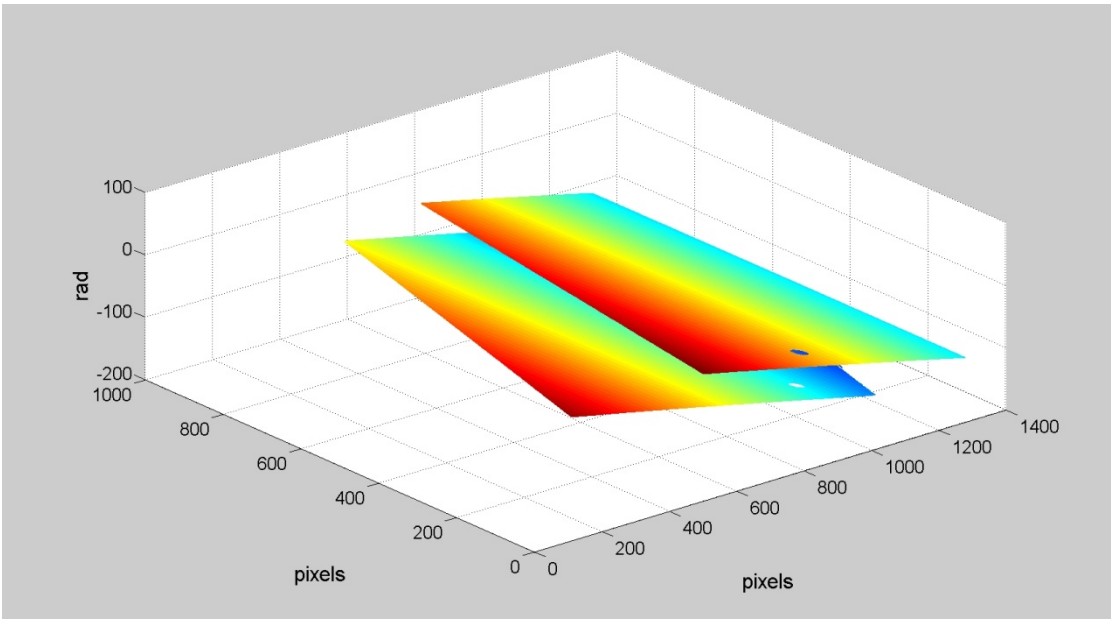

Figure 7.15a: A Matlab visualization of the two unwrapped phase maps. The two surfaces (planes) show the reliable data within the whole field of view.

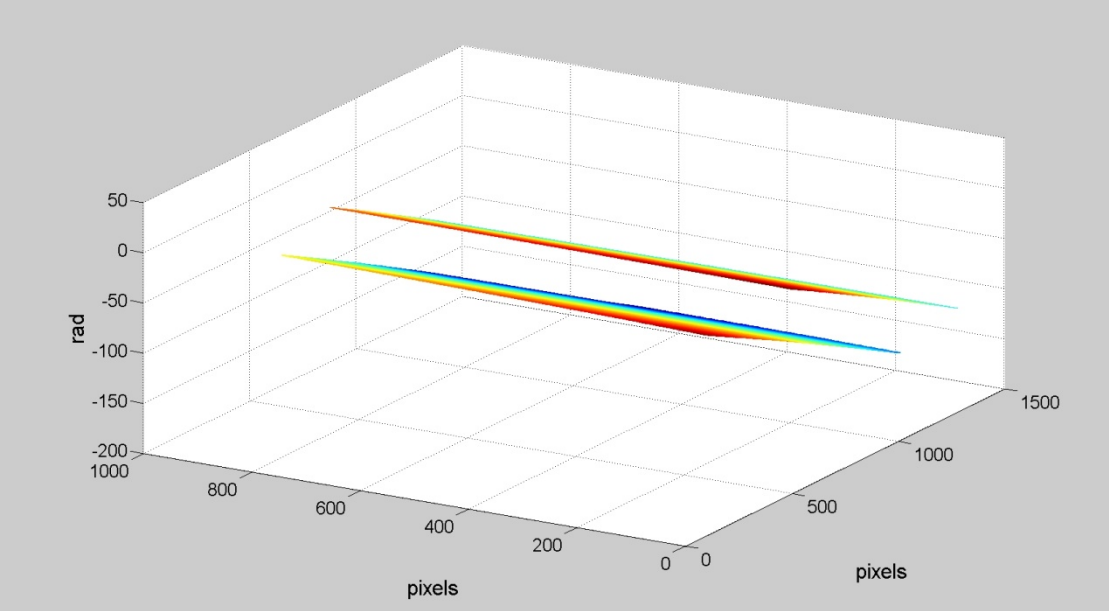

Figure 7.15b: Cross-section of the two unwrapped phase maps

Figure 7.16 depicts the relative distance between the two planes. The cross section has been taken considering the same row, within the phase maps, for both the planes.

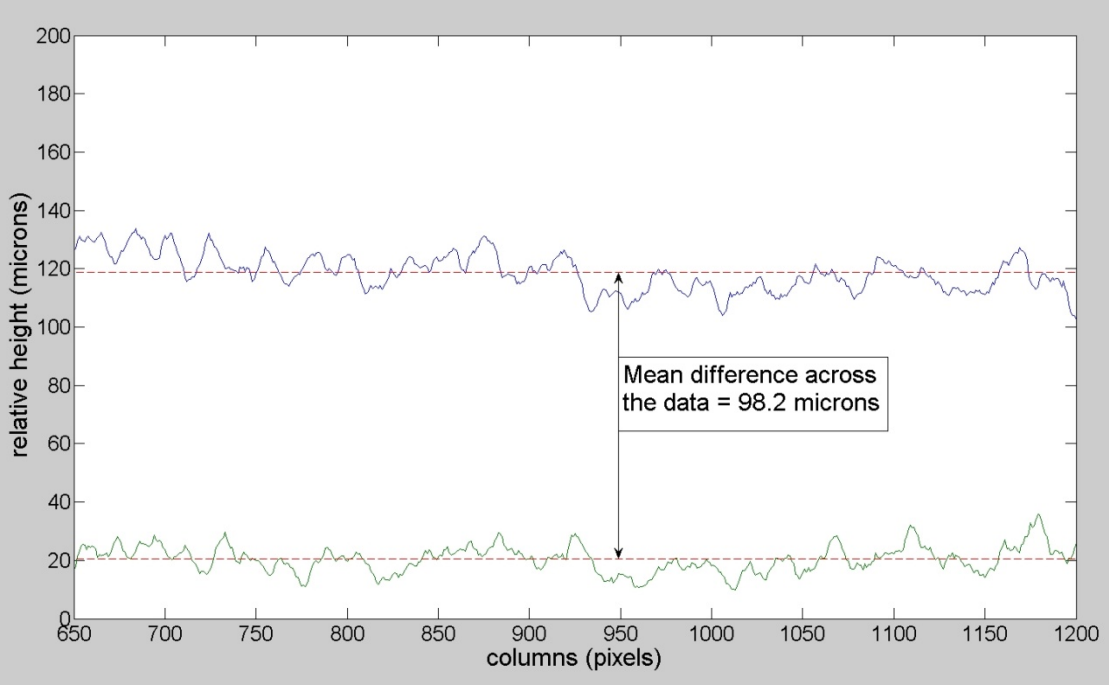

Figure 7.16: Cross section of the two measured profiles. The mean difference across the data (z-distance between the two planes) is 98.2 microns. This value is in good agreement with the nominal thickness used for the experiment (100 ± 2 μm).

It is quite likely that inserting the feeler gauge will not give exactly the height difference expected due to the flow cell not sitting back down exactly in the same way.

7.3 *Summary*

This chapter has described some results of the technique developed for the case of experiments involving static liquids. On the basis of calibration results, the proposed measurement system (based on the twin fibre configuration) has been applied for the shape measurement of some static fluids. Some experiments have been carried out using the best dye solution in terms of fluorescence emission and light depth penetration (a saturated solution of Rhodamine B dissolved in Ethanol as discussed in Chapter 4). The profile of the exterior surface of these fluids has been investigated by means of the phase-stepping technique and the phase-height relationship. The resolution achieved is less than 2 microns (to 1 standard deviation) which is sufficient for the thin films to be considered in this project.

In addition, the experimental data demonstrated the ability of this methodology to measure fluids with micron resolution over a field of view larger than 10 × 10 mm (16.3 × 12.2 mm in the previous images).

In the light of these results, the technique will be employed for the investigation of thin fluid films (100-300 μm) flowing over an inclined plate with topography (see the next Chapter 8).

Chapter references

[100] PHOTONIC SOLUTIONS Ltd. Laser Dye Properties. Available from http://www.photonicsolutions.co.uk/dyeinfo.asp# (Accessed: 27/05/2013).

[101] PHOTONIC SOLUTIONS Ltd. Sulforhodamine 640. Available from http://www.photonicsolutions.co.uk/datasheets/exci/Sulforhodamine%20640.pdf (Accessed: 27/05/2013).

[102] Blümel T. Knowledge Base: Phase Shifting. TRIOPTICS (14/08/2012). Available from http://www.trioptics-berlin.com/downloads/intern/formular_en.php (Accessed: 27/05/2013).

[103] XIAOLING Z, YUCHI L, MEIRONG Z, XIAOBING L et al. (2005). Calibration of a fringe projection profilometry system using virtual phase calibrating model planes. *J. Opt. A: Pure Appl. Opt.* **7**(192).

[104] PICART P (2010). Interference and fringe pattern demodulation (online courses, multiple authors). Available from http://www.optique-ingenieur.org/en/courses/OPI_ang_M02_C06/co/Grain_OPI_ang_M02_C06_1.html (Accessed: 27/05/2013).

Chapter 8

Experiments on thin film flowing fluids

The technique applied to the study of static thin fluids (Chapter 7) will be employed for the investigation of flowing thin fluids over an inclined plate with topography.
Several applications make use of thin films: from fabrication of coatings for displays to solar cell manufacture and for surface property modification (see Chapters 1&2).
In a number of cases the surface to be coated includes topographic features, required for the functionality of the device. These perturb the formation of the film and can create long lasting ripples over the surface **[105]**.
The aim of this chapter is to show the application of this method for applications involving dynamic fluids. In particular, a flow rig set-up was built in order to test the shape measurement system in the presence of real liquid flows (at different thickness) over topography of known geometry. In the following sections, firstly the description of the experimental setup will be introduced including the description of the optical and mechanical sections developed for the inclined flow rig. Secondly the experimental details of phase-stepped interferometry applied to the inclined plate set-up will be illustrated in light of the method developed so far (the use of fluorophores with laser based fringe projection). The main target of the dynamic experiments will be to show the metrology capability for thin fluid films over uneven topography (i.e. the profilometry of the outer geometry of the fluid with fringe projection) and provide a *qualitative* comparison of the fluid surface topography near the topographic feature as reported in literature for thin liquid films flowing over topography.

8.1 *Description of the experimental set-up*

The experimental set-up produces a gravity driven flow over an inclined plate with topography. The determination of the shape of the fluid film makes use of the phase-stepping technique (as described in Section 7.2, Chapter 7).

Figure 8.1 illustrates the overall system used for measurement and production of thin fluids films. The gravity-driven liquid flowing over the topography is collected at the end of the inclined plate. Consequently, the pump must be sized to maintain a stable flow rate by recycling the fluid to a reservoir. The relative height of the reservoir can be changed with respect to the inlet of the slit. Reservoir and slit inlet are connected via a flexible hose.

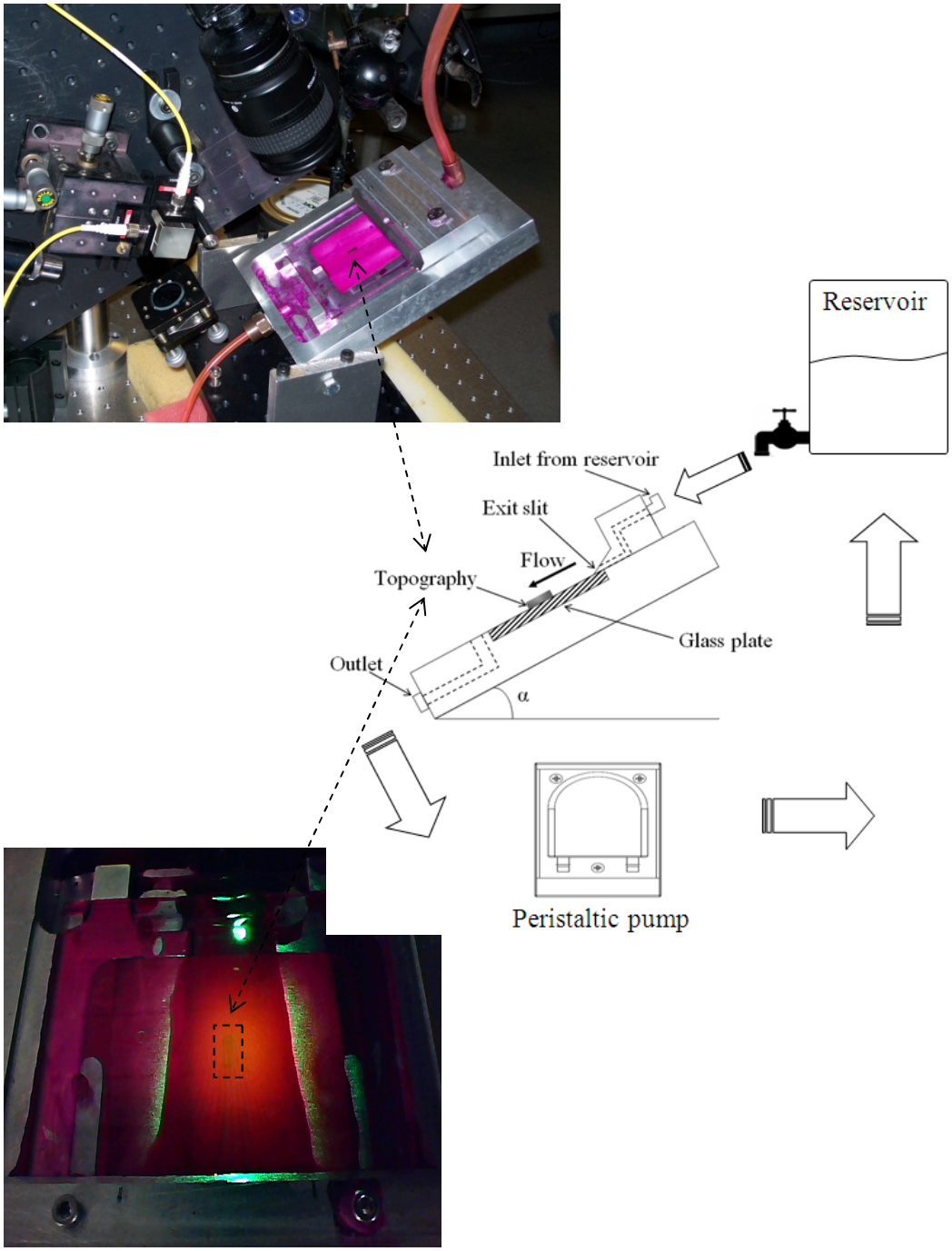

Figure 8.1: The practical flow rig set-up developed. (Top left) Physical realization showing the inclined plate with topography and the projector system (reservoir and drain are out of view);
The schematic (Middle) highlights the fundamental components of the system. The liquid flow can be controlled by changing the height of the reservoir and the angle the slit makes with the horizontal, α. The peristaltic pump has two roles: collecting the fluid from the exit and providing a stable flow rate. In addition, this kind of devices is ideal for experiments with dye solutions: the liquid being pumped never comes into contact with any moving parts because it is totally contained within the re-enforced hose.
(Bottom left) The top view shows the exit of slit with topography (60 µm thick) covered by real fluid.

The optical setup makes use of the same components adopted for the measurement of static fluid films (see also Chapter 7).

Hence, the optical part consists of the following main elements:

- 532 nm laser (green light) with 200 mW laser output power
- Monochrome Basler CCD camera (frames at 1280 × 960 pixels, 8-bit with pixels of 6.45 × 6.45 µm)
- 60 mm f/2.8 Macro Lens (Nikkor)
- Fringe projector (beam splitter and output fibres block)
- Red laser spot projector (to give an absolute zero in the unwrapped phase map)

As usual, the phase-stepping algorithm relies on a LabView code developed in order to drive a piezoelectric transducer with an appropriate voltage (see Section 5.3, Chapter 5 for further details). The new flow rig deserves to be described in detail. The following figures (Figure 8.2a & 8.2b) show the typical dimensions of the slit.

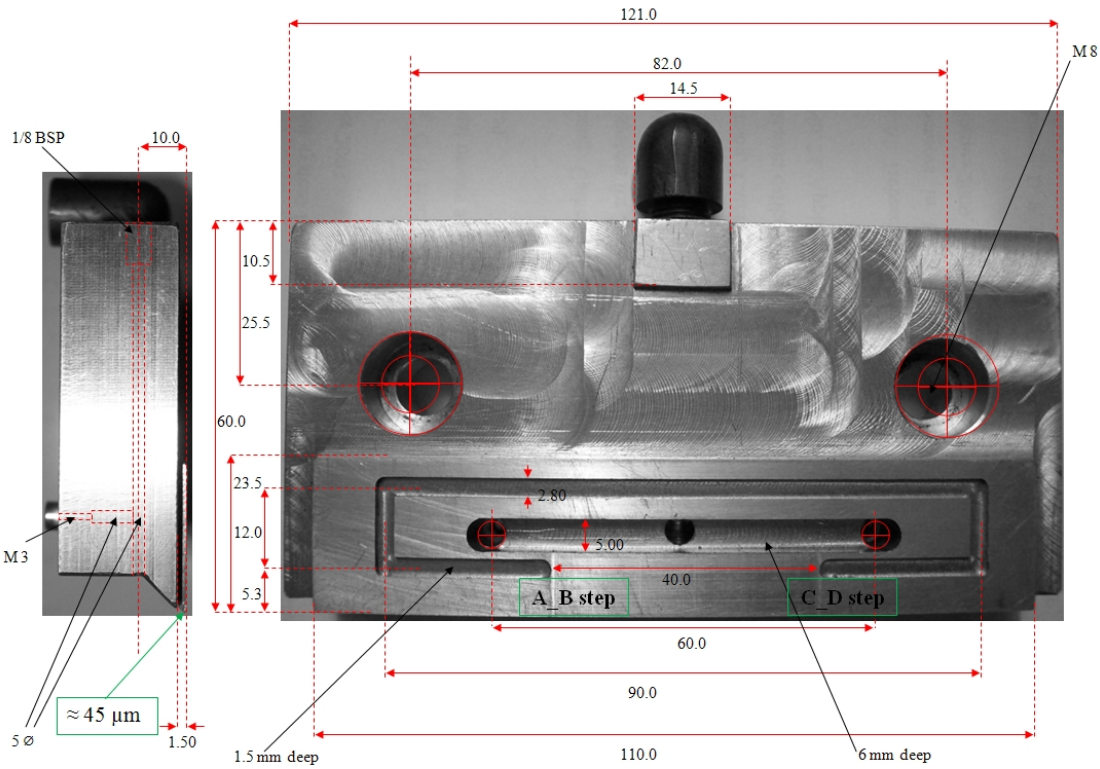

Figure 8.2a: (Left) Side view showing (in green) the height of the exit of feeding slit. (Right) This upside down view shows the lateral dimensions of feeding slit delimited by A_B and C_D steps (see Figure 8.1b for details). All dimensions are in millimetres (mm) unless otherwise specified.

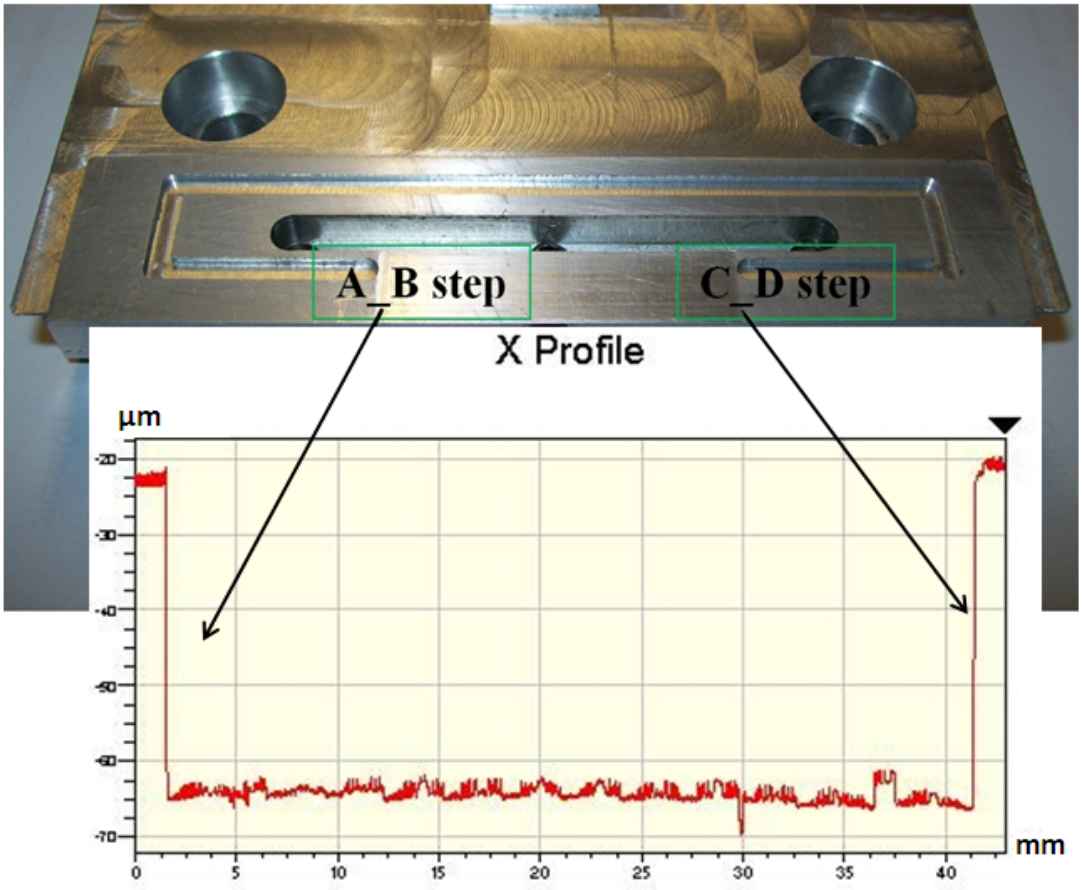

Figure 8.2b: A_B and C_D steps define the geometry of feeding slit: its width is 40 mm while the average height step is about 45 microns (measurement taken with a non-contact WYKO white-light interferometer). These parameters are useful for dimensioning the exit flow.

In particular, attention is focused on the requirements to be met for generating a sustainable thin film flow (the order of 100 microns).

8.1.1 *Set-up requirements*

The flow generated for the study of thin fluid films over topography has to meet the following requirements:

- stable against disturbances over the measurement interval
- its thickness (i.e. the height of the fluid flowing down) has to be enough to generate a detectable modulated fringe pattern
- its flow rate has to be constant during the acquisition time period

In addition, the flow has to be laminar[1] next to the topography area **[107]**.

The geometry of the (flow rig) slit suggests some parameters to be taken in consideration. The slit mounted on the inclined plate allows the gravity driven fluid to flow down with a flow rate depending on width and height of the slit (geometrical parameters). Under these conditions, it can be proven that the entire flow over the inclined plate can be divided in two parts: first the flow inside the slit which is described as a Poiseuille[2] flow (because no turbulence occurs).

Hence, the flow rate through a rectangular slit of width *b* and height *d* can be written as **[109]**:

$$Q_{slit} = -\frac{1}{12\mu}\frac{dP}{dx} b\, d^3 \qquad \text{(eq. 8.1)}$$

where μ being the dynamic viscosity of the fluid [$m\,Pa\,s$] and dP/dx is the pressure gradient necessary to force the fluid through the slit [$kg/(m^2 s^2)$].

This pressure is exerted by a reservoir (see previous Figure 8.1) raised to a height, *H* with respect to the outlet of the slit.

Therefore the pressure can be rewritten as **[33]**:

$$\frac{dP}{dx} = -\rho\, g\, \frac{H}{D} \qquad \text{(eq. 8.2)}$$

with ρ the fluid density [kg/m^3], g the acceleration of gravity [m/s^2] and D the length of the slit in the flow direction.

Second the flow flowing down the inclined plane, in steady state condition, can be expressed as (α is the angle the slit makes with the horizontal, **[33]**):

$$Q_{inclined\ plane} = \frac{1}{3\mu} B\, \rho\, g\ h_\infty{}^3 \sin\alpha \qquad \text{(eq. 8.3)}$$

This last relation takes into account the actual width of the liquid film on the inclined plane, *B* and the asymptotic film thickness, h_∞.

([1]) Type of fluid flow in which the fluid travels smoothly or in regular paths, in contrast to turbulent flow, in which the fluid undergoes irregular fluctuations and mixing **[106]**.

([2]) Poiseuille flow is pressure-induced flow (Channel Flow) in a long duct, usually a pipe **[108]**.

By comparing the two flow rates one can know the expected (theoretical) thickness of the flow with respect to the height of the slit and the angle the slit makes with the horizontal (Figure 8.3).

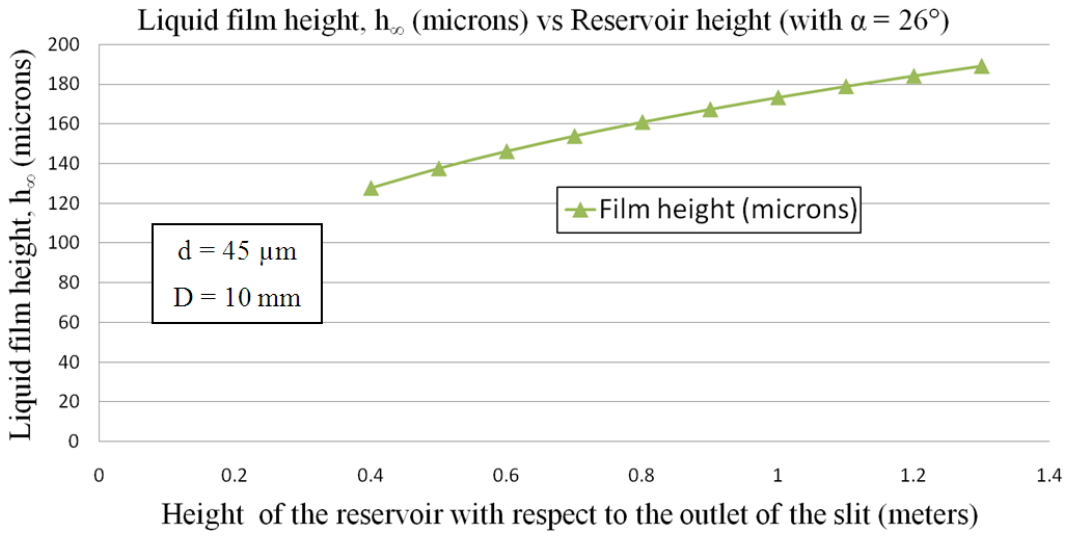

Figure 8.3: Showing the relationship between thickness of the film and height of reservoir once the angle (α) the slit makes with the horizontal is known

Indeed, comparing the two previous flow rates gives:

$$h_\infty = d\left(\frac{1}{4D\sin\alpha}\right)^{\frac{1}{3}} H^{\frac{1}{3}} \qquad \text{(eq. 8.4)}$$

In our case, d = 45 µm, D = 10mm and α = 26°:

$$h_\infty \cong 173 H^{\frac{1}{3}} \qquad \text{(eq. 8.5)}$$

with asymptotic film thickness, h_∞ in microns and reservoir height, H in meters.

It would be interesting to notice that one will expect to have the same film thickness with all fluids as density and viscosity cancel. In essence, the asymptotic film thickness, h_∞ is independent of the fluid viscosity **[33]**.

8.1.2 *Improvements*

Under the previous conditions it would be possible to predict the liquid film thickness flowing down the inclined plate. In reality, some issues have to be addressed in order to maintain a stable and controllable flow rate over the whole period of measurement.

Figure 8.4 shows the overall flow rig. In particular, a clear float glass (100 GC 100, Comar Optics) was used as a reference surface to create a topography feature.

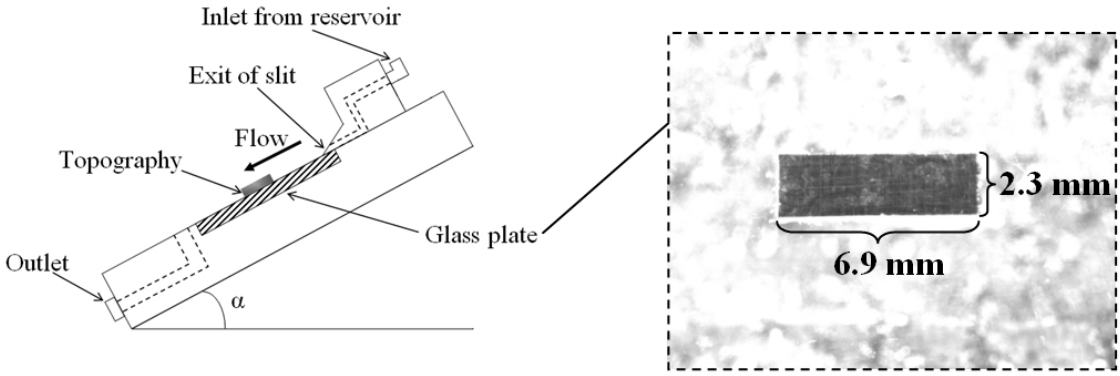

Figure 8.4: (Left) Schematic design of the inclined support showing the glass plate (100 × 100mm, 3mm thick) with the topography (right) used for the experiments. Glass to metal bonding was successful by means a UV glue. The metal thickness is 60 ± 2 microns, including the adhesive thickness.

In addition, because the study is focused on the shape of the thin liquid film flowing over a glass plate, it is necessary that the flow motion is not perturbed by impurities on the glass surface. In our case, the assumption of having a laminar flow is strictly true if no (local) flow turbulences occur. Hence, the cleaning procedure is absolutely fundamental. Indeed, during the first experiments, it had been observed that the liquid film tends to organize the flow in a non-uniform manner. This effect depends on the wettability[3] of glass.

([3]) Wettability is defined as the tendency of one fluid to spread on or adhere to a solid surface in the presence of other immiscible fluids **[110]**

In our case, ideally the lower the wettability the easier the flow can flow over the glass surface because the liquid tends to spread over the contact surface (i.e. the glass plate). Figure 8.5 illustrates three cases with different solvents.

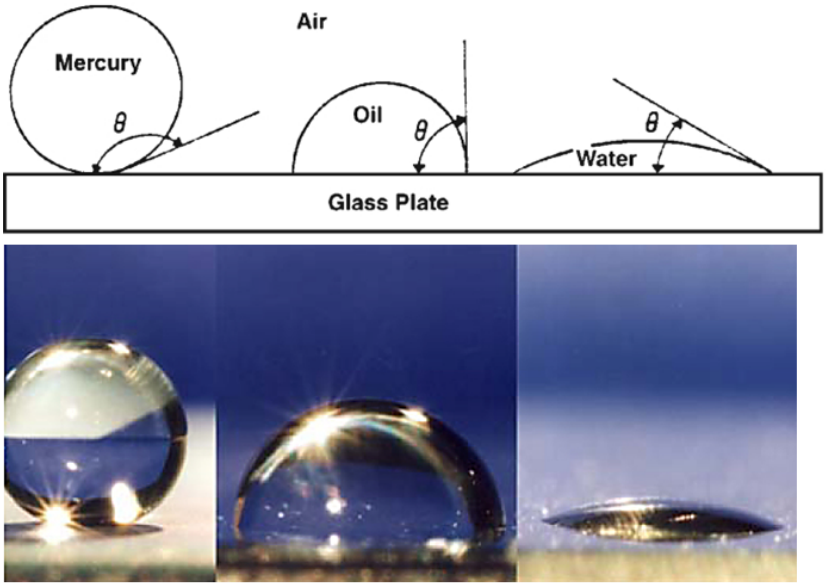

Figure 8.5: (Top) Illustration of wettability for three different solvents. As the contact angle, θ tends to decrease, the wetting characteristics of the liquid increase **[110]**. (Bottom) The real case of a fluid with different surface wettability (adapted from IKV, Institut Für Kunststoffverarbeitung).

In particular, it has been seen that the wettability of glass depends on the concentration and composition of the surfactant[4] mixture **[112]**.

As stated from the Chapter 4, the fluid used for our experiments is a saturated solution of Rhodamine B (Chloride) dissolved in ethanol. In our case, the glass surface showed a better wettability when cleaned with isopropyl alcohol and denatured water.

([4]) Surfactants (contraction for surface-active agents) are compounds that tend to reduce the surface tension of a liquid in which it is dissolved, the interfacial tension between two liquids, or that between a liquid and a solid **[111]**

Another potential issue to be considered is related to the CCD camera position respect to the inclined plane. The camera axis has to be perpendicular to the inclined support (metal structure with glass and topography) in order to maintain the same configuration adopted during the calibration procedure. This target has been achieved by mounting the whole inclined support on a micrometric stage held in place with a threaded collar driven by means of a lead screw (Figure 8.6).

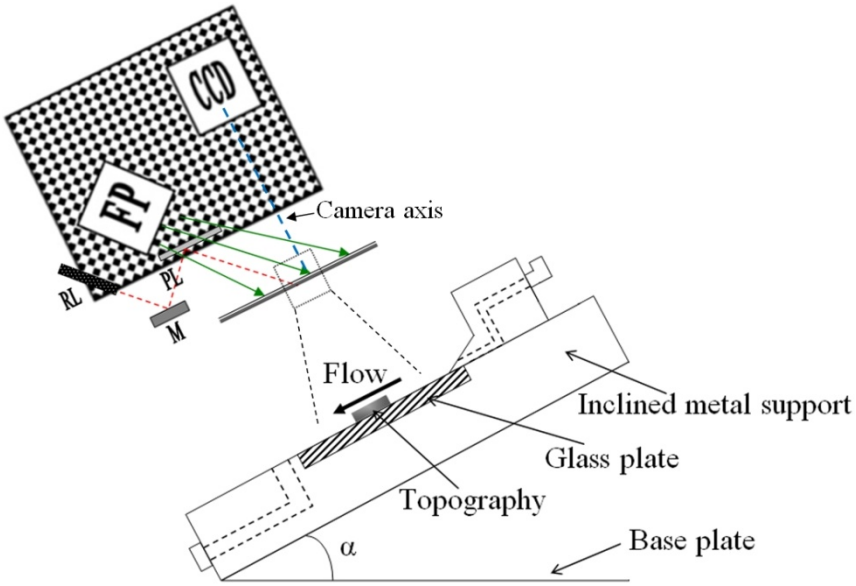

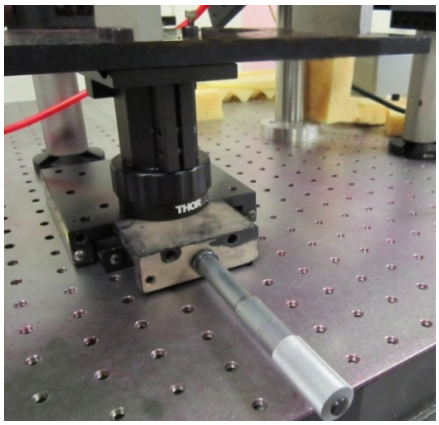

Figure 8.6: (Top) Layout showing the typical set-up configuration adopted during the experiments. Fringe projector, FP and CCD camera are rigidly connected with the red laser spot projector, RL used to have an absolute zero in the unwrapped phase map (see Fig. 6.5 Chapter 6 for further details). Camera axis is set to be perpendicular to the glass plate with topography.
(Bottom) Particular of the translation stage mounted under the aluminium breadboard (base plate).

The reproducibility of the flow is one of the biggest issues in this kind of (dynamic) configuration setups. Any variation of the slit height from the nominal value implies a thickness change in the flow. For example, a variation of 5 microns in slit height yields a thickness change of about 17 microns (Figure 8.7).

This effect could be observed if there is a non-perfect adherence between the exit of the slit plane and the glass plate (for example, due to impurities).

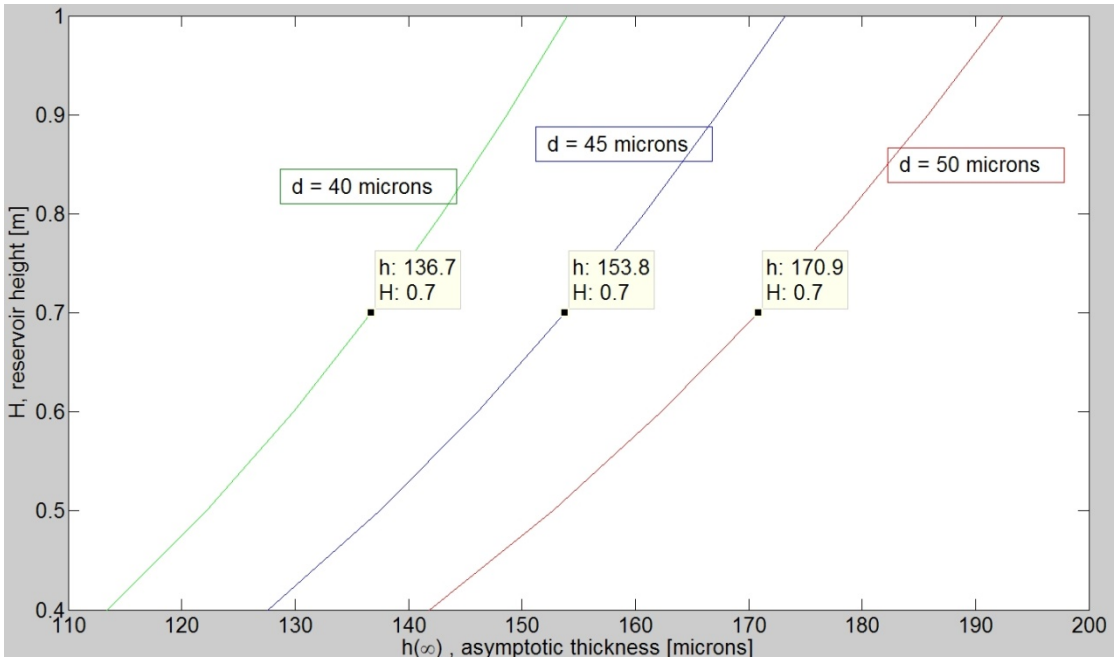

Figure 8.7: The plot shows, for the same reservoir height, H the variation of asymptotic fluid thickness, h_∞ when the slit height changed, d.

However, the model predictions (eq. 8.1-8.5) provided a relation between the asymptotic fluid thickness (h_∞), the geometrical set-up parameters (reservoir height, H and inclination angle, α) and the slit parameters (slit height, d).

It would be noted that, by interferometric measurements using fluorescence from a concentrated dye solution, it is not possible to have an absolute value of flow thickness (i.e. the height of the fluid with respect to the glass plate interface) but variations of the profile.

The film thickness value has been obtained by using the red laser spot projector (RL), used to have an absolute zero in the unwrapped phase map. First a reference (for the spot coordinates) is taken when the glass plate is completely dry (Figure 8.8a, left). Then a successive reference is taken when the glass plate is covered by the flow (Figure 8.8a, right). As seen from the CCD camera the projected spot moves along the X-axis (from the left to right side as the fluid height increases, as illustrated in Figure 8.8b).

By knowing the angle of incidence (45°) and the scale of the image (12.7 μm per pixel in the object plane, as seen from the CCD camera) one can get a better estimation of the fluid height.

Therefore all values of h_∞ reported here have been obtained by measuring the flow in this way.

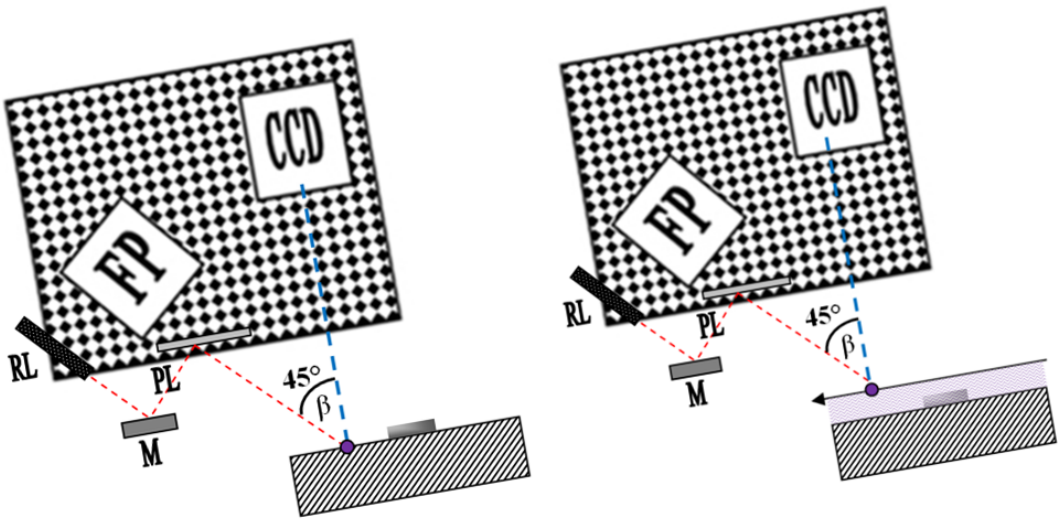

Figure 8.8a: Estimation of the fluid thickness. The red laser spot projector, RL is set to be collinear with the fringe projector block, FP by means of a mirror, M and a pellicle beam splitter, PL. The resulting laser beam forms an angle of 45° with the CCD camera axis. (Left) The projected spot coordinates are taken when the inclined glass plate is dry (see also Figure 8.8b, left). Then (right) a second spot reference is taken with the fluid (see also Figure 8.8b, right). The two spot coordinate sets are collected in order to have an estimation of the fluid thickness as difference of the two spot heights.

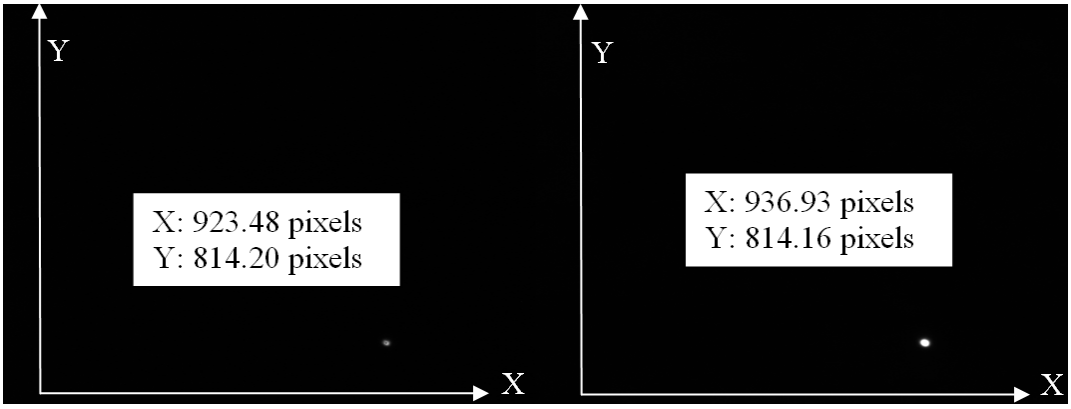

Figure 8.8b: Projected spot and its image coordinates (as seen from the CCD camera) when the glass plate is dry (left) and covered by real flow (right). From the CCD camera point of view (placed at normal incidence with the glass plate) the spot moves from the left to right side as the fluid height increases (i.e. its X-axis coordinate increases).

8.2 *Experimental results*

The following results are based on the system after calibration as described in Chapter 6. The fluid used is a saturated solution of Rhodamine B (Chloride) dissolved in ethanol (48 mM, Molarity) as illustrated in the previous Chapter 7 for the experiments with static fluids (Section 7.2). The following figure (Figure 8.9a) illustrates the case of a gravity driven flow over the topography (as seen from the CCD camera) when the measured fluid thickness is around 160 microns. The nominal thickness of the topography is about 60 microns (the lateral dimensions are 6.9 × 2.3 mm, see previous Figure 8.4). The actual field of view of the camera is about 16.3 × 12.2 mm (1280 × 960 pixels). The fringe separation is around 500 μm as viewed by the camera. The lateral resolution, as determined by means of a 1951 USAF resolution test target, is 12.7 microns (this is due to the pixel spacing, see also previous Figure 8.8a).

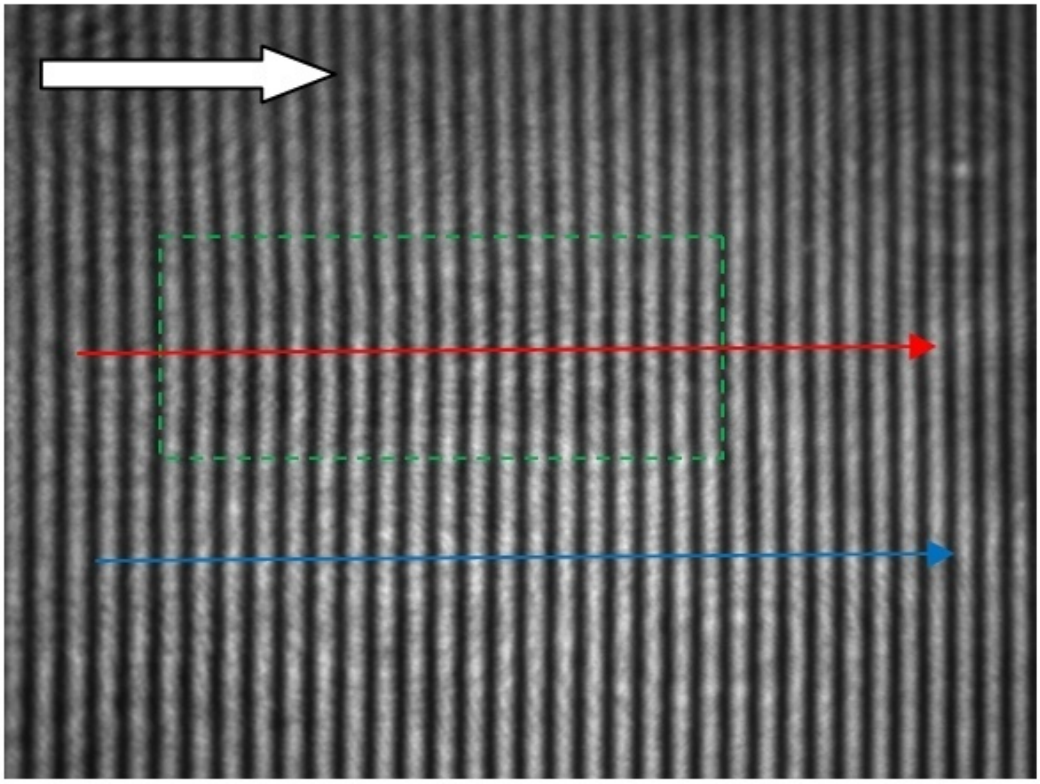

Figure 8.9a: The arrow points in the direction of fluid flow. The estimated asymptotic thickness is around 160 μm. The dotted-green box highlights the area where the topography is. Two different rows (into the image) have been selected for plotting the height change graph (see Figure 8.9b). The red one is right on the topography while the blue one is within a 'flat' area (fluid over the glass plate).

According to the phase stepping algorithm developed (see Section 5.3, Chapter 5) one set of phase-stepped frames have been collected. The estimated average phase step, for the 4-stepped frames, is 90.007 degrees. Moreover, on the basis of calibration coefficients collected, the unwrapped phase map has been processed in order to have an estimation of the fluid height variation across the field of view (phase to height relationship as discussed in Par 6.1, Chapter 6).

The following figures are surface (lines, for the 2D plots) showing the result of the unwrapping process followed by conversion to z coordinates in microns.

Hence, the following Matlab plot shows the height change between the rectangular topography (shown in red and marked as "topography position") and a 'flat' area (liquid flow flowing down the glass plate, marked in blue) over the whole field of view (16.3 × 12.2 mm). Indeed, two rows of the previous image (Figure 8.9a) have been selected then the 2-D plot shows the relative height against the columns (pixels) of the whole image (cross-section, Figure 8.9b).

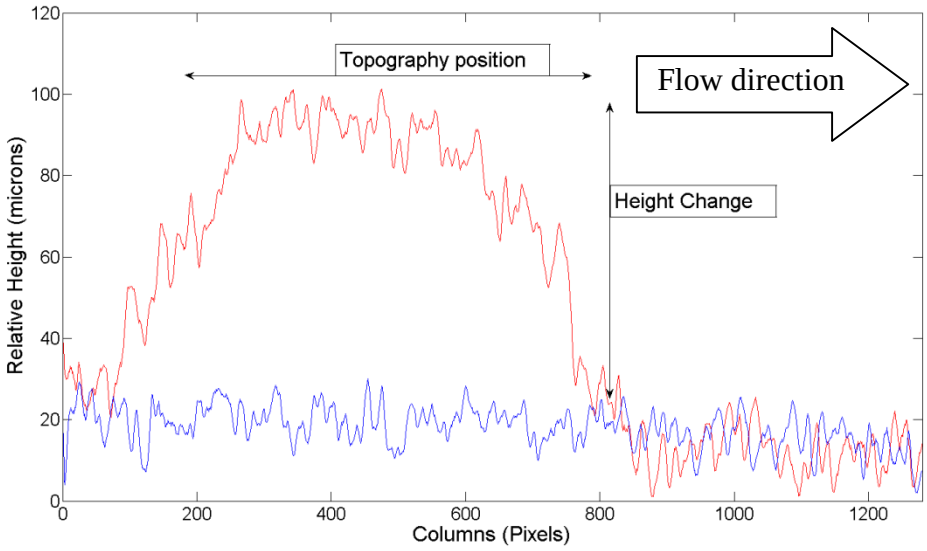

Figure 8.9b: According to the Figure 8.9a: one row of the image, across the field of view, includes the topography location (red). The fluid height change highlights the presence of the 60 micron step between the topography and an area without any topography (i.e. liquid flowing over the glass plate, marked in blue).

The cross-section of the measured profile shows clearly the topography presence. The standard deviation is about 2.3 micron of the measurement volume dimension (about 250 micron high, for this set of images). It has been decided to implement a polynomial fit in order to reduce the residual noise visible in the images (2D and 3D plots). Target of this process is to "smooth" out the collected data noise leaving unaltered the topography shape (already visible in the raw images). In general, this process ("smoothing") is equivalent to low-pass filtering which reduces the high-frequency components of a signal while retaining the low-frequency components. By comparison with different polynomial order fits, it was found that a 10^{th} order polynomial trend (evaluated using least squares fits in Matlab, see for example the next Figure 8.9c) tends to filter out a significant portion of the data's high-frequency content. In general, higher degree polynomials can more accurately capture the heights and widths of narrow peaks (relative to the added noise), but leave undesirable levels of noise over wider peaks (i.e. in this case, the topography shape results better "preserved") **[113]**.

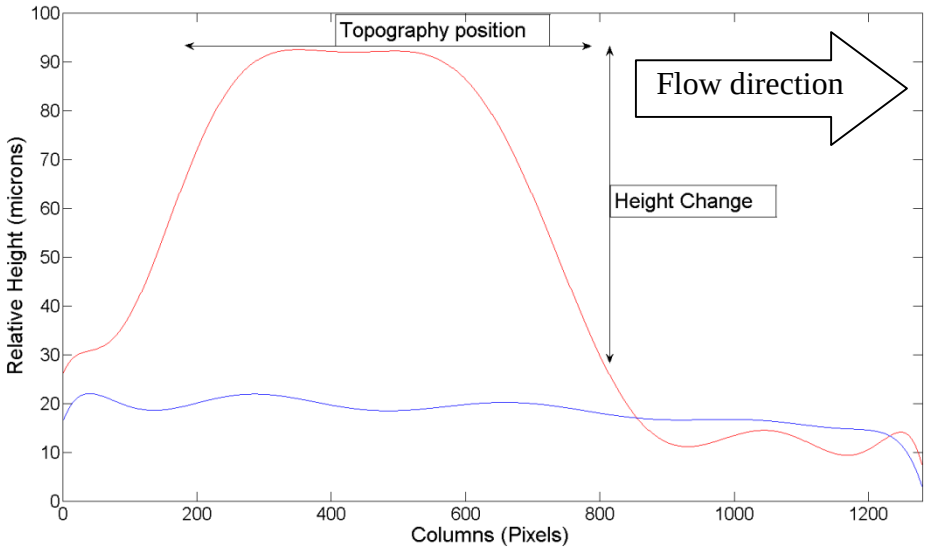

Figure 8.9c: Showing the result of 10^{th} order polynomial fit applied to the data of Figure 8.9b. Topography location and height change are clearly depicted. For reference, the blue line represents the cross-section of the liquid flowing over the glass plate far from the topography.

The surface plot (3D Matlab representation) in Figure 8.10a (top of figure) shows the full field of view (16.3 × 12.2 mm) where all data points have been plotted along each axis. It would be interesting to notice that there is a minor orientation difference between the shape measurement system and the flow rig. Any residual minor orientation differences have been reduced with an appropriate Matlab code. The resulting plot is shown in Figure 8.10a (bottom of figure).

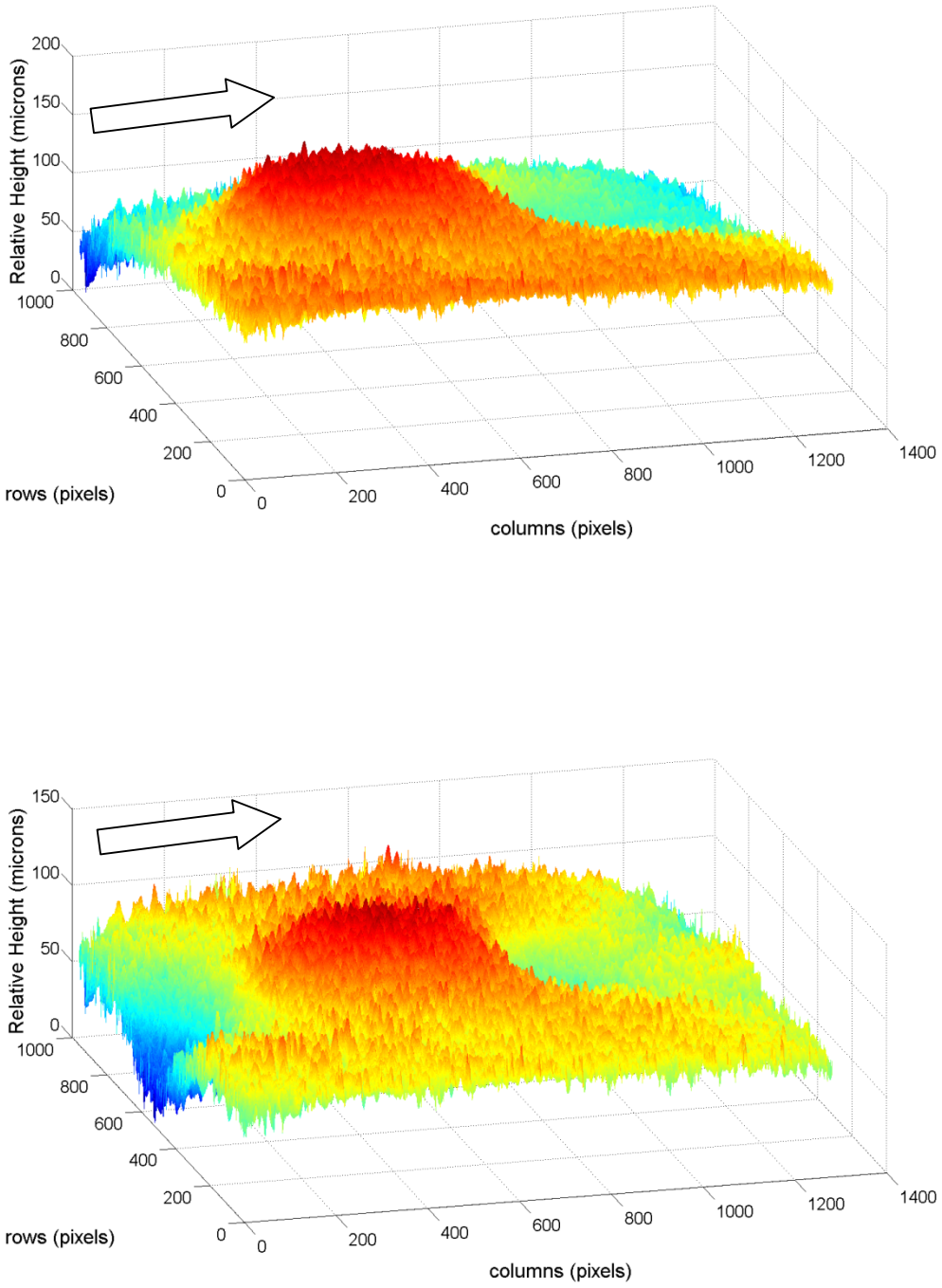

Figure 8.10a: (Top) Full field of view (16.3 × 12.2 mm) of the reconstructed 3D surface. There is a minor orientation difference between the shape measurement system and the flow rig. (Bottom) The orientation difference has been compensated by subtracting the slope in x and y of the 3D data from the original data. The white arrow indicates the (fluid) flow direction.

Previous surface plots show a residual noise likely due to the residual phase noise in the fringe projection system. The following (Figure 8.10b) is the result of a 10th order polynomial fit applied to each row of the 3-D image. Whilst this processing makes the profile of the film clearer over the topography, it introduces a problem of oscillations at the edges of the interpolation interval (1-1280 pixels) which is expected when using polynomial interpolation with polynomials of high degree[5].

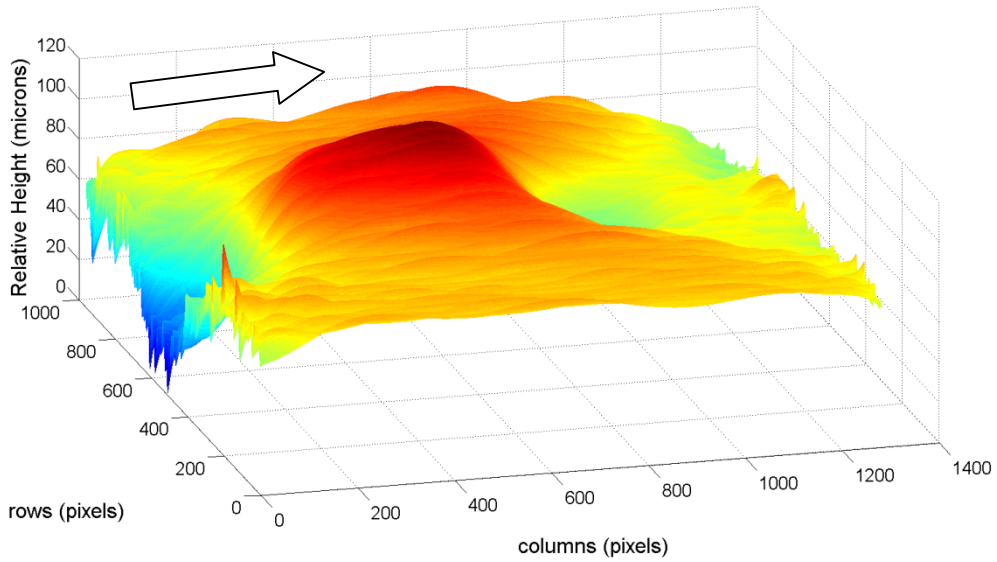

Figure 8.10b: Showing the result of *polyfit* and *polyval* functions (10th order polynomial fit) applied to every single row of the above 3D plot (Figure 8.10a, bottom). The white arrow indicates the (fluid) flow direction.

The estimated asymptotic thickness (160 microns) results are in good agreement with the theoretical value (eq. 8.4). In particular, with the height of the reservoir of 0.7 m and an inclination angle of 26° the theoretical asymptotic thickness is 153.8 microns (as shown in previous Figure 8.7). The following plots (Figures 8.11-8.12) show an example of fluid flow with an estimated thickness of about 300 microns. The average phase step for the new set of four stepped images is 89.858 degrees.

([5]) Runge's phenomenon discovered by Carl D. T. Runge (1901). *"Über empirische Funktionen und die Interpolation zwischen äquidistanten Ordinaten"*, Zeitschrift für Mathematik und Physik 46: 224–243.

With a similar data processing approach (see previous Figure 8.9c) a fitting polynomial has been applied to each row of the 2D Matlab plot (raw data). The following (Figure 8.11) shows the result of the 10th order polynomial fit. It is interesting to notice that two surface depressions are visible either side of the topography in the direction of flow. In light of the likely stability of the flow (according to the model predictions described by eq. 8.1-8.5) the Reynolds number earlier introduced (p. 24, Chapter 2) may give a further indication on the stability. Re-writing the previous expression for the Reynolds number, in the case of gravity-driven flow over a profile inclined of an angle α, yields **[107]**:

$$Re = \frac{\rho V L}{\mu} = g \frac{h^3 \sin\alpha}{3\mu^2} \rho^2$$

where μ being the dynamic viscosity of the fluid [$kg\,m\,s$], ρ the fluid density [kg/m^3], g the acceleration of gravity [m/s^2] and h the local film thickness.

Decré and Baret reported **[33]** similar flow structures in the case of square (step-down, step-up) topography when the height ratio (dimensionless) between topography height and asymptotic fluid thickness is around 0.2 and Reynolds number ranges from 0.84 and 2.83 (assuming ρ*=1000* [kg/m^3], μ*=0.001* [$kg\,m\,s$], α = 30° and the fluid thickness ranging between 80 and 120 μm, as reported in **[33]**). According to the equation $Re_{crit} = \frac{5}{4}\cot\alpha$ (**[40, 41]**, see p. 25 Chapter 2) the expected critical value is 2.56 in the experiments reported in this chapter. However, although the experimental data collected (concerning the dynamic flow with an estimated thickness of about 300 microns) show the presence of two "depressions" near the topography feature even in the raw data (i.e. the data with the residual noise *before* any polynomial smoothing, see for example top of Figure 8.12) and describe some *qualitative* features of the experiment by Decré and Baret **[33]** a quantitative comparison does not seem possible due to the different fluid generation into the experiments involved (demineralized water **[33]** against a saturated solution of Rhodmine B dissolved in ethanol) and the restricted size of the experiment (in our case, the topography can be considered as one rectangular step-up, step-down structure). The height ratio is around 0.2 because the topography height is 60 microns with the estimated liquid thickness being 300 microns high. Moreover, the

use of demineralized water in Decré and Baret experiments ensures a complete knowledge of the fluid parameters (in particular the fluid density, dynamic viscosity and surface tension). In addition, the optimized dye solution used in this thesis doesn't enable a precise value of the dynamic viscosity to be known, μ [$kg\,m\,s$] and the fluid tension ρ [kg/m^3] (an estimation of this last parameter could be achieved assuming $\rho_{dye} << \rho_{Ethanol}$ as the molarity value (48 mM) and Rhodamine molar weight (479) are known).

However, it has been demonstrated **[114]** that Rhodamine B can act as a surfactant (reducing the surface tension of the liquid in which it is dissolved) in water-solvent mixtures. It would be interesting to examine the effect of surfactant on the stability of the film flowing down an inclined plane **[115]** in the case of Rhodamine B acts as a surfactant in Ethanol (spectrometric grade). Indeed, M. G. Blyth and C. Pozrikidis have demonstrated that the primary role of the surfactant is effectively to raise the critical Reynolds number at which instability is first encountered **[115]**.

Finally, an accurate knowledge of the fluid parameters involved in this experiment would also give a correct Reynolds number for a deeper investigation of fluid stability according to the linear stability constraint on gravity-driven films **[40, 41].**

These results demonstrate the ability of the proposed technique to obtain free surface topography measurements of thin films using a set of phase stepped images (captured in <1 second). The acquisition time is significantly less than the (up to 1 hour) time required for data capture using the classical interferometry approach used by Decré and Baret **[33]**. Therefore, the proposed approach opens up the potential to study dynamically evolving or evaporating fluid films. The resolution of the data obtained at +/- 2 microns is worse than that achieved by Decré and Baret. However, the resolution reported here could be improved with the existing equipment by using projected fringes with a reduced period.

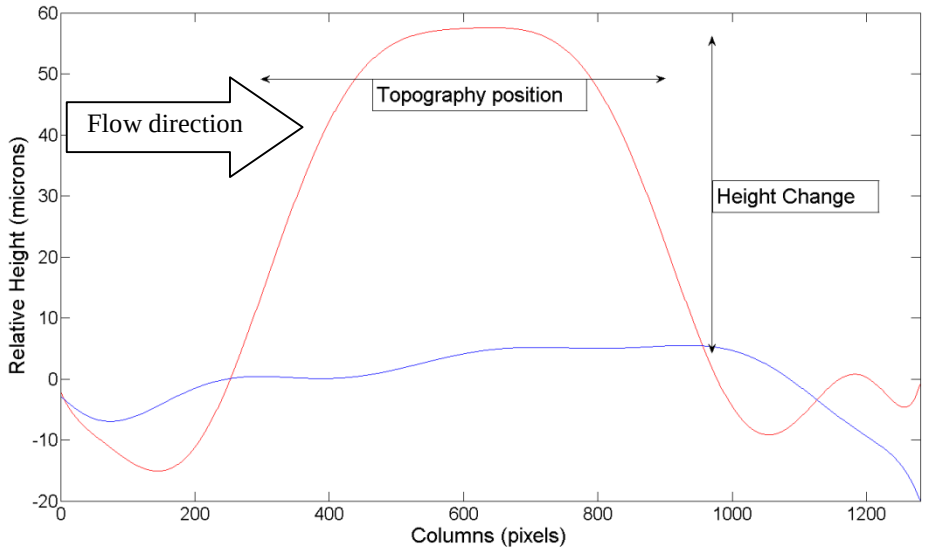

Figure 8.11: Showing the result of *polyfit* and *polyval* functions (10^{th} order polynomial fit) applied to every single row of the 2D raw data plot. Topography location and height change are clearly delighted. For reference, the blue line represents the cross-section of the liquid flowing over the glass plate far from the topography. The estimated fluid thickness is about 300 microns.

The surface plots (3D Matlab representations) in Figure 8.12 show the full field of view where all data points have been plotted along each axis both before and after applying the 10^{th} order polynomial fit (Figure 8.12, bottom).

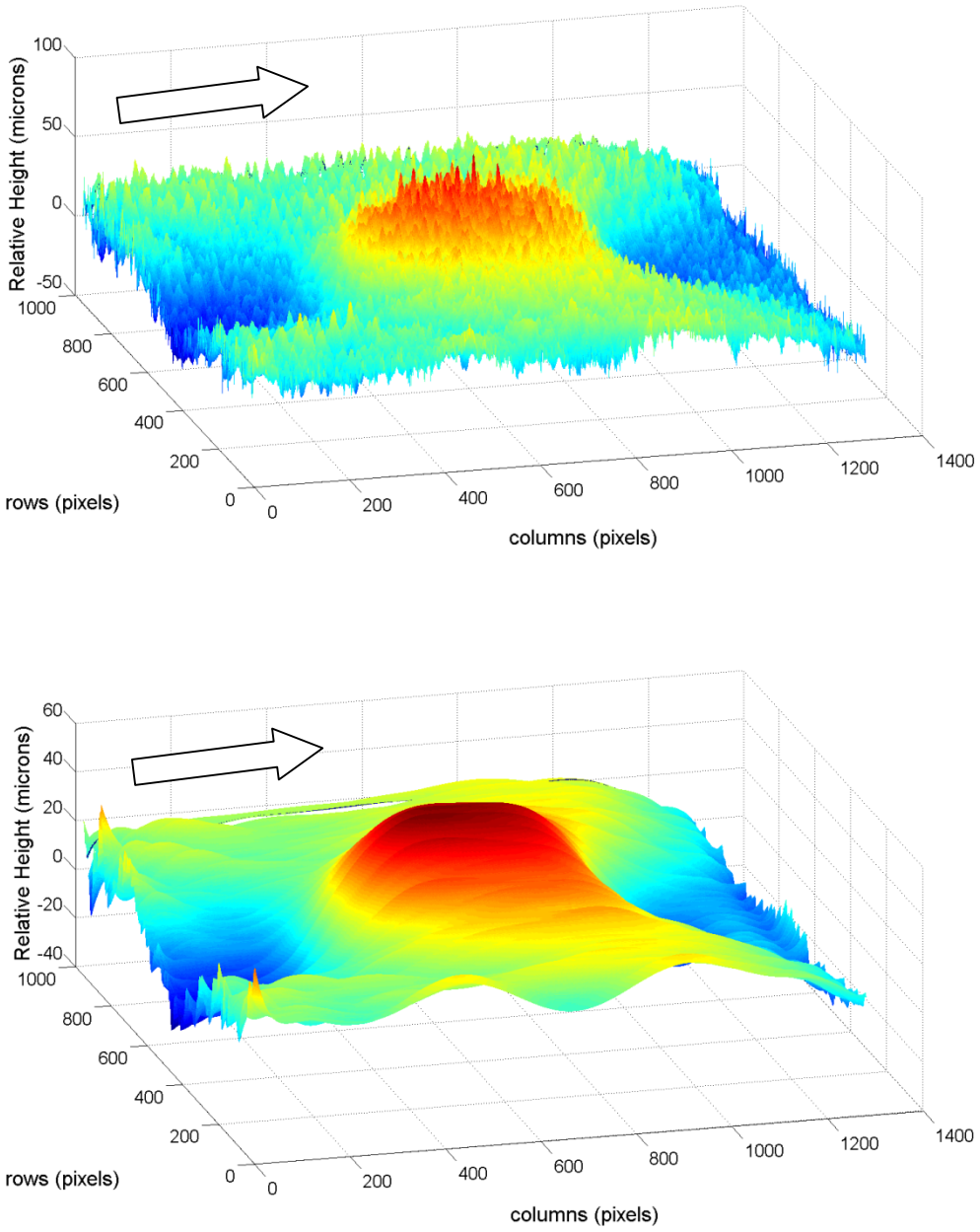

Figure 8.12: 3D reconstructed surface plots for the raw data (top) and the post-processed data (bottom) by means of a 10^{th} order polynomial fit (*polyfit* and *polyval*, Matlab functions). Two surface depressions (blue area) are visible near the topography edges. The polynomial fit makes viewing the two features rather easier. The white arrow indicates the (fluid) flow direction.

8.3 *Summary*

This chapter illustrated some results of the technique developed in case of experiments involving dynamic liquids. The proposed shape measurement system with a suitable fluorescent solution (a saturated solution of Rhodamine B dissolved in Ethanol) has been applied for the measurement of the surface profile in fluid thin film flowing over topography. In particular, a flow rig set-up has been built in order to test the shape measurement system in presence of real liquid flows. Realization of the inclined system (gravity assisted) and topography have been achieved on the basis of a theoretical model (laminar flow) and some practical set-up improvements (increased wettability of the glass and micrometric translation stage). On the basis of calibration results (relationship between phase maps and surface height), some experiments have been carried out using the best dye solution in terms of fluorescence emission and light depth penetration (as illustrated in Chapter 4). The profile of the exterior surface of these fluids has been investigated by means of a phase-stepping technique and the phase-height relationship. Two different liquid flow thicknesses have been processed and analysed. In particular, for the 300 micron high fluid, the presence of two surface depressions near the edge of the topography has been noticed in the flow direction. This result seems, to a first approximation, to be *qualitatively* in agreement with the experimental results found in literature (Decré and Baret work) for the study of similar structures in experiments of gravity driven (water) film flowing down inclined plates. Further investigations on different topography features/fluid thickness will be necessary for a complete quantitative comparison.

Chapter references

[105] DIPRESA D, TOWERS CE, and TOWERS DP. 5th September 2012. Metrology of Thin Films using Interferogram Analysis Techniques. *In*: Photon12 (Conference presentation). Durham, UK.

[106] MASSEY, B. 1988. Mechanics of fluids (revised by John Ward-Smith). Cheltenham: Stanley Thornes (ISBN: 0278000479).

[107] MESSÉ S and DECRÉ MMJ (1997). Experimental study of a gravity driven water film flowing down inclined plates with different patterns. Spin coating over een puntje (SOEP). *Unclassified Report*, PHILIPS ELECTRONICS.

[108] RICHARDSON SM (1989). Fluid Mechanics. New York: Hemisphere Publishing Corporation (ISBN: 0891166718).

[109] Dunn DJ. Fluid Flow Theory. TUTORIAL No. 1 (2006). Available from http://www.freestudy.co.uk/fluid%20mechanics/t1203.pdf (Accessed: 27/05/2013).

[110] AHMED TH (2006). Reservoir Engineering Handbook. Burlington, MA: Elsevier/Gulf Professional. (ISBN: 9780750679725).

[111] ROSEN MJ and KUNJAPPU JT (2012). *Surfactants and Interfacial Phenomena*. New York: John Wiley and Sons (ISBN: 9780470541944).

[112] SZYMCZYK K and JANCZUK B (2008). Wettability of a glass surface in the presence of two nonionic surfactant mixtures. *Langmuir: the ACS journal of surfaces and colloids* **24**(15), 7755-7760.

[113] THE MATHWORKS, INC. (2013). *Filtering and Smoothing Data*. Available from *http://www.mathworks.de/de/help/curvefit/smoothing-data.html* (Accessed: 27/05/2013).

[114] THIJSSEN JHJ, SCHOFIELD AB, and CLEGG PS (2011). How do (fluorescent) surfactants affect particle-stabilized emulsions? *Soft Matter* **7**(18), 7965-7968.

[115] BLYTH MG and POZRIKIDIS C (2004). Effect of surfactant on the stability of film flow down an inclined plane. *J. Fluid Mech.* **521**, 241-250.

Chapter 9

Conclusions and Future Work

In this thesis a new approach for metrology of thin liquid films by using laser fringe projection with fluorescent dyes was presented[1]. This study included an explanation of the techniques developed so far, the characterization of suitable dyes, the description of the imaging system and the experimental development of a flow rig suitable for the study of dynamic liquid flows.
This chapter summarises the achievements and discusses perspectives of future work.

The major achievements presented in this thesis are described in the following sections.

9.1 *Characterization of fluorescent dyes for laser based fringe projection*

- A new approach to measure the shape of thin fluid films was presented. The proposed approach made use of suitable dyes for measuring the surface topography of thin fluid films by fluorescence based fringe projection (narrow band laser illumination).

- Three different fluorescent dyes were presented as their absorption spectra match the frequency of the laser source available (main laser input power of 200mW at 532nm) and also the spectral sensitivity range of the CCD device.

- Characterization of fluorescent dyes was carried out following two criteria: penetration depth for the laser light passing through the dye dissolved in a solution and fluorescence intensity of the candidate fluorescent dyes in order

[1] The results of this work will be submitted to Optics Letters (Journal paper).
Authors: D. Dipresa, D.P. Towers, C.E. Towers.
Affiliation: School of Mechanical Engineering, University of Leeds, Leeds. LS2 9JT.

to match the maximum peak of fluorescence emission with the lowest depth of penetration of the light into the fluid as needed for the investigation of thin fluid films. Some practical experimental setups were arranged in order to validate the theoretical approach.

- Under the two previous criteria, the best combination was a saturated solution of Rhodamine B chloride as it shows sufficiently strong absorption (light depth penetration of about 4 μm) but without significant loss of emission intensity with increasing dye concentration (as required for the study of the surface topography of thin fluid films).

9.2 *Imaging system for thin (liquid) film measurement*

- Experimental setups were arranged for the production of laser based fringes by the interference between two coherent waves using a diffraction grating (grating based fringe projection) or a pair of single mode fibers (twin fiber system).

- Compared the phase resolution achieved by the twin fiber approach with the grating system, the twin fiber configuration was proposed in order to provide sufficient excitation (200 mW laser source at 532 nm, green light) for the fluorescent dyes dissolved in the fluid. The key feature is the idea of using a fluorophore with laser fringe projection for profilometry of the outer geometry of the fluids. A rotatable mount made the laser fringe projector suitable for different experiments involving static and dynamic fluids. The imaging system proposed was extended in order to make the twin fiber system robust against the environmental instabilities and suitable for phase stepping algorithm implementation (LabView code).

9.3 *Experiments on static and dynamic fluids based on phase to height calibration*

- After the system calibration, the unwrapped phase to height relationship was found. The profile of the exterior surface of static fluids has been investigated by means of phase-stepping technique.

- Some experiments on static fluids have been carried out using an open-top vessel rig and a clear glass flow cell both filled up with a saturated solution made of Rhodamine B (Chloride) dissolved in ethanol. This fluorescent solution was the best dye solution in terms of fluorescence emission and light depth penetration.

- A flow rig set-up (gravity assisted inclined system) was built in order to test the shape measurement system in presence of real liquid flows (at different thickness) over topography of known geometry. Its realization was based on a theoretical model (laminar flow) and some practical set-up improvements.

- Two different dynamic (real) liquid flow thicknesses (160 and 300 microns) were generated and analyzed. In particular, for the 300 micron high fluid, two surface depressions, near the edge of the topography, were noticed in the flow direction. This result seem to be in agreement with the experimental results found in a previous work (Decré and Baret) concerning the study of similar structures in experiments of gravity driven (water) film flowing down inclined plates.

- The experimental results showed that the resolution achieved, over a field of view of 16 × 12 mm, is less than 2 microns (to 1 standard deviation) which is sufficient for the thin films to be considered in this project.

9.4 *Outlook*

From the main focus of this thesis, the following areas of future work have been identified.

9.4.1 *System improvements*

- The results presented in this work used a narrow band laser illumination demonstrating ability to measure fluids with sub-micron resolution over a field of view of >10 × 10 mm (16.3 × 12.2 mm). Further measurements may be taken with the proposed imaging system and different combinations of magnification – field of view by means of a new pair of CCD camera and main lens.

- The overall system could be re-arranged in order to have a system suitable for the shape measurement of fluids with different dynamic flow rig setup. For example, by means of a new reservoir-pump system.

9.4.2 *Measurements with different fluid-topography combinations*

Given the increasing requirement of fabrication processes where the definition of very small geometries is required (e.g. a photolithographic pattern for manufacturing of integrated circuits) further measurements of the 3-D flows are required as follows.

- Using the method proposed (and the flow rig set-up built) the shape measurements of liquid thin films could be obtained with different topography geometries and fluid thickness. In particular, new experiments could be performed on step, trench, rectangular and square topographies in order to investigate the presence of free surface disturbances for real flows with a different ratio between topography height and asymptotic fluid thickness (0.2 was used in this thesis).

- The production of advanced topographies with different depth and lateral dimensions could be achieved by using professional (and often expensive) techniques. For instance, topographies with lateral dimensions smaller than one millimeter would require photo lithographical techniques or etching methods

Appendix A

Derivation of the Two Beam Interference Equation

For simplicity, one can consider two different light waves, $\vec{E}_1$ and $\vec{E}_2$ with the same frequency, λ both linearly polarized [1] and propagating along the x-axis. In the complex representation they can be written as:

$$\vec{E}_1 = \vec{A}_1 e^{j(kx-\omega t+\varphi_1)} \quad \text{and} \quad \vec{E}_2 = \vec{A}_2 e^{j(kx-\omega t+\varphi_2)}$$

The irradiance *I* (i.e. the flow of energy per unit area per unit time) at a point x_0 is proportional to the square of the amplitude of the electric field [2]:

$$I = \varepsilon_0 c n \langle \vec{E}^2 \rangle$$

where ε_0 is the permittivity of free space, c is the speed of light in vacuum and n being the refractive index of the medium.

The resultant field is the linear superposition of the two waves:

$$\vec{E} = \vec{E}_1 + \vec{E}_2$$

Hence, the irradiance can be re-written as:

$$I = \varepsilon_0 c n (\vec{E}_1^{\,2} + \vec{E}_2^{\,2} + 2\vec{E}_1 \cdot \vec{E}_2)$$

with

$$\vec{E}^2 = \vec{E}^2 \cdot \vec{E}^2$$

According to the complex representation used for representing the light waves the above equation becomes (the asterisk denotes complex conjugation):

$$I = \varepsilon_0 c n(\vec{E}_1 \cdot \vec{E}_1^{\,*} + \vec{E}_2 \cdot \vec{E}_2^{\,*} + \vec{E}_1 \cdot \vec{E}_2^{\,*} + \vec{E}_2 \cdot \vec{E}_1^{\,*})$$

with the first two scalar products given by:

$$\vec{E}_1 \cdot \vec{E}_1^{\,*} = A_1^{\,2}\, e^{j(kx_0 - \omega t + \varphi_1)} e^{-j(kx_0 - \omega t + \varphi_1)} = A_1^{\,2}$$

and

$$\vec{E}_2 \cdot \vec{E}_2^{\,*} = A_2^{\,2}\, e^{j(kx_0 - \omega t + \varphi_2)} e^{-j(kx_0 - \omega t + \varphi_2)} = A_2^{\,2}$$

A very common situation [2] occurs when $\vec{A}_1$ is parallel to $\vec{A}_2$ so that:

$$\vec{E}_1 \cdot \vec{E}_2^{\,*} = A_1 A_2\, e^{j(kx_0 - \omega t + \varphi_1)} e^{-j(kx_0 - \omega t + \varphi_2)} = A_1 A_2 e^{-j(\varphi_2 - \varphi_1)}$$

and

$$\vec{E}_2 \cdot \vec{E}_1^{\,*} \overset{(1)}{=} \vec{E}_1^{\,*} \cdot \vec{E}_2 = A_1 A_2\, e^{-j(kx_0 - \omega t + \varphi_1)} e^{j(kx_0 - \omega t + \varphi_2)} = A_1 A_2 e^{j(\varphi_2 - \varphi_1)}$$

Combining the last two dot products this yields:

$$\vec{E}_1 \cdot \vec{E}_2^{\,*} + \vec{E}_1^{\,*} \cdot \vec{E}_2 = A_1 A_2 [e^{j(\varphi_2 - \varphi_1)} + e^{-j(\varphi_2 - \varphi_1)}] =$$
$$A_1 A_2 [\cos(\varphi_2 - \varphi_1) + j\sin(\varphi_2 - \varphi_1) + \cos(\varphi_2 - \varphi_1) - j\sin(\varphi_2 - \varphi_1)] =$$
$$2A_1 A_2 \cos(\varphi_2 - \varphi_1)$$

([1]) $a \cdot b = b \cdot a$ (Commutative property of dot product for vectors *a* and *b*)

Therefore

$$I = \varepsilon_0 c n [A_1^2 + A_2^2 + 2A_1 A_2 \cos(\varphi_2 - \varphi_1)]$$

Or

$$I = I_1 + I_2 + 2\sqrt{I_1 I_2}\cos(\varphi_2 - \varphi_1)$$

Where

$$I_1 = \frac{\varepsilon_0 c n}{2} A_1^2$$

and

$$I_2 = \frac{\varepsilon_0 c n}{2} A_2^2$$

References

[1] C.M. Vest. *Holographic interferometry* (1979). Wiley.

[2] E. Hecht. *Optics*, 2nd ed. (1987). Addison-Wesley.

Appendix B

The following Matlab code relies on Matlab unwrap function to generate a smooth phase distribution and assess noise level against a low order polynomial.

```
% Take out the central row for noise analysis
[nrows ncols] = size(phfft);

phrow1 = phfft( round(1*nrows/4), :);
% nrows/2 gives the middle row of the image
phrow2 = phfft( round(1*nrows/2), :);
phrow3 = phfft( round(3*nrows/4), :);

% Selects central section left to right of the wrapped phase
ileft = 300;
iright = 800;

phrowbit1 = phrow1(ileft:iright);
phrowbit2 = phrow2(ileft:iright);
phrowbit3 = phrow3(ileft:iright);

uwprowbit1 = unwrap(phrowbit1);
uwprowbit2 = unwrap(phrowbit2);
uwprowbit3 = unwrap(phrowbit3);

figure
plot(phrow1);
figure
plot(uwprowbit1);
title('Unwrapped Phase Along a Row');
ylabel('Phase (radians)');

% DO some noise analysis by polynomial fitting and looking at
residual errors
x1 = 1:length(uwprowbit1);
x2 = 1:length(uwprowbit2);
x3 = 1:length(uwprowbit3);

pn1 = polyfit( x1, uwprowbit1, 3);
pn2 = polyfit( x2, uwprowbit2, 3);
pn3 = polyfit( x3, uwprowbit3, 3); % use a 3rd order fit

uwpfit1 = polyval( pn1, x1);
uwpfit2 = polyval( pn2, x2);
uwpfit3 = polyval( pn3, x3);

pherr1 = uwprowbit1 - uwpfit1;
pherr2 = uwprowbit2 - uwpfit2;
pherr3 = uwprowbit3 - uwpfit3;

phnse1 = std(pherr1);
phnse2 = std(pherr2);
phnse3 = std(pherr3);

phnseAverage = (phnse1+phnse2+phnse3)/3;
```

```
roundAverage = round((2*pi/phnse1+2*pi/phnse2+2*pi/phnse3)/3);

s1 = sprintf('STD Noise at 1/4 row: %.3f radians, or 1/%d of a
fringe', phnse1, round(2*pi/phnse1));

s2 = sprintf('STD Noise at 1/2 row: %.3f radians, or 1/%d of a
fringe', phnse2, round(2*pi/phnse2));

s3 = sprintf('STD Noise at 3/4 row: %.3f radians, or 1/%d of a
fringe', phnse3, round(2*pi/phnse3));

sAverage = sprintf('STD Noise as average of 3 rows: %.3f radians,
or 1/%d of a fringe', phnseAverage,roundAverage);

disp(s1);
disp(s2);
disp(s3);
disp(sAverage);
```

Index

4

4D – technology · - 43 -

A

absolute zero (in unwrapped phase maps) · - 75 -, - 125 -, - 133 -, - 139 -, - 141 -
absorbance · - 54 -, - 55 -, - 61 -
absorption · IV, - 7 -, - 37 -, - 40 -, - 52 -, - 53 -, - 55 -, - 56 -, - 57 -, - 61 -, - 65 -, - 66 -, - 67 -, - 68 -, - 114 -, - 155 -, - 156 -
aerogel · - 8 -, - 9 -
algorithm · - 23 -, - 25 -, - 36 -, - 87 -, - 89 -, - 104 -, - 118 -, - 120 -, - 133 -, - 143 -, - 156 -
approximation · - 100 -

B

band · IV, - 68 -, - 71 -, - 80 -, - 94 -, - 155 -, - 158 -
band gap · - 6 -, - 7 -
band-pass filter · - 35 -
bands (interference) · - 73 -
bandwidth · - 73 -, - 115 -
beam splitter · - 22 -, - 35 -, - 80 -, - 81 -, - 86 -, - 87 -, - 133 -
Beer-Lambert law · - 52 -, - 54 -, - 55 -, - 57 -, - 58 -, - 59 -, - 61 -, - 62 -

C

calibration · IV, XVIII, - 33 -, - 88 -, - 98 -, - 99 -, - 101 -, - 102 -, - 103 -, - 104 -, - 105 -, - 106 -, - 107 -, - 108 -, - 109 -, - 118 -, - 123 -, - 126 -, - 128 -, - 139 -, - 142 -, - 143 -, - 152 -, - 157 -
Carré algorithm · - 91 -
CCD · - 31 -, - 35 -, - 36 -, - 43 -, - 45 -, - 47 -, - 53 -, - 58 -, - 62 -, - 66 -, - 71 -, - 72 -, - 73 -, - 78 -, - 84 -, - 87 -, - 88 -, - 90 -, - 93 -, - 98 -, - 100 -, - 101 -, - 105 -, - 113 -, - 133 -, - 139 -, - 141 -, - 142 -, - 155 -, - 158 -
coating · XVI, XVII, - 2 -, - 3 -, - 4 -, - 7 -, - 8 -, - 9 -, - 12 -, - 15 -, - 16 -, - 18 -, - 130 -
coherence · - 22 -, - 73 -, - 115 -
coherent · - 33 -, - 34 -, - 68 -, - 71 -, - 73 -, - 80 -, - 86 -, - 87 -, - 94 -, - 156 -
cuvette · - 54 -, - 57 -, - 66 -

D

DCM · - 53 -, - 56 -, - 59 -, - 63 -, - 66 -, - 67 -
depth · IV, - 32 -, - 34 -, - 53 -, - 54 -, - 55 -, - 56 -, - 58 -, - 59 -, - 60 -, - 61 -, - 62 -, - 65 -, - 66 -, - 67 -, - 68 -, - 108 -, - 114 -, - 124 -, - 128 -, - 152 -, - 155 -, - 156 -, - 157 -, - 159 -
depth resolution · - 75 -, - 76 -
diffraction efficiency · - 35 -
diffraction order · - 35 -, - 74 -, - 75 -, - 77 -
DMD · - 34 -
DRAM · - 8 -
dye · IV, XVII, XVIII, - 23 -, - 24 -, - 37 -, - 38 -, - 52 -, - 53 -, - 54 -, - 55 -, - 56 -, - 57 -, - 58 -, - 59 -, - 60 -, - 61 -, - 62 -, - 63 -, - 64 -, - 65 -, - 66 -, - 67 -, - 68 -, - 71 -, - 78 -, - 94 -, - 112 -, - 113 -, - 114 -, - 115 -, - 116 -,- 117 -, - 124 -, - 128 -, - 132 -, - 140 -, - 152 -, - 155 -, - 156 -, - 157 -

E

ellipsometry · - 38 -, - 39 -, - 40 -, - 41 -, - 42 -, - 47 -
emission bands · - 65 -
ERLIF · - 38 -

F

far-field approximation · - 87 -
feeler gauge · - 124 -, - 125 -, - 126 -, - 128 -
FFT · - 32 -, - 72 -, - 83 -, - 84 -, - 92 -, - 118 -
fibre · IV, IX, XVII, - 35 -, - 36 -, - 63 -, - 64 -, - 68 -, - 71 -, - 72 -, - 78 -, - 79 -, - 80 -, - 81 -, - 82 -, - 83 -, - 84 -, - 85 -, - 86 -, - 88 -, - 89 -, - 94 -, - 113 -, - 118 -, - 128 -, - 156 -
field of view · - 21 -, - 23 -, - 26 -, - 52 -, - 53 -, - 75 -, - 98 -, - 101 -, - 104 -, - 105 -, - 108 -, - 118 -, - 124 -, - 125 -, - 126 -, - 128 -, - 142 -, - 143 -, - 144 -, - 145 -, - 146 -, - 150 -, - 157 -, - 158 -
flow cell · - 52 -, - 57 -, - 58 -, - 59 -, - 118 -, - 119 -, - 124 -, - 125 -, - 128 -, - 157 -
flow rate · - 131 -, - 132 -, - 134 -, - 135 -, - 136 -, - 137 -
flow rig · IV, XVIII, - 130 -, - 132 -, - 133 -, - 135 -, - 137 -, - 145 -, - 146 -, - 152 -, - 155 -, - 157 -, - 158 -
fluid · IV, XVI, XVII, XVIII, - 4 -, - 23 -, - 24 -, - 25 -, - 26 -, - 52 -, - 53 -, - 54 -, - 55 -, - 57 -, - 59 -, - 68 -, - 71 -, - 86 -, - 94 -, - 106 -, - 112 -, - 114 -, - 118 -, - 122 -, - 128 -, - 130 -, - 131 -, - 132 -, - 133 -, - 134 -, - 135 -, - 136 -, - 137 -, - 138 -, - 140 -, - 141 -, - 142 -, - 143 -, - 144 -, - 146 -, -

147 -, - 148 -, - 150 -, - 151 -, - 152 -, - 155 -, - 156 -, - 157 -, - 158 -
fluid density · - 24 -, - 135 -, - 136 -, - 148 -
fluorescein · - 23 -, - 37 -
fluorescence · IV, VIII, XVII, - 23 -, - 24 -, - 26 -, - 37 -, - 38 -, - 47 -, - 52 -, - 53 -, - 54 -, - 55 -, - 58 -, - 59 -, - 60 -, - 61 -, - 62 -, - 63 -, - 64 -, - 65 -, - 66 -, - 67 -, - 68 -, - 113 -, - 115 -, - 125 -, - 128 -, - 140 -, - 152 -, - 155 -, - 157 -
fluorescent · IV, XVIII, - 37 -, - 38 -, - 53 -, - 54 -, - 55 -, - 56 -, - 57 -, - 58 -, - 59 -, - 61 -, - 63 -, - 65 -, - 66 -, - 68 -, - 71 -, - 78 -, - 94 -, - 112 -, - 113 -, - 114 -, - 115 -, - 152 -, - 155 -, - 156 -, - 157 -
fluorophore · - 37 -, - 53 -, - 54 -, - 58 -, - 61 -, - 62 -, - 63 -, - 64 -, - 65 -, - 66 -
fringe depth · - 72 -, - 75 -, - 76 -, - 115 -, - 116 -
fringe separation · - 72 -, - 75 -, - 76 -, - 98 -, - 115 -, - 117 -, - 142 -
fringes · IV, - 23 -, - 26 -, - 32 -, - 33 -, - 34 -, - 35 -, - 47 -, - 53 -, - 71 -, - 72 -, - 73 -, - 77 -, - 78 -, - 79 -, - 80 -, - 81 -, - 83 -, - 84 -, - 86 -, - 87 -, - 88 -, - 89 -, - 94 -, - 98 -, - 100 -, - 102 -, - 103 -, - 104 -, - 115 -, - 116 -, - 117 -, - 123 -, - 125 -, - 133 -, - 139 -, - 156 -
full field imaging · IV, - 52 -, - 68 -

G

gap (phase gaps) · - 118 -
grating · - 31 -, - 32 -, - 33 -, - 34 -, - 35 -, - 36 -, - 44 -, - 45 -, - 46 -, - 47 -, - 68 -, - 71 -, - 72 -, - 74 -, - 75 -, - 76 -, - 77 -, - 78 -, - 79 -, - 83 -, - 84 -, - 85 -, - 86 -, - 94 -, - 156 -
grating equation · - 74 -
gravity · IV, - 23 -, - 131 -, - 135 -, - 142 -, - 148 -, - 152 -, - 157 -

H

hardware · - 71 -, - 98 -
hydrophobicity · - 2 -

I

inner filter effect · *See* self-quenching
interference · IV, - 23 -, - 32 -, - 34 -, - 35 -, - 36 -, - 53 -, - 68 -, - 71 -, - 72 -, - 73 -, - 74 -, - 77 -, - 79 -, - 80 -, - 81 -, - 83 -, - 86 -, - 87 -, - 89 -, - 90 -, - 94 -, - 156 -
interference (two beam interference equation) · - 73 -, - 160 -
interferogram · - 21 -, - 22 -, - 44 -, - 45 -, - 46 -, - 83 -, - 89 -, - 92 -, - 118 -, - 119 -, - 120 -
interpolation · - 100 -, - 105 -, - 147 -
IR · - 43 -
irradiance · - 73 -, - 82 -, - 160 -

J

jump (phase jumps) · - 120 -

K

Kiton Red 620 · - 59 -

L

LabView · XVIII, - 82 -, - 89 -, - 90 -, - 91 -, - 93 -, - 104 -, - 133 -, - 156 -
laminar flow · - 24 -, - 135 -, - 137 -, - 152 -, - 157 -
Laser Scanning · - 30 -
laser source · - 31 -, - 53 -, - 58 -, - 155 -
Laser Speckle Pattern Sectioning · - 32 -, - 47 -
lateral resolution · - 142 -
LCD · - 9 -, - 34 -
LIF · - 37 -, - 38 -
lithography · XVI, - 2 -, - 11 -, - 15 -, - 16 -, - 19 -, - 158 -, - 159 -
long pass filter · - 58 -, - 63 -, - 64 -
lotus effect · - 2 -

M

Marangoni · - 19 -
Matlab · - 83 -, - 91 -, - 92 -, - 104 -, - 105 -, - 106 -, - 107 -, - 120 -, - 126 -, - 143 -, - 145 -, - 148 -, - 150 -, - 151 -, - 163 -
MEMS · VIII, - 8 -
metrology · IV, XVII, - 52 -, - 155 -
Michelson interferometer · - 21 -, - 79 -, - 80 -, - 86 -
microscope objective · - 58 -, - 76 -, - 77 -, - 78 -, - 79 -, - 83 -, - 84 -, - 85 -, - 88 -, - 94 -
Moiré · - 31 -, - 32 -, - 33 -
molar absorptivity · - 54 -, - 55 -, - 56 -, - 57 -, - 59 -
Molarity · - 142 -
MOSFET · - 104 -

N

noise · - 71 -, - 83 -, - 84 -, - 85 -, - 87 -, - 100 -, - 107 -, - 122 -, - 147 -, - 163 -
numerical aperture · - 26 -, - 52 -, - 53 -, - 76 -, - 77 -, - 78 -
numerical aperture object · VIII, - 101 -

O

order fringe · - 102 -
order polynomial fit · - 83 -, - 101 -, - 104 -, - 108 -, - 121 -, - 144 -, - 145 -, - 147 -, - 150 -, - 151 -

P

pellicle beam splitter · - 102 -, - 141 -
phase · IV, VIII, XVIII, - 21 -, - 22 -, - 23 -, - 25 -, - 27 -, - 32 -, - 34 -, - 35 -, - 36 -, - 40 -, - 41 -, - 42 -, - 43 -, - 44 -, - 45 -, - 46 -, - 47 -, - 53 -, - 72 -, - 73 -, - 74 -, - 76 -, - 79 -, - 81 -, - 82 -, - 83 -, - 84 -, - 85 -, - 86 -, - 87 -, - 88 -, - 89 -, - 90 -, - 91 -, - 92 -, - 93 -, - 94 -, - 98 -, - 99 -, - 100 -, - 102 -, - 103 -, - 109 -, - 112 -, - 113 -, - 116 -, - 118 -, - 119 -, - 120 -, - 122 -, - 124 -, - 126 -, - 127 -, - 128 -, - 131 -, - 133 -, - 143 -, - 147 -, - 152 -, - 156 -, - 157 -, - 163 -
phase map · IV, XVIII, - 83 -, - 86 -, - 121 -, - 122 -
phase noise · - 83 -, - 84 -, - 116 -, - 121 -, - 122 -
phase resolution · - 53 -, - 85 -, - 86 -, - 94 -, - 118 -, - 156 -
phase shift · - 22 -, - 32 -, - 43 -, - 45 -, - 103 -, - 120 -
phase-height relationship · IV, - 100 -, - 104 -, - 109 -, - 112 -, - 128 -, - 143 -, - 152 -
phase-stepping · IV, - 89 -, - 90 -, - 94 -, - 118 -, - 125 -, - 157 -
photobleaching · - 66 -
photogrammetry · - 30 -, - 33 -
piezoelectric · VIII, - 22 -, - 82 -, - 88 -, - 89 -, - 93 -, - 133 -
planarization · - 19 -, - 20 -
Poiseuille flow · - 135 -
polarization · - 39 -, - 40 -, - 41 -, - 42 -, - 43 -, - 44 -, - 45 -, - 88 -
polyfit · - 105 -, - 147 -, - 150 -, - 151 -, - 163 -
polyval · - 105 -, - 147 -, - 150 -, - 151 -, - 163 -
pressure gradient · - 135 -
profilometry · - 98 -, - 99 -, - 118 -
projection angle · - 72 -, - 75 -, - 76 -, - 115 -

Q

quartz · - 57 -
quenching · - 65 -

R

refractive index · - 38 -, - 39 -, - 40 -, - 41 -, - 43 -, - 57 -, - 81 -, - 160 -
reservoir · - 131 -, - 132 -, - 135 -, - 136 -, - 140 -, - 147 -, - 158 -
resolution · IV, XVII, - 11 -, - 12 -, - 15 -, - 25 -, - 26 -, - 30 -, - 31 -, - 32 -, - 33 -, - 34 -, - 36 -, - 38 -, - 45 -, - 47 -, - 52 -, - 53 -, - 58 -, - 76 -, - 83 -, - 94 -, - 105 -, - 113 -, - 124 -, - 128 -, - 157 -, - 158 -
Reynolds · IX, - 24 -, - 25 -, - 148 -, - 149 -
Rhodamine B · - 53 -, - 55 -, - 56 -, - 59 -, - 60 -, - 62 -, - 63 -, - 65 -, - 66 -, - 67 -, - 68 -, - 104 -, - 109 -, - 118 -, - 119 -, - 122 -, - 124 -, - 128 -, - 138 -, - 142 -, - 152 -, - 156 -, - 157 -
rig · - 122 -, - 123 -, - 157 -
Runge's phenomenon · - 147 -

S

saturation · - 57 -, - 58 -, - 60 -, - 61 -, - 62 -, - 64 -, - 65 -, - 66 -, - 67 -, - 84 -, - 104 -
self-quenching · - 66 -
silicon (silica) · - 6 -, - 7 -, - 8 -
Snell's law · - 38 -, - 39 -
software · - 71 -, - 87 -, - 98 -, - 118 -
solar cell · XVI, - 5 -, - 6 -, - 130 -
solubility · - 61 -, - 119 -
spectrometer · - 63 -, - 64 -
spin coating · XVII, - 9 -, - 10 -, - 15 -, - 16 -
Stokes shift · - 37 -
Structured light · - 33 -, - 34 -, - 47 -, - 68 -, - 71 -, - 94 -
Sulforhodamine 640 · - 53 -, - 56 -, - 59 -, - 60 -, - 61 -, - 62 -, - 63 -, - 65 -, - 66 -, - 67 -, - 113 -

T

thickness · IV, XVII, - 2 -, - 4 -, - 6 -, - 8 -, - 9 -, - 10 -, - 11 -, - 15 -, - 16 -, - 17 -, - 21 -, - 24 -, - 25 -, - 26 -, - 38 -, - 41 -, - 43 -, - 52 -, - 61 -, - 68 -, - 74 -, - 112 -, - 114 -, - 117 -, - 118 -, - 125 -, - 126 -, - 127 -, - 130 -, - 134 -,- 135 -, - 136 -, - 137 -, - 140 -, - 141 -, - 142 -, - 143 -, - 147 -, - 148 -, - 150 -, - 157 -, - 158 -
thin film · XVI, XVII, - 2 -, - 3 -, - 5 -, - 6 -, - 7 -, - 8 -, - 9 -, - 11 -, - 15 -, - 16 -, - 17 -, - 18 -, - 21 -, - 24 -, - 25 -, - 38 -, - 39 -, - 41 -, - 43 -, - 47 -, - 52 -, - 53 -, - 54 -, - 128 -, - 130 -, - 134 -, - 152 -, - 157 -, - 158 -
Time of Flight · - 30 -, - 47 -
topographic features · XVII, - 3 -, - 16 -, - 19 -, - 20 -, - 21 -, - 27 -, - 130 -
topography · XVI, XVII, XVIII, - 2 -, - 11 -, - 12 -, - 15 -, - 16 -, - 19 -, - 20 -, - 21 -, - 23 -, - 25 -, - 26 -, - 27 -, - 52 -, - 53 -, - 68 -, - 118 -, - 128 -, - 130 -, - 131 -, - 132 -, - 134 -, - 135 -, - 137 -, - 139 -, - 142 -, - 143 -, - 144 -, - 145 -,- 147 -, - 148 -, - 150 -, - 152 -, - 155 -, - 156 -, - 157 -, - 158 -, - 159 -
twin fibre system · IV, XVII, - 68 -, - 71 -, - 72 -, - 80 -, - 83 -, - 84 -, - 85 -, - 86 -, - 88 -, - 94 -, - 113 -, - 118 -, - 128 -, - 156 -
Twyman-Green interferometer · - 21 -, - 44 -, - 45 -, - 99 -

U

unwrapped phase map · - 83 -, - 84 -, - 85 -, - 98 -, - 103 -, - 104 -, - 105 -, - 107 -, - 116 -, - 118 -, - 121 -, - 122 -, - 125 -, - 126 -, - 133 -, - 139 -, - 141 -, - 143 -, - 157 -
unwrapping algorithm · - 103 -, - 120 -
USAF 1951 Chart · - 58 -, - 142 -
UV · - 18 -, - 24 -, - 43 -, - 137 -

V

visibility · - 22 -, - 88 -, - 117 -
VLSI · - 18 -, - 19 -
voltage · - 4 -, - 5 -, - 88 -, - 89 -, - 90 -, - 93 -, - 133 -

W

wavefront · - 21 -, - 22 -, - 89 -, - 99 -
wettability · - 137 -, - 138 -, - 152 -
Wheatstone bridge · - 5 -
wrapped phase · - 83 -, - 84 -, - 118 -, - 120 -, - 126 -, - 163 -

Y

Young's double-slit experiment · - 86 -, - 87 -

Z

zero · *See* absolute zero
zero order · - 77 -